PHILOSOPHICAL TRANSACTIONS OF THE ROYAL SOCIETY A MATHEMATICAL, PHYSICAL & ENGINEERING SCIENCES

The Breakdown of Superfluidity in Liquid ^{4}He: III. Nucleation of Quantized Vortex Rings

R. M. Bowley, P. V. E. Mcclintock, F. E. Moss, G. G. Nancolas and P. C. E. Stamp

Phil. Trans. R. Soc. Lond. A 1982 **307**, 201-260
doi: 10.1098/rsta.1982.0109

Phil. Trans. R. Soc. Lond. A **307**, 201–260 (1982) [201]
Printed in Great Britain

THE BREAKDOWN OF SUPERFLUIDITY IN LIQUID ^{4}He: III*. NUCLEATION OF QUANTIZED VORTEX RINGS

By R. M. BOWLEY†, P. V. E. McCLINTOCK‡, F. E. MOSS‡§, G. G. NANCOLAS‡ and P. C. E. STAMP‡||
† *Department of Physics, University of Nottingham, Nottingham NG7 2RD, U.K.*
‡ *Department of Physics, University of Lancaster, Lancaster LA1 4YB, U.K.*

(*Communicated by W. F. Vinen, F.R.S. – Received 4 December* 1981)

CONTENTS

* Parts I and II appeared respectively in *Phil. Trans. R. Soc. Lond.* A **284**, 179–224 (1977) and *Phil. Trans. R. Soc. Lond.* A **296**, 581–595 (1980).

§ Permanent address: Department of Physics, University of Missouri-St Louis, Natural Bridge Road, St Louis, Missouri 63121, U.S.A.
|| Now at: Physics Division, School of Mathematical and Physical Sciences, University of Sussex, Falmer, Brighton BN1 9QH, U.K.

We have measured the rate ν at which negative ions nucleate charged vortex rings in isotopically pure superfluid ^{4}He for pressures, P, temperatures, T, and electric fields, E, within the ranges: $15 < P < 25$ bar†; $0.3 < T < 0.9$ K; $5 \times 10^4 < E < 10^6$ V m^{-1}. The measurements were done by a novel electrostatic induction technique specially developed for the purpose, and this is described in some detail. It was found that: at fixed E and P, ν increases rapidly with T for $T >$ *ca.* 0.5 K, but approaches a temperature-independent limiting value ν_s for $T < 0.5$ K; at fixed P and T, ν at first increases rapidly with E but then passes through a maximum at *ca.* 7×10^5 V m^{-1} and decreases again for larger values of E; at fixed E and T, ν increases rapidly with decreasing P until, below *ca.* 15 bar, the signal becomes too small to use. In all cases, ν was found to be considerably smaller than had been measured for low E by earlier workers using helium of the natural isotopic ratio (*ca.* 2×10^{-7}). The same signals were also used for measuring ionic drift velocities, $\bar{v}$, for $\nu <$ *ca.* 3×10^4 s^{-1}. Values of the matrix element for roton pair emission have been deduced from the $\bar{v}(E)$ measurements for several pressures in the range $17 < P < 25$ bar. The pressure dependence of the Landau critical velocity was measured and is compared with predictions based on accepted values of the roton parameters. Analysis of the nucleation data showed that, at fixed $\bar{v}$ and P, $(\nu - \nu_s) \propto n_r$, where n_r is the thermal roton density, suggesting that ν is the sum of contributions from two independent nucleation mechanisms: a spontaneous mechanism responsible for ν_s and a roton driven mechanism responsible for the increase in ν with T above 0.5 K. The existence of a maximum in $\nu(E)$ appears to be inconsistent with the peeling model of vortex nucleation; but it is entirely to be expected on the basis of the quantum transition model. It is shown that all the nucleation rate measurements reported herein are consistent with the quantum transition model, provided that due account is taken of the possibility that roton absorption may give rise to a critical velocity v_r that is smaller than the critical velocity v_v characteristic of the spontaneous nucleation mechanism. Values of v_v and v_r are deduced from the experimental data for several pressures. The fact that exponential decay of the bare ion signal still occurs even when $v \gtrsim v_v$ (or v_r) constitutes the first experimental evidence that the microscopic mechanisms responsible for vortex nucleation are probabilistic in nature.

1. INTRODUCTION

The superfluidity of liquid ^{4}He can break down in two quite different ways. An object moving through the liquid at sufficient speed can dissipate kinetic energy either through the creation of rotons or, alternatively, through the production of quantized vorticity. The former process, the one originally predicted by Landau (1941, 1947), turned out to be relatively rare in reality but it has, none the less, been investigated in considerable detail by studying the motion of negative ions in pressurized He II (Allum *et al.* 1977, hereinafter referred to as I; Ellis *et al.* 1980*a*, hereinafter referred to as II). It is to the latter and far commoner process that the present paper is addressed.

The mechanisms through which quantized vorticity is formed in the liquid are still not

† 1 bar = 10^5 Pa.

properly understood. Indeed, they can be regarded as one of the major unsolved problems of superfluid physics, at least as far as ^{4}He is concerned. The phenomenon can be studied through a number of different types of experiment, of which the creation of quantized vortex rings by ions, the subject of this paper, provides one particularly simple and well characterized example. The relevant properties of the negative ion, which may be regarded as a semi-macroscopic spherical cavity in the liquid, were summarized in I. Thus the nascent vortex ring first appears in the vicinity of a moving spherical cavity whose radius and hydrodynamic effective mass are accurately known, in a liquid that can readily be prepared in a state of quite extraordinary purity, and far distant from the interfering influence of the chamber walls whose surface microstructure is usually complex and, in practice, often in doubt.

In §1*a* we discuss the use of ions as probes for investigating the breakdown of superfluidity in liquid ^{4}He, in §1*b* we present a brief review of earlier experimental work on the ion–vortex ring transition and in §1*c* we describe briefly the theoretical models that have been proposed to describe the transition. In §1*d* we place the present research programme in context.

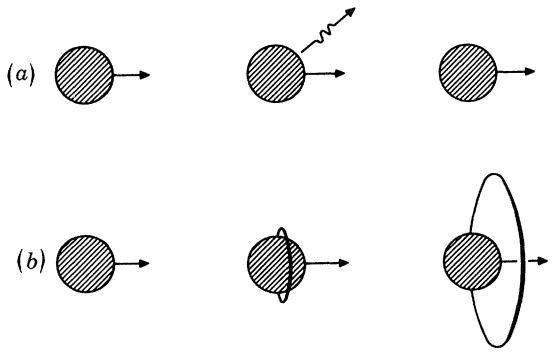

FIGURE 1. Two alternative mechanisms through which a moving ion can dissipate energy in superfluid ^{4}He at zero temperature: (*a*) the ion may create a roton (or a pair of rotons); (*b*) the ion may create a quantized vortex ring. In each case, the time sequence runs from left to right and the direction of motion is indicated by the arrows. It should be noted that in (*a*) the final state of the charge carrier is still a bare ion whereas in (*b*) the carrier ends up as a charged vortex ring whose properties are very different from those of a bare ion.

(*a*) *Ions and the breakdown of superfluidity*

The two known mechanisms through which ions can dissipate energy in superfluid ^{4}He (assumed, for the moment, to be at zero temperature) are illustrated diagrammatically in figure 1.

(i) Rotons may be emitted (figure 1*a*) from the moving ion, apparently in pairs, as described in detail in I. This process is also of relevance to the present experiments because, as described in §2, our technique for investigating the vortex nucleation process (ii) relies on roton creation to provide the principal means of controlling the drift velocity $\bar{v}$ of the ion.

(ii) A vortex ring may be created (figure 1*b*) by the moving ion. Hydrodynamic forces will usually bind the ion and ring tightly together and, in the presence of an electric field, the charged ring will steadily grow, decelerating as it travels down the field gradient.

In general, the two processes appear to compete with each other. Because (ii) usually leads to the loss of the bare ion, whereas (i) does not, (ii) inevitably appears to dominate the scene in most experimental situations.

At finite temperatures account must be taken of the thermal excitations which, for the relevant range below 1 K, can be considered as a dilute gas of rotons and phonons. Their most obvious influence lies in providing a source of drag by scattering from the moving ion. Thus, for roton creation in a given electric field E, the drift velocity $\bar{v}$ of a bare ion may be expected to decrease with increasing temperature T: whether or not this effect is significant will, of course, depend on the relative values of E and T (see I). Under conditions such that roton creation does not occur, the ion will approach a value of $\bar{v}$ determined by a balance between the force due to the electric field and the drag due to excitation scattering, unless or until it creates and is trapped by a vortex ring. In the latter case, the ring may or may not be stable, again depending on the relative magnitudes of T and E and also on whether isotopic impurities are present.

Fetter (1976) has presented an excellent and virtually inclusive (up to 1972) review of experimental and theoretical work on ions and vortices in liquid helium, to which the reader is referred for further information about the general background to the present research programme on the breakdown of superfluidity.

(*b*) *Earlier work on the ion–vortex ring transition*

The nature of the bare ion–charged vortex ring transition still remains obscure more than two decades after Meyer & Reif (1961) first reported their discovery of charge carriers that displayed 'runaway behaviour' in He II. They found that these carriers could not necessarily be stopped by a retarding electric field, but only by a retarding potential of magnitude greater than or equal to that across the region in which they had been created. Although the beautiful experiments of Rayfield & Reif (1964) soon enabled the carriers to be identified unambiguously as charged vortex rings, little information could be gleaned about the creation mechanism. Meyer & Reif had noted earlier, however, that ring creation could be inhibited by the application of pressure to the helium: above 15 bar†, bare ions arrived at the collecting electrode; it was at lower pressures than this that the 'runaway behaviour' had been observed.

These early results were confirmed through subsequent, more detailed, experiments by Careri *et al.* (1965), Rayfield (1966, 1967, 1968*a*), Neeper (1968), and Neeper & Meyer (1969). One of the principal conclusions to emerge was that, as the electric field E was increased, $\bar{v}$ rose towards a maximum value v_c at $E = E_c$. For fields beyond E_c, $\bar{v}$ decreased very rapidly again and it was evident that the charge carriers were exclusively vortex rings: in some sense, therefore, $\bar{v}_c$ could be regarded as a critical drift velocity for the formation of a vortex ring. Typically, $\bar{v}_c$ lay in the range 30–50 m s^{-1} for either positive or negative ions, for all pressures up to that for solidification, and was insensitive to temperature. The exception was, of course, that of negative ions for pressures above 15 bar where $\bar{v}$ was believed at the time (but cf. results and discussion in I) to approach a 'plateau velocity' equal to the Landau critical velocity for roton creation. Neeper & Meyer observed, however, that some vortex rings were also being created in the plateau region. Furthermore, as the cell was cooled below 0.5 K, the proportion of charged rings to bare ions increased until, at 0.3 K, no bare ions at all could be detected at the collector. This latter observation, which caused considerable surprise at the time, may now be accounted for in terms of ^{3}He isotopic impurities which are invariably present, albeit at a very low concentration, in commercial ^{4}He (see §3*b* below).

A series of experiments in which ionic velocities were carefully correlated with their corresponding signal magnitudes, each as a function of electric field, enabled Strayer *et al.* (1971)

† 1 bar = 10^5 Pa.

to infer that the creation of rings was probably a stochastic process. This was subsequently confirmed (but see §1*c* below) by Titus & Rosenshein (1973), and by Zoll & Schwarz (1973), who succeeded in measuring directly the average time dependence of the transition process. They were able to show that the creation of charged vortex rings could be characterized by a nucleation rate ν such that, in analogy with radioactive decay, the number N of bare ions remaining in a travelling bunch of ions after time t could be written

$$N = N_0 e^{-\nu t}, \tag{1}$$

where N_0 is the number of ions in the bunch at time zero. For technical reasons, both sets of experiments were confined to electric fields of no more than a few kilovolts per metre.

The behaviour of ν in larger electric fields is, however, of particular theoretical interest (see §1*c*, below). Some indirect information about this régime for the case of negative ions in pressurized He II was obtained by investigating the characteristics of a superfluid field-emission diode (Phillips & McClintock 1974; 1975) and by analysing the variation of signal magnitude with electric field for cells of two different lengths (Allum & McClintock 1978*a*, *b*). For temperatures near 1 K it was possible to deduce values of ν from the shape of vortex ring signals arriving at the collector (Allum & McClintock 1978*b*). These experiments yielded a number of surprises. In particular, it seemed that: (i) under certain circumstances ν decreased with increasing electric field, whereas models of the transition process (see §1*c*) suggested the opposite; (ii) sometimes ν seemed to increase with increasing temperature and at other times it appeared to decrease, behaviour that, again, was apparently inexplicable in terms of the existing models. There was, however, a suspicion (Allum & McClintock 1976) that the behaviour of ν might have been influenced by ^{3}He impurities in the ordinary (unpurified) liquid ^{4}He samples that were used.

The effect of added ^{3}He impurities on the ion–vortex ring transition has been investigated for weak electric fields by a number of workers, including Rayfield (1968*b*), Neeper & Meyer (1969), Zoll & Schwarz (1973) and Zoll (1976). It was found that, other things being equal, the addition of ^{3}He to natural helium caused a marked enhancement of ring production as shown either through a reduction in $\bar{v}_c$ or through an increase in ν. The possibility that ^{3}He might be able to influence ring creation when present at the natural level (*ca.* 2×10^{-7}) does not seem to have been considered. It will be shown below (in §3*b*), however, that naturally occurring isotopic impurities are in fact of considerable importance in nucleation by negative ions. This should be borne in mind in relation to all experimental measurements purportedly on pure ^{4}He but where, in reality, unpurified commercial ^{4}He has been used, as usually seems to have been the case before the present work.

(*c*) *Models of the ion–vortex ring transition*

Two mutually antithetic types of model have been proposed to describe the ion–vortex ring transition.

One suggestion is that, as sketched in (*a*) of figure 2, the vortex ring grows continuously from the surface of the moving ion, starting with a loop of vortex core of microscopic proportions. This so-called peeling model was introduced by Rayfield (1967) to account for his observation that, in a relatively strong ^{3}He–^{4}He solution, the drift velocity can change smoothly through the transition region without any sign of the sudden discontinuity expected on formation of a fully fledged vortex ring. The model was subsequently modified and refined by Donnelly &

Roberts (1971). Influenced by the ideas of Iordanskii (1965) and Langer & Fisher (1967), they proposed that the initial loop of vortex core grew from a 'proto-ring' as the result of a thermal fluctuation. They suggested that this proto-ring was in fact a roton, localized near the equator of the moving ion. Once a fluctuation had occurred that was large enough to enable an energy barrier to be surmounted, the nascent vortex ring would peel away continuously from the ion very much in the manner envisaged by Rayfield. The fluctuation rate, and hence ν, was calculated to be a very rapid function of the ionic velocity. It should, however, be noted that the smooth variation of $\bar{v}$ near $\bar{v}_c$, which provided the original motivation for introducing the peeling model, has received an alternative, entirely satisfactory and plausible explanation from Padmore (1972) and Zoll & Schwarz (1973). These authors have pointed to the existence of a régime wherein the conditions necessary for ring creation are satisfied but those required for the stability of the resultant ring are not. Under such circumstances, the

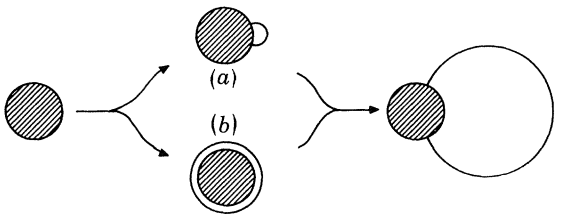

FIGURE 2. Two alternative models of the vortex creation process: (*a*) in the peeling model, the ring grows out from a small loop of vortex core attached at both ends to the ion; (*b*) the ring appears spontaneously as the result of a quantum transition, one possibility being that it does so in a symmetrical position girdling the equator of the ion before the ion moves sideways and becomes trapped on the vortex core. The velocity of the ion in each case is assumed to be directed at right angles to the page and the time sequence runs from left to right as indicated by the arrows.

carrier must cycle back and forth between the bare ion and charged ring states and the measured drift velocity will depend mainly on the relative times spent in each condition, thus leading to a continuous variation of $\bar{v}$ through the transition region, as observed. It should also be noted that Schwarz & Jang (1973) have cast considerable doubt on the concept of 'localized roton states' introduced by Donnelly & Roberts. Assuming that these do not exist in reality, one may conclude that, if the proto-rings are still to be identified as rotons, the vortex nucleation rate would be closely related to the thermal roton density and hence should be highly sensitive to changes of temperature.

The other school of thought, by contrast, simply holds that the transition will occur as soon as (or very quickly after) it is allowed to do so while satisfying the conservation laws for energy and momentum, unless there is some hidden symmetry that forbids the process. Thus, there will be a critical velocity v_v below which the transition cannot occur, in close analogy with the Landau critical velocity v_L below which roton emission cannot occur (see I). This general approach was put forward tentatively by Rayfield & Reif (1964). A subsequent estimate by Pines (1966), however, suggested that v_v would be close to 70 m s^{-1}, a value considerably and discouragingly in excess of the $\bar{v}_c$ values of typically 30–40 m s^{-1} then being measured. Little further interest seems to have been shown in this 'quantum transition model' until it was taken up and developed in explicit detail by Schwarz & Jang (1973); see also Blount & Varma (1976). These authors proposed that the critical velocity v_v would correspond to the spontaneous appearance of a vortex ring girdling the equator of the ion, which would subsequently move sideways and become trapped on the core. This process is sketched in (*b*) of figure 2.

They were able to calculate approximate values of v_v for both positive and negative ions over the full range of pressures 0–25 bar, and to show that these were plausible in relation to measurement of $\bar{v}$ and ν in weak electric fields. The principal difficulty in making a quantitative comparison with experiment lay in the fact that the distribution function of ionic velocities $f(v)$ was unknown and, except in one special set of circumstances, could not readily be calculated. It was evident, however, that significant numbers of ions in the high velocity tail of $f(v)$ could quite well be attaining v_v and creating rings, even though the centre of gravity of $f(v)$, corresponding to $\bar{v}$, remained at a lower velocity. The only situation, so far, where it has proved possible to calculate $f(v, E)$ explicitly (Bowley & Sheard 1977) is where $\bar{v}$ is limited by roton emission (see I) i.e. the case of negative ions for large E/T and $P > 15$ bar. Bowley (1976) suggested that the vortex ring nucleation rate R as a function of the instantaneous ionic velocity v could, as a simplest plausible assumption, be written as

$$R = R_0\theta(v - v_v), \tag{2}$$

where R_0 is a constant and θ is the unit step function. (We reserve ν to represent the average nucleation rate, which is what is measured in an actual experiment.) In other words, he proposed that there would be no nucleation for $v < v_v$ and nucleation at the constant rate R_0 for $v > v_v$. On the basis of this assumption, he showed how values of v_v and R_0 could be extracted from measurements of $\nu(E)$ by using the distribution function $f(v, E)$ deduced from measurements of $\bar{v}(E)$.

TABLE 1. DISTINCTIVE FEATURES OF TWO MODELS OF THE VORTEX NUCLEATION PROCESS

Peeling model	*Quantum transition model*
No true critical velocity.	A well defined critical velocity.
Ring grows out from surface of ion; so ion is always bound on vortex core.	Ring appears spontaneously, close to ion, which then moves sideways and gets trapped on vortex core.
Nucleation rate closely related to the thermal roton density; hence a rapid temperature dependence.	Virtually no temperature dependence (in form originally proposed).

The main differences between the two models are summarized in table 1. It should be noted that, although the peeling model in the form developed by Donnelly & Roberts (1971) takes no explicit account of the existence of the distribution function $f(v, E)$, there is no reason in principle why it should not be extended to do so. The only temperature dependence expected *a priori* for the quantum transition model is that arising from the slight broadening of the distribution function due to excitation scattering. Such an effect would, of course, also occur for the peeling model but it would be totally swamped by the temperature dependence of the roton (proto-ring) density. It must be emphasized that use of the term 'quantum transition model' is intended to convey simply that the initial vortex ring appears spontaneously, in more or less fully fledged form; it should not, of course, be taken as carrying any implication that quantum mechanics plays no role in the peeling model.

The relative merits of these two models are discussed below (see §4*c*) in relation to their ability to account for the experimental results. We can at this stage comment on very general grounds, however, that the quantum transition model appears *a priori* to be somewhat the less plausible of the two because it must imply a comparatively large discontinuous change in the wavefunction of the system at the moment of nucleation. The retention of cylindrical symmetry

during nucleation as proposed by Schwarz & Jang is, none the less, a feature presenting an undeniable aesthetic appeal.

An interesting point raised by Zoll & Schwarz (1973) relates to the probabilistic nature, or otherwise, of the transition. The fact that the number of bare ions in a travelling cloud decays according to (1) has been taken (Titus & Rosenshein 1973) as a vindication of the Donnelly & Roberts (1971) version of the peeling model. Zoll & Schwarz point out, however, that this is not necessarily a valid conclusion: if $\bar{v}$ is significantly less than v_v, so that only the tail of the velocity distribution function extends beyond v_v, then, almost regardless of the physical nature of the transition itself, the macroscopic behaviour observed in an experiment will display probabilistic features. The only way to obtain direct information about the actual transition, therefore, is to arrange for measurements under conditions such that $\bar{v} \gtrsim v_v$ which, in practice, means measurements of v in very strong electric fields. Such measurements have formed a part of the present research programme and they are presented and discussed below.

(*d*) *The present research programme*

The variation of signal magnitude with electric field and temperature in I displayed a number of features (see §1*b* above and also §3*b* of I) that did not at first sight appear to be readily explicable in terms of either of the models described above. The principal aim of the present research programme, therefore, was to obtain accurate measurements of v in pure liquid ^{4}He over a wide range of P, E and T within the roton emission dominated régime, to try and clarify the situation. It was hoped, in particular, to establish the applicability or otherwise of each of the models.

In view of the strong suspicion that some, at least, of the seemingly anomalous behaviour in I had been associated with isotopic impurities, it was clearly essential that the measurements should be made with isotopically pure ^{4}He. Accordingly, a technique was developed for the isotopic purification of ^{4}He (Atkins & McClintock 1976), by using superfluid heat flush, and this was then used as the basis of a larger-scale isotopic separation cryostat (Scott & McClintock 1977; McClintock 1978) which was capable on warming of pressurizing a standard gas bottle to 35 bar with pure ^{4}He. Helium prepared in this apparatus is believed to be entirely devoid of ^{3}He. More recently, we have commissioned and enjoyed the greater convenience provided by a continuous flow isotopic purification system (Ngan *et al.* 1981), based on the same principle of operation, from which a succession of standard gas bottles may be filled to 120 bar with pure ^{4}He.

A new method was devised for measuring v. Based on electrostatic induction, and described in detail in §2*a* below, this novel technique has enabled the measurements to be extended to electric fields some two orders of magnitude greater than previously (Titus & Rosenshein 1973; Zoll & Schwarz 1973; Zoll 1976). Development and testing of the induction cell were done with natural helium (Stamp *et al.* 1979). Some brief reports and preliminary discussion of the initial results obtained with isotopically pure ^{4}He have also been published (Bowley *et al.* 1980; McClintock *et al.* 1980*a*, *b*).

2. Experimental details

The cryogenics and thermometry were essentially as described in I and II. Cleaning, condensation and pressurization of the helium sample were also as before, except in that isotopically pure ^{4}He replaced the ordinary well helium used previously. In §2*a*, an analysis of the

electrostatic induction technique for measuring ν is presented for three model electrode geometries approximating to some of the structures used in our experiments. The analysis is developed in some detail because the technique is a new one and, in particular, because our interpretation of the data presented in §3 depends on confidence in its reliability. The experimental cell used for most of the measurements is described in §2*b* and a brief description of the control circuitry and electronics is given in §2*c*. Signal analysis and data handling are discussed respectively in §2*d* and §2*e*.

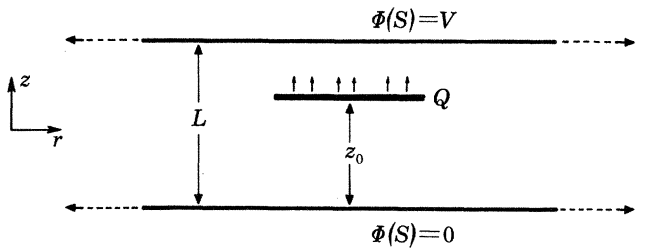

FIGURE 3. Idealized cell geometry for measuring the rate ν of vortex nucleation by means of the electrostatic induction technique. An infinitesimally thin disc-shaped ensemble of bare ions, total charge Q, is driven from the lower plate towards the upper one by means of the uniform electric field. If there is no vortex nucleation between the plates, a constant current will have to flow from the upper plate in order that its potential should remain equal to V. If nucleation is occurring at rate ν, however, the current will be proportional to $e^{-\nu t}$, where t is the time.

(*a*) *The electrostatic induction technique for measuring* ν

The crucial problem in the design of these experiments was to devise a method of determining ν accurately under a variety of different conditions (depending on the temperature, pressure and applied electric field) involving very different values of ν. The novel feature of the new cell design that accomplishes this task is a 'current induction technique': the nucleation rate is determined by measuring the rate at which a bare ion current of negative ions decays. This is possible because an ion, once it has produced a vortex ring and been captured by it, will slow down to a negligible velocity in a very short time. This means that, except in extremely weak electric fields, the resulting ion–ring complex effectively makes no contribution to the measured current from the moment that it is formed.

The perfect cell for such a method would consist simply of two infinite parallel conducting plates, separated by a distance L and with a uniform field $E = -V/L$ between them (figure 3). A disc-shaped ensemble of bare ions would be driven by the field at a constant velocity between the plates, decaying in density as it went. The theorem (see, for example, Pippard 1972)

If capacitor plates of arbitrary shape are maintained at zero and unit potentials, and a charge Q is taken from zero potential and placed at a point where the potential is ϕ, a charge ϕQ is induced on the plate at unit potential

demonstrates that an infinitesimally thin disc of charge $Q(t)$ situated a distance z_0 from the bottom plate will induce a charge $q(z_0) = -Qz_0/L$ on the top plate; if the disc is moving at a velocity $(dz/dt) = v$ it will thereby induce a compensating current $i = -vQ/L$ which may be tapped from the top plate. If the experimental conditions are the same throughout the cell, then $Q(t)$ will be of the form

$$Q(t) = Q_0 e^{-\nu t} \tag{3}$$

so that we may then determine ν directly by measurement of $i(t)$.

In practice, of course, the cell must be finite in size, and the actual design reflects a desire to retain, as nearly as possible, a linear dependence of $q(z_0)$ upon z_0, as well as a correspondingly uniform field in the z-direction in the region traversed by the charged disc. Before discussing actual experimental cells it will be useful to discuss in a quantitative way the considerations entering into the cell design. The results are, for the most part, fairly obvious qualitatively in the light of the above theorem, but the actual magnitude and form of the deviations of the cell's performance from ideal behaviour are usually rather difficult to estimate without explicit calculation. It should be noted that, as a result of the peculiar $\bar{v}(E)$ relation (see I), the theorem cannot be applied quantitatively in any simple way to a disc of charge. This is because, even

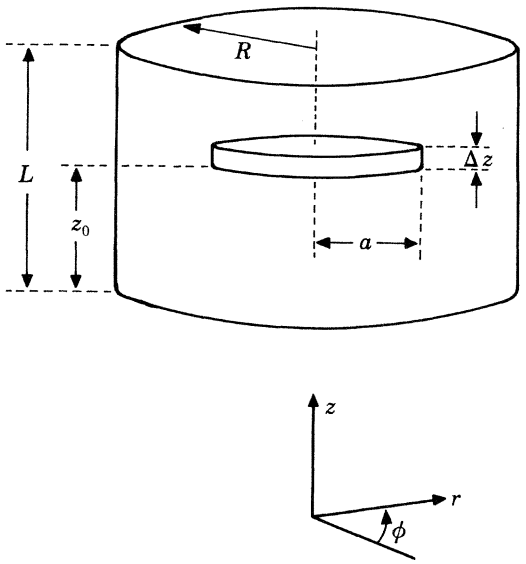

FIGURE 4. Model cell geometry, approximating the cells used for experimental measurements. The charge disc is of radius a and finite thickness Δz. The induction space is of radius R and length L and is bounded by a conducting wall. The coordinates are defined as shown.

though the disc may start out from an equipotential surface, it will not in general conform in shape to successive equipotential surfaces as it travels down the cell. (This behaviour will be followed accurately only in situations where $v \propto E^{-1}$ which, interestingly, is almost true for vortex rings at higher temperatures (Rayfield & Reif 1964); but it certainly is not the case for the free ions under consideration here.) It can, however, be shown that, under our experimental conditions, the motion of the ions is rather well approximated by the assumption that the disc is rigid.

It is convenient to discuss the behaviour of the real cells in terms of a model. As shown in figure 4, we consider a rigid disc-shaped volume of charge of radius a and thickness Δz moving up the z-axis of a cylindrical container of radius R and length L. The disc is not assumed necessarily to have a uniform charge density. We do assume, however, that the charge density is a function only of radial distance from the centre r, and of z, but not of angle ϕ. The cell walls (considered as a surface S) we assume to be perfectly conducting, although for the sake of the model we introduce the artificiality of an arbitrary potential distribution $\Phi(S)$. In practice the disc enters the induction space through a fine-mesh conducting wire grid in the bottom plate of the cell; this grid is designed to let the ions through while screening out as

much as possible any electric fields external to the cell. The disc is absorbed by the top plate once it has traversed the cell.

Clearly the motion (and indeed the detailed shape) of the disc is controlled only by the potential distribution $\Phi(S)$: we assume (as is the case in reality) that the induced charges on the walls due to the disc make a negligible contribution to $\Phi(S)$, so that $\Phi(S)$ is fixed externally; and we assume (as is also the case in reality) that space charge spreading of the disc may be neglected. The induced charge $q(z_0)$ that we measure depends only on the cell geometry and the shape of the collector plate (i.e. the region of the cell walls from which $q(z_0)$ is tapped).

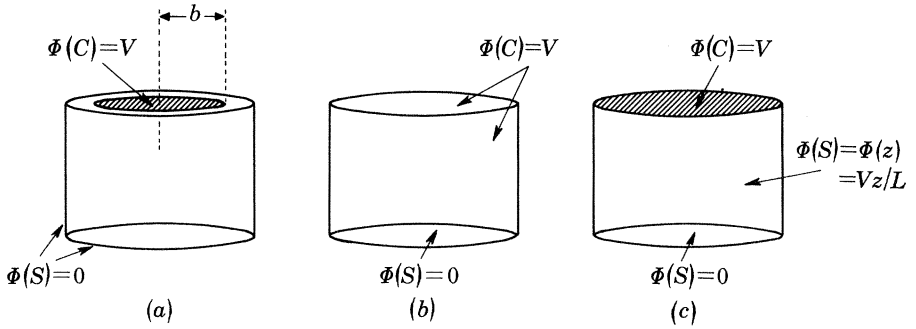

FIGURE 5. Three possible configurations of the collector and potential distribution for the model cell: (*a*) the collector (shaded) is a disc of radius b at potential V, while the walls and base are at zero potential; (*b*) the collector consists of the walls and top plate together, all held at potential V, but with the base still held at zero potential; (*c*) the collector (shaded) consists just of the top plate at potential V, the base is at zero potential and the walls are given a potential varying uniformly in z.

Three simple possibilities are shown in figure 5. In figure 5*a* the collector plate is a disc of radius b; in figure 5*b* it comprises the top plate (of radius R) and the entire side wall; while in figure 5*c* the collector plate consists just of the top plate. In each case the collector plate is held at a constant potential V. The side walls are held at zero potential in (*a*) and at V in (*b*), and in (*c*) they are given a potential varying uniformly with z (the collector plate still being at potential V).

In appendix A it is shown how the field distribution $\Phi_0(\boldsymbol{x})$ in these cells and the induced charge $q(z_0)$ on the collector plates may be calculated. Here we just quote and discuss the conclusions. Looking first at the results for $q(z_0)$, we find for an *infinitesimally thin* disc ($\Delta z \to 0$) the following:

for model cell (*a*)

$$q(z_0) = -Q\left\{\frac{z_0}{L}+\frac{4b}{a}\sum_{n=1}^{\infty}\frac{(-1)^n}{n\pi} \times \sin(n\pi z_0/L)\left[I_1(n\pi a/L)\left(K_1(n\pi b/L)+\frac{K_0(n\pi R/L)}{I_0(n\pi R/L)}I_1(n\pi b/L)\right)\right]\right\} \quad \text{for} \quad b \geqslant a, \tag{4a}$$

and

$$q(z_0) = -Q\left\{\left(\frac{b}{a}\right)^2\frac{z_0}{L}+\frac{4b}{a}\sum_{n=1}^{\infty}\frac{(-1)^n}{n\pi} \times \sin(n\pi z_0/L)\left[I_1(n\pi b/L)\left(K_1(n\pi a/L)+\frac{K_0(n\pi R/L)}{I_0(n\pi R/L)}I_1(n\pi a/L)\right)\right]\right\} \quad \text{for} \quad a \geqslant b; \tag{4b}$$

for model cell (b)

$$q(z_0) = -Q\left\{\frac{z_0}{L}+\frac{4L}{a}\sum_{n=1}^{\infty}\frac{\sin(n\pi z_0/L)}{(n\pi)^2}\frac{I_1(n\pi a/L)}{I_0(n\pi R/L)}\right\}; \tag{5}$$

and for model cell (c)

$$q(z_0) = -Q\left\{\frac{z_0}{L}+\frac{4L}{a}\sum_{n=1}^{\infty}\frac{(-1)^n}{(n\pi)^2}\sin(n\pi z_0/L)\frac{I_1(n\pi a/L)}{I_0(n\pi R/L)}\right\}. \tag{6}$$

In these equations $I_\nu(z)$ and $K_\nu(z)$ are hyperbolic Bessel functions. For properly designed cells the terms in equations (4)–(6) that are not linear in z_0 will be small. Examination of equations ($4a$) and ($4b$) reveals that this will be so provided that $[2R-(a+b)] \gg L$; similarly, if $(R-a) \gg L$ in equations (5) and (6).

If we now elaborate slightly by considering a non-uniformly charged disc, the results are somewhat more complicated but still easily interpreted. Allowing for a finite thickness Δz at the disc, with the charge distribution $\rho_{z_0}(\boldsymbol{x}')$ for a disc centred at a distance z_0 from the grid being given by

$$\rho_{z_0}(\boldsymbol{x}') = \frac{Q(z_0)}{\pi a^2}\theta(a-r')f(z, z_0) \quad \text{with} \quad \int f(z, z_0)\,\mathrm{d}z = 1$$

we obtain a new induced charge

$$\bar{q}(z_0) = \int \mathrm{d}z\, q(z) f(z, z_0)\, Q(z_0),$$

where $q(z)$ is the quantity appropriate to an infinitely thin disc. In the experiments the natural assumption to make is that $f(z, z_0)$ and $Q(z_0)$ take the combined form

$$f(z, z_0)\, Q(z_0) = Q_0 \frac{\nu\, \mathrm{e}^{-\nu z/\bar{v}}}{2\sinh(\nu\Delta z/2\bar{v})}\{\theta(z-z_0-\tfrac{1}{2}\Delta z)-\theta(z-z_0+\tfrac{1}{2}\Delta z)\},$$

that is, the charge density in the disc decays exponentially at a rate $\mathrm{e}^{-\nu z/\bar{v}}$ between the rear edge and the leading edge of the disc. If we integrate the exact expressions (equations (4)–(6)) for $q(z)$ in the above equation for $\bar{q}(z_0)$ we obtain rather unwieldy results, especially for the nonlinear terms; furthermore, they are of no great interest since the nonlinear terms only become significant at very low nucleation rates, when equations (4)–(6) are appropriate for the induced charge.

If we allow now for a variation of $\rho(\boldsymbol{x}')$ with r', then the nonlinear terms are multiplied by the factor (see appendix A)

$$\frac{n\pi Q}{aLI_1(n\pi a/L)}\int_0^a \mathrm{d}r'\, r'\rho(r')\, I_0(n\pi r'/L).$$

As we might expect, this factor is greater than 1 for $\rho(r')$ weighted towards large r' and less than 1 if charge is concentrated near the centre. In the experiments the charge density should in fact have been fairly uniform with, if anything, an increase near the centre.

Turning now to the function $\Phi_0(\boldsymbol{x})$ which describes the field in the cell due to the walls, we find that we must be rather careful to ensure that the charged disc is always moving through a region of constant field. For our three model cells, the r- and z-components of field are given by (see appendix A):

for model cell (a), with $r < b$,

$$E_z(\boldsymbol{x}) = -\frac{V}{L}\left\{1+\frac{2b}{L}\sum_{n=1}^{\infty}(-1)^n n\pi\cos(n\pi z/L)\left[I_0(n\pi r/L)+\frac{K_0(n\pi R/L)}{I_0(n\pi R/L)}I_1(n\pi b/L)\right]\right\}, \tag{7a}$$

$$E_r(\boldsymbol{x}) = -\frac{V}{L}\left\{\frac{2b}{L}\sum_{n=1}^{\infty}(-1)^n n\pi \sin(n\pi z/L)\left[I_1(n\pi r/L)\left(K_1(n\pi b/L)+\frac{K_0(n\pi R/L)}{I_0(n\pi R/L)}I_1(n\pi b/L)\right)\right]\right\}, \tag{7b}$$

and, with $r > b$,

$$E_z(\boldsymbol{x}) = \frac{V}{L}\left\{\frac{2b}{L}\sum_{n=1}^{\infty}(-1)^n n\pi \cos(n\pi z/L)\left[I_1(n\pi b/L)\left(K_0(n\pi r/L)-\frac{K_0(n\pi R/L)}{I_0(n\pi R/L)}I_0(n\pi r/L)\right)\right]\right\}, \tag{7c}$$

$$E_r(\boldsymbol{x}) = -\frac{V}{L}\left\{\frac{2b}{L}\sum_{n=1}^{\infty}(-1)^n n\pi \sin(n\pi z/L)\left[I_1(n\pi b/L)\left(K_1(n\pi r/L)+\frac{K_0(n\pi R/L)}{I_0(n\pi R/L)}I_1(n\pi r/L)\right)\right]\right\}; \tag{7d}$$

for model cell (b),

$$E_z(\boldsymbol{x}) = -\frac{V}{L}\left\{1+2\sum_{n=1}^{\infty}(-1)^n \cos(n\pi z/L)\frac{I_0(n\pi r/L)}{I_0(n\pi R/L)}\right\}, \tag{8a}$$

$$E_r(\boldsymbol{x}) = \frac{-2V}{L}\sum_{n=1}^{\infty}(-1)^n \sin(n\pi z/L)\frac{I_1(n\pi r/L)}{I_0(n\pi R/L)}; \tag{8b}$$

and for model cell (c),

$$E_z(\boldsymbol{x}) = -V/L, \quad E_r(\boldsymbol{x}) = 0. \tag{9}$$

It is interesting to sketch the field lines and equipotentials in the three model cells described by these equations (see figure 6). There is of course an unphysical discontinuity in potential at the edges of the collector plates in figure 6*a*, *b*, which in a real cell will be removed by a thin layer of nylon insulation between the collector plate and the rest of the cell, but apart from this the drawings give an accurate picture of the field distribution inside the cell. It will be clear from the diagrams how important it is that the disc should travel in the central regions of the cell, in order that the nonlinear terms in equations (7)–(9) be small.

It is not possible to calculate exactly the effect of slightly separating the collector plate from the rest of the cell and inserting insulation material in the resultant space: this is an intractable problem with complicated mixed boundary conditions. However, we can see from the sketches of figure 6 that, provided that the collector plate is large, the effect of doing this will be small (there are two effects to consider; the effect of 'field leakage' outside the cell due to the gap, and the tendency of the nylon insulation, with a larger dielectric constant than ^{4}He, to 'drag' field lines into itself. Both of these effects enhance the nonlinearities in field).

Another possible source of field distortion arises from 'leakage' through the fine-mesh wire grid at the bottom of the cell. (We assume, which was the case in practice, that the field outside the induction space is smaller than that inside the space.) While a solution of Laplace's equation for the full three-dimensional problem would be rather difficult, we may place an *upper bound* on the errors introduced by considering the simpler two-dimensional problem in which the collector plate is treated as an infinite conducting plane and the grid as a line of equally spaced parallel infinite wires. This is because the shielding power of the three-dimensional grid is necessarily *greater* than that of the hypothetical two-dimensional grid. The problem is easily solved by mapping it onto an equivalent complex variable problem. Let us make the

PHILOSOPHICAL TRANSACTIONS OF THE ROYAL SOCIETY A MATHEMATICAL, PHYSICAL & ENGINEERING SCIENCES

assumption that $L \gg \beta \gg \alpha$, where β is the spacing between the wires and α is their radius: the first condition is invariably well satisfied in practice ($L/\beta > 100$); and the applicability of the second condition is discussed below. If we use the coordinate system of figure 3, and place the origin at the centre of one of the wires, we obtain for the potential

$$\Phi_0(z, r) = V\left\{1 - \left[\frac{4\pi L}{\beta} + 2\ln\left(\frac{\beta}{2\pi d}\right)\right]^{-1} \ln\left[\frac{\sin^2(\pi x/\beta) + \sinh^2[\pi(y-2L)/\beta]}{\sin^2(\pi x/\beta) + \sinh^2(\pi y/\beta)}\right]\right\}. \quad (10)$$

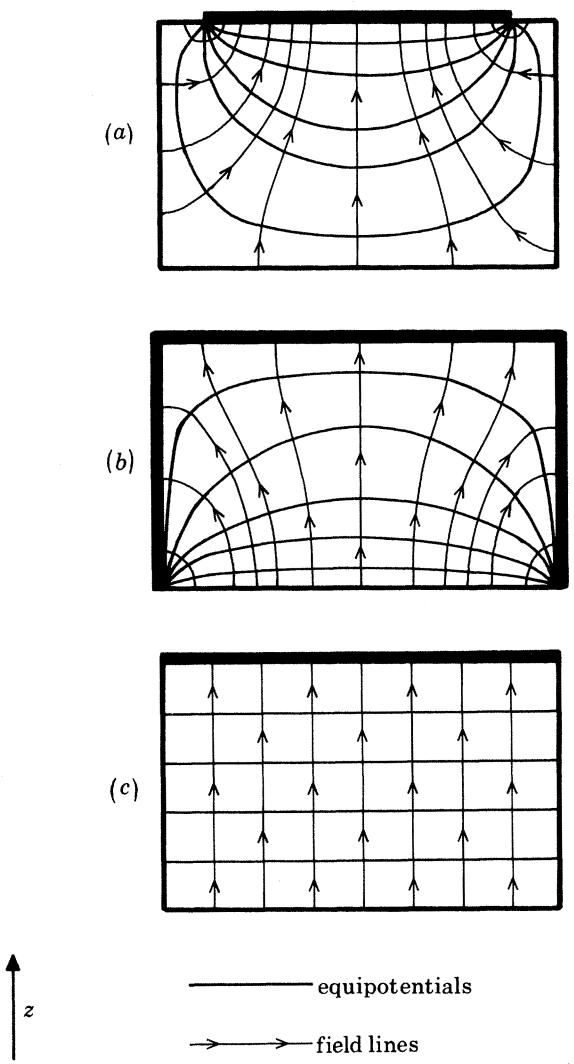

FIGURE 6. Lines of electric field (arrowed) and equipotentials for the three model cells of figure 5. Lines representing the collector region have been thickened.

The solution may be imagined pictorially by the usual device of comparing it with the problem of a piece of stretched rubber fixed to a line of infinite parallel wires and a flat plane. It will be clear that, for a line of closely spaced wires, the field will be fairly uniform once an ion has moved from the immediate vicinity of the wires: the real problem is to make sure that no ion travelling between two wires can traverse a path from $z = 0$ to $z = L$ over which the potential difference is significantly less than V. The worst possible case would be for an ion

travelling midway between two wires: at a point $(z = 0, r = (n+\frac{1}{2})\beta)$ where $n = 0, \pm 1, \pm 2, \ldots$ the potential is given by

$$\Phi_0(0, \tfrac{1}{2}\beta) = V\left\{1 - \frac{\ln\left[1+\sinh^2(2L/\beta)\right]}{4\pi L/\beta + 2\ln(\beta/2\pi\alpha)}\right\}$$
$$\approx 2V[\ln(\beta/8\pi\alpha)]/[\chi + 2\ln(\beta/2\pi\alpha)],$$

where
$$\chi = 4\pi L/\beta \gtrsim 1500.$$

In the actual experiments $\beta \approx 8\alpha$ so that $\Phi_0(0, \frac{1}{2}\beta)$ would be a negligible fraction of V. It may be objected that, under these conditions, the inequality leading to (10) is no longer valid and that, consequently, (10) cannot be considered accurate. None the less, it will be clear that thickening the grid wires while leaving β and L constant will merely decrease $\Phi_0(0, \frac{1}{2}\beta)$, thus *increasing* the efficacy of the shielding. It is evident, therefore, that the above estimate of $\Phi_0(0, \frac{1}{2}\beta)$ provides an upper bound for the effects of field leakage and demonstrates them to be negligible.

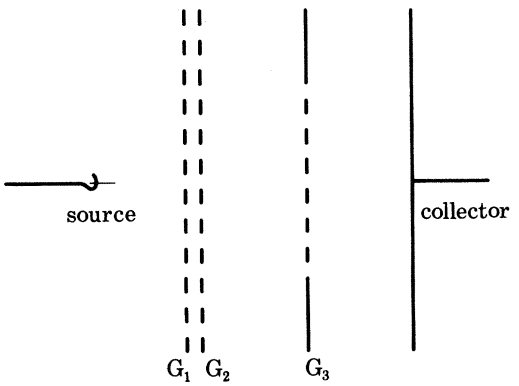

FIGURE 7. The electrode structure used for vortex nucleation measurements (diagrammatic). Ions from the field emission source are gated into a thin disc by means of a voltage pulse applied to the gate formed by grids G_1 and G_2. The signal is induced in the collector while the charge disc is travelling under the influence of a strong uniform electric field between G_3 and collector.

(*b*) *The experimental cell*

The form of the electrode structure needed for the experiments is indicated in figure 7. The induction space is between grid G_3 and collector. The grids G_1 and G_2 enable ions generated by the field emission source to be gated into a disc (as in I and II), which then proceeds towards G_3 under the influence of a modest assisting electric field. During its passage across G_2–G_3, transients induced in the detection circuit by the gating pulse applied to G_1 have time to die away, so that the electrostatic induction signal rises from a stable baseline as the ions pass through G_3. A diaphragm, on which G_3 is mounted, is used to limit the radius of the charge disc.

The electrode structure used in practice for most of the measurements is shown in figure 8. As in II, nickel grids were mounted on mild steel electrodes so that the grids would, if anything, tighten on cooling down. The assembly slides into the nylon sleeve and pressure chamber already described (see §2*a* and fig. 1 of II). The current induced in the collector is inevitably rather small in this type of arrangement compared to that in the velocity cells of I and II, being reduced by a factor approximately equal to the ratio of the thickness of the charge disc and the G_3–collector spacing. In an attempt to mitigate this difficulty, the single field emission source used previously was replaced with an array of ten sources arranged so as to 'illuminate'

PHILOSOPHICAL TRANSACTIONS OF THE ROYAL SOCIETY A MATHEMATICAL, PHYSICAL & ENGINEERING SCIENCES

G_1 with ions as uniformly as possible and positioned about 1.5–2.0 mm from G_1. This smaller separation had the effect of increasing the emission from each individual tip, the magnitude of which is apparently controlled by spacecharge built up on an enveloping tangle of vorticity (Phillips & McClintock 1975).

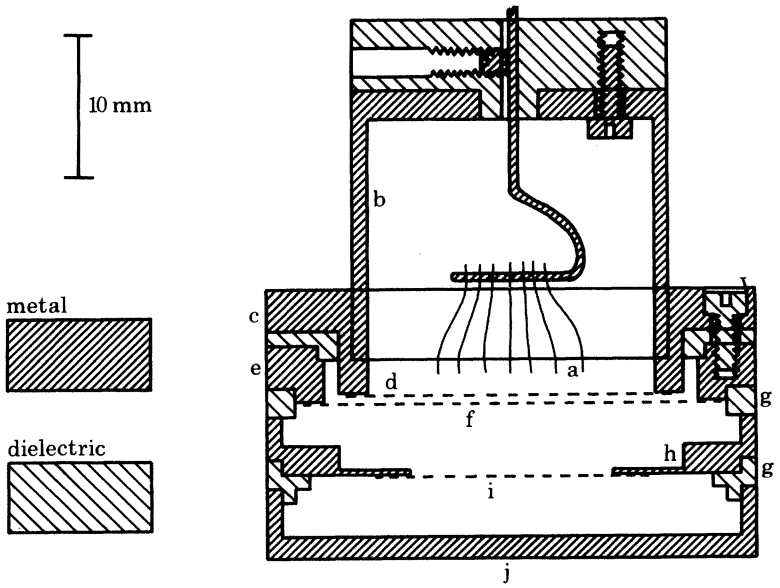

FIGURE 8. The electrode structure used in practice, slightly modified so as to appear in a single vertical section: a, set of ten tungsten field emission tips, spot-welded to a nickel wire; b, brass backplate; c, mild steel electrode to carry G_1, in electrical contact with backplate; d, nickel grid G_1; e, mild steel electrode to carry grid G_2; f, nickel grid G_2; g, nylon insulator; h, mild steel diaphragm to carry grid G_3; i, nickel grid G_3; j, collector.

It is clear from the discussion in §2*a* that, to minimize the nonlinear terms in equations (4)–(6), the induction space should be made as short and as wide as possible, and the radius of the charge disc should be restricted. In reality, of course, practical considerations limit the extent to which these ideals can be met. The overall diameter is restricted by the space available in the cryostat; the length of the induction space must be sufficient to provide a free transit time for the ions which does not differ by more than one or two orders of magnitude from the expected extreme values of ν^{-1}; and the aperture of the diaphragm must not be so restricted that the signal/noise ratio becomes inadequate.

We now address the question, therefore, of the errors in ν that will arise if we analyse data acquired from the real (non-ideal) cell but using equation (3) rather than the exact forms (4)–(6). We will consider, in particular, model cell (*b*) of figure 6, which bears the closest resemblance to the cell (figure 8) used for most of the measurements reported below. It may be noted that the charge disc traverses a region sufficiently far away from the areas of field leakage and nylon insulation that it effectively does not see them, and so the model cell adequately describes the situation. Ignoring the terms in equation (5) beyond $n = 1$, we find for the collector current

$$i(z_0) = \bar{v}\frac{\partial q(z_0)}{\partial z_0} = -\bar{v}\,\mathrm{d}Q\,\frac{\partial}{\partial z_0}\left\{\frac{z_0}{L} + \delta \sin\frac{\pi z_0}{L}\right\}, \tag{11}$$

where

$$\delta = \frac{4L}{\pi^2 a}\,\frac{I_1(\pi a/L)}{I_0(\pi R/L)}. \tag{12}$$

This is the contribution to the collector current from an infinitesimally thin charge disc of total charge $\mathrm{d}Q$, positioned at z_0 and moving at velocity $\bar{v}$. The current arising from the motion of a thick disc, thickness L/α_1, will therefore be

$$i(z_0) = \int_{z_0}^{z_0+L/\alpha_1} -\bar{v}\,\mathrm{d}Q\,\frac{\partial}{\partial z_0}\left\{\frac{z_0}{L}+\delta\sin\frac{\pi z_0}{L}\right\}. \tag{13}$$

By writing $\mathrm{d}Q = \pi a^2\rho'\,\mathrm{d}z_0$, where ρ' is the average density of free charge, and integrating, (13) becomes

$$i(z_0) = -\bar{v}\pi a^2\rho'\left\{\frac{1}{\alpha_1}+\delta\sin\left(\frac{\pi z_0}{L}+\frac{\pi}{\alpha_1}\right)-\delta\sin\frac{\pi z_0}{L}\right\}. \tag{14}$$

We note that (14) displays the correct limiting behaviour as $\alpha_1 \to 1$: as the entire induction space fills with charge, z_0 tends to zero for a freely moving charge disc, the terms in δ vanish, and $i(z_0)$ becomes equal to the d.c. current entering the volume. We wish to estimate the apparent nucleation rate ν_0 which will be measured under conditions such that no vortex nucleation is taking place. In practice, we invert (3) and may then determine the nucleation rate from

$$\nu_0 = t^{-1}\ln(i_\mathrm{m}/i_\mathrm{f}), \tag{15}$$

where i_m and i_f are the maximum and final values of $i(z_0)$ on the top of the signal, separated by the disc transit time t. (In reality, we perform a least squares fit to the whole of the top of the signal (see §2*d*), but the difference from the ν_0 found by using (15) will not be great.) The currents i_m and i_f correspond respectively to $z_0 = 0$ and $z_0 = L - L/\alpha_1$, so that from (14) we obtain

$$i_\mathrm{m} = -\bar{v}\pi a^2\rho'[\alpha_1^{-1}+\delta\sin(\pi/\alpha_1)], \tag{16}$$

and

$$i_\mathrm{f} = -\bar{v}\pi a^2\rho'[\alpha_1^{-1}-\delta\sin(\pi/\alpha_1)]. \tag{17}$$

Substituting in (15), using the fact that $t = (L-L/\alpha_1)/\bar{v}$ is the relevant time (that is, the time during which the disc of charge moves freely within the induction space), and assuming that $\alpha_1\delta \ll 1$, we find

$$\nu_0 = \frac{2\alpha_1\bar{v}}{L(\alpha_1-1)}\ln[1+\alpha_1\delta\sin(\pi/\alpha_1)]. \tag{18}$$

The value of α_1 chosen in practice amounted to a compromise between using a disc thick enough to provide adequate signal/noise and having a disc thin enough to ensure that the time $(L-L/\alpha_1)/\bar{v}$ was long enough for the measurement to be made with sufficient accuracy: the value used was typically $\alpha_1 = 3.5$. On this assumption, we plot in figure 9 the values of $\nu_0 L/\bar{v}$ that would be expected for a number of different cell geometries. The curves are calculated on the basis of equation (18), but they are plotted in terms of dimensionless variables to facilitate estimating ν_0 for a variety of cells.

We must emphasize that the curves of figure 9 represent estimates for model cell geometries that take no account of possible radial inhomogeneities in the charge density within the disc. None the less, they are of considerable assistance in designing cells. The general philosophy has been to choose the geometry in such a way as to ensure that the estimated ν_0 was no greater than the average random error (*ca.* 50–100 s^{-1} for our *ca.* 5 mm cells) in the measurements of small ν. The acid test was then to measure ν_0 at 25 bar for fairly weak electric fields when, as described below, we can be confident that the vortex nucleation rate was negligible: the average measured value of ν_0 could then be used as a small correction to be subtracted from

all values of ν measured in that cell. When the design philosophy mentioned above was used, the correction was of course expected to be negligible except at small ν.

The relevant dimensions of the cell used for most of the experiments (figure 8) were $R = 16$ mm and $a = 6.75$ mm; and the length, measured at room temperature and adjusted to allow for thermal contraction, was $L = 4470\ \mu\text{m} \pm 2\,\%$ at helium temperatures. The length required to give agreement with the Landau velocity at 25 bar as calculated from roton parameters (see §4*a* below) was some 0.56 % smaller, which is, however, well within the estimated uncertainty

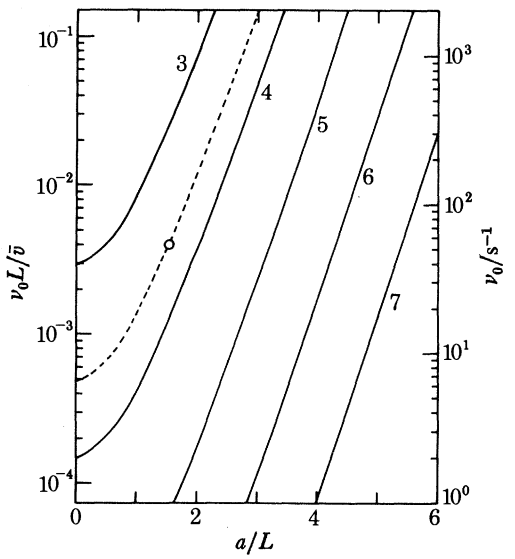

FIGURE 9. The systematic error ν_0 expected in ν as a result of making measurements with the model cell of figure 5*b* rather than the idealized geometry of figure 3. The curves are calculated from equation (18) on the assumption that $\alpha_1 = 3.5$, and are plotted in terms of the dimensionless variables $\nu_0 L/\bar{v}$ and a/L for a number of different values of R/L as indicated by the number adjacent to each curve. The dashed curve corresponds to the particular cell shown in figure 8, for which $R/L = 3.6$: the resulting values of ν_0 are plotted on the right ordinate. For the diaphragm used in practice, $a/L = 1.52$. The corresponding operating point is indicated by the circle and implies that measurements with this cell would be expected to suffer from a systematic error in the region $\nu_0 \approx 65\ \text{s}^{-1}$ if all other non-idealities in the signal acquisition system could be ignored. (In practice a small *negative* systematic error was found: see text.)

in the direct measurement. Accordingly, in the interests of consistency with the set of roton parameters used in §4 for analysis of the experimental data, we have taken the length of the induction space to be 4445 μm. The dashed line in figure 9 indicates the calculated locus of operating points for the cell of figure 8, with use of a variety of diaphragm apertures; the circled point corresponds to the chosen aperture of 6.75 mm radius. Taking an averaged value of $\bar{v} = 60\ \text{m s}^{-1}$ (since the absolute value of $\bar{v}$ does not vary greatly), we find the values of ν_0 shown on the right ordinate. For the cell of figure 8, therefore, we would expect to measure a ν_0 of *ca.* $53\ \text{s}^{-1}$.

Finally, we consider the extent to which the electric field traversed by the charge disc may be regarded as uniform. Inserting the relevant dimensions into equation (7) for $\boldsymbol{x} = (z, r = a)$, we find

$$E_z(z, a) = -(V/L)\{1 + 4.59 \times 10^{-3} \cos(\pi z/L) + \text{negligible terms}\},$$

$$E_r(z, a) = -(V/L)\{4.10 \times 10^{-3} \sin(\pi z/L) + \text{negligible terms}\}.$$

The deviations in $\mathbf{E}(\boldsymbol{x})$ at the edge of the charged disc are small but by no means negligible. A glance at figure 6*b* shows that the disc slightly expands in radius during its traversal of the cell, and that it will become very slightly distorted (bare ions in the disc will almost exactly follow the field lines, although the nonlinear dependence of velocity on field makes the exact shape of the disc at any time rather complicated to calculate). However, the fractional deviations in $E_z(z, a)$ are always less than 0.45 %, which means (since $\bar{v}-v_L \propto E^{\frac{1}{3}}$) that at no point during the traversal of the cell will any ion in the disc be moving more than 0.15 % faster than any other. The radius of the ring will be $(2/\pi) \times 0.41\ \% \approx 0.26\ \%$ larger when $z_0 = L$ than when $z_0 = 0$.

(*c*) *Electrical circuitry and electronics*

The principal features of the control circuitry and measurement system are illustrated in figure 10.

A pair of Hewlett Packard 214A pulse generators and an extra high tension (e.h.t.) amplifier are used to operate the ion source and gate essentially as described in I, creating a coin-shaped disc of charge travelling from G_2 towards the collector C. As soon as the ions pass G_3, a current is induced in C. Because a substantial proportion of the ions are caught on G_3, however, there is a tendency for the potential of G_3 to change as the ions reach it. This effect, which, through the stray capacitance between G_3 and C, could have had a fatally deleterious effect on the signal shape, was minimized by a large (0.8 μF) capacitor between G_3 and earth. To withstand the required working voltage of up to 5000 V on G_3, this capacitor was formed from ten 600 V × 8 μF electrolytic capacitors in series, with a stabilizing resistor in parallel with each element. The necessary d.c. potential differences between G_1G_2 and G_2G_3 were obtained from batteries with associated potentiometric dividers and voltmeters, floated on top of the G_3 potential. In normal use, the gate G_1G_2 was held shut by 10 V and an assisting potential difference of 180 V was applied between G_2 and G_3. The necessary 5000 V bias for electrodes other than C was taken from a standard Brandenberg Alpha Series II stabilized e.h.t. generator, and measured by means of a digital voltmeter connected via the 1:1000 divider.

The transient current pulse induced in C was taken to earth through a 5.4 kΩ resistor, this value being chosen so as to make the frequency response of the collector circuit comparable with that of the 2 MHz Brookdeal 9454 amplifier connected to the high side of the resistor. The output of the amplifier was digitized by a Biomation 8100 transient recorder, which was triggered after a suitable delay. The digital signal was then passed to the Nicolet Instruments 1080 minicomputer which was used both to sum a large number of like signals to enhance signal/noise, and for the analysis of the averaged signals (see §2*d*). The process was repeated at a repetition rate of up to 25 Hz until acceptable signal/noise had been achieved, as indicated by display 2, after which the signal could be transferred to magnetic 'floppy' disc to be stored for subsequent examination or reanalysis, as desired. Display 1 exhibited the contents of the transient recorder memory. To minimize the residual effects of external electrical interference, much of which was coherent with the mains supply even although it did not reach the amplifier by this route, the master trigger produced pulses that were synchronized to the mains but whose mean position could be adjusted in relation to the 50 Hz peaks. In this way, it was usually possible to find a position on the mains cycle that was free of noise. To avoid inadvertently enhancing any mains coherent noise that existed below the random noise on the signal, the exact triggering point was usually oscillated linearly at a few tenths of a hertz about its mean position on the cycle.

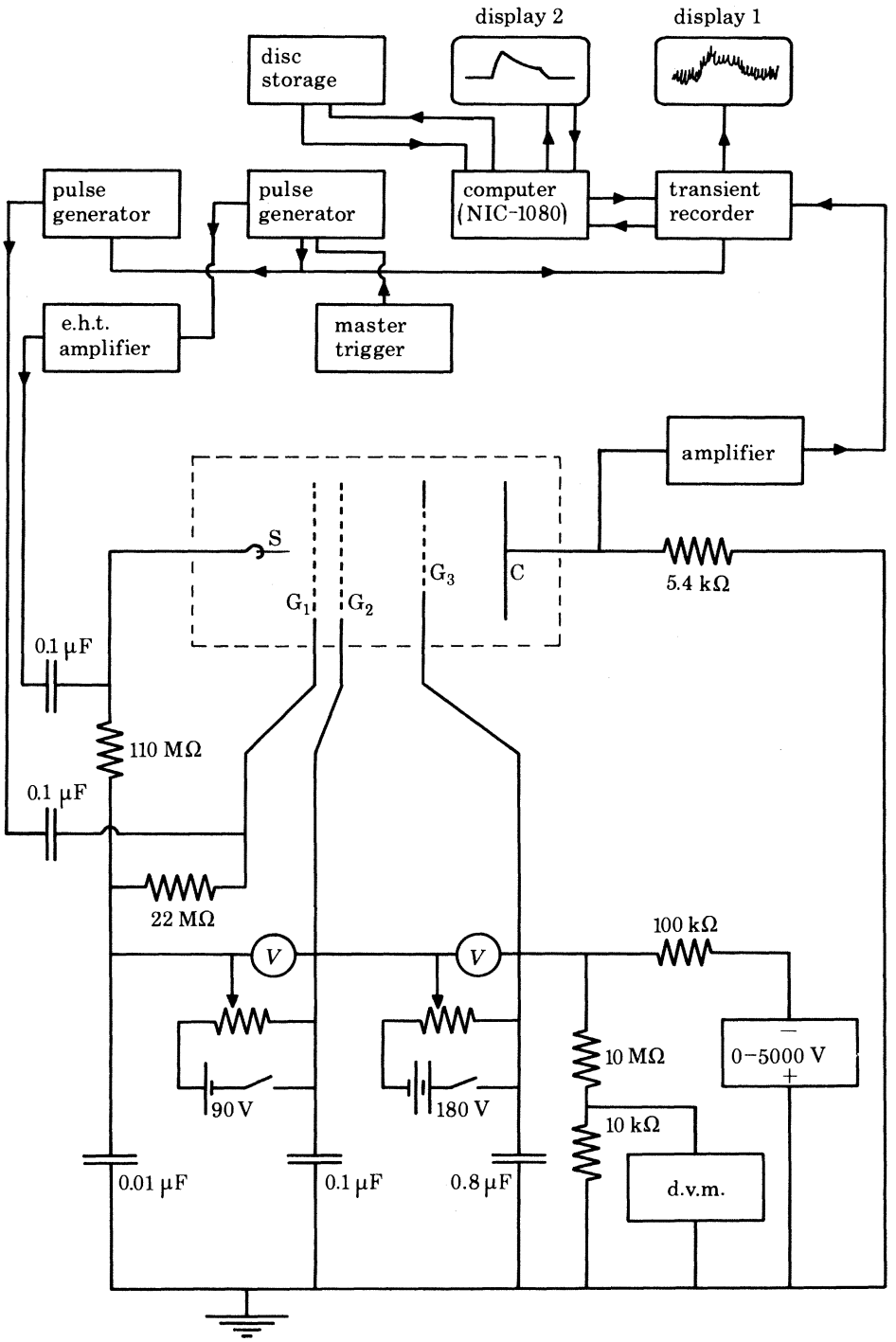

FIGURE 10. Block diagram of the electrical circuit used in making the vortex nucleation rate measurements. Components inside the dashed line represent the electrodes of the experimental cell, which is filled with pressurized He II at *ca.* 0.5 K. All the other components are at room temperature.

(*d*) *Signal analysis*

A charge disc of finite thickness would be expected to induce in the collector a signal of the shape sketched in figure 11: t_1 is the time at which the leading edge of the disc reaches G_3 (see also figure 7); t_2 is the time at which the trailing edge passes G_3; between t_2 and t_3 the disc travels freely within the induction space between G_3 and C; and t_3 and t_4 correspond respectively to the times at which the leading and trailing edges reach C. The principal items of information that can be extracted from such a signal are: (i) the magnitude of ν, by measuring the exponent of the decreasing signal between t_2 and t_3; (ii) the magnitude of $\bar{v}$, by measuring the time of flight across G_3–C which can be obtained from either (t_3-t_1) or from (t_4-t_2).

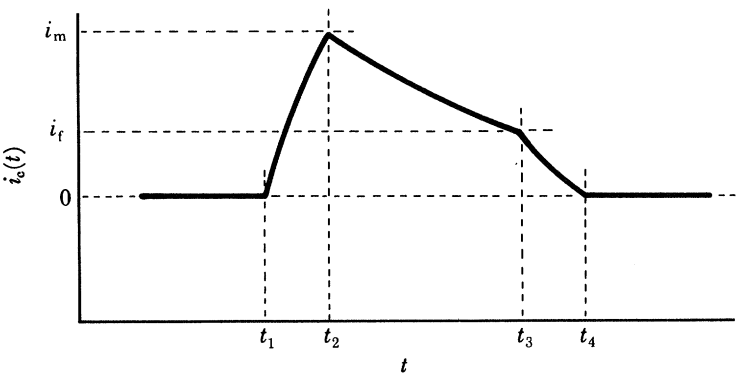

FIGURE 11. Idealized collector signal to be expected when a charge disc of length t_2-t_1 in time travels from G_3 to collector (figure 7). The collector current i_c is plotted as a function of time t. Between t_1 and t_2 the disc is entering the induction space; between t_2 and t_3 the disc moves freely, decaying exponentially as it travels owing to vortex ring production; and between t_3 and t_4 it passes into the collector. Equations (21)–(29) define the detailed shape of the signal.

To identify the points $t_1 \ldots t_4$, equations were fitted to the adjacent regions of the signal in each case. The base is, of course, a straight line; but the sides and top of the signal are curves unless ν is zero. In deriving the corresponding equations we assume that the nonlinear terms in equation (5) may be ignored, so that the collector current may be written as

$$i(t) = Q(t)\,\bar{v}/L$$

or

$$i(t) = (\pi a^2 \bar{v}/L) \int \rho(z)\,\mathrm{d}z, \tag{19}$$

where $\rho(z)$ is the average density of free charge which, for finite ν, will decrease owing to nucleation events as the disc travels down the chamber. Since

$$\rho = \rho_0 \mathrm{e}^{-\nu z/\bar{v}},$$

where ρ_0 is the charge density in the disc at $z = 0$, (19) becomes

$$i = (i_0/L) \int \mathrm{e}^{-\nu z/\bar{v}}\,\mathrm{d}z, \tag{20}$$

where $i_0 = \pi a^2 \rho_0 \bar{v}$ is the local current passing G_3. The limits of integration of (20) needed to describe the leading edge, top and trailing edge of the signal are respectively: zero to $\bar{v}t$, with t running from zero to Δt; $\bar{v}(t-\Delta t)$ to $\bar{v}t$, with t running from Δt to $L/\bar{v}$; $\bar{v}(t-\Delta t)$ to L, with t

running from $L/\bar{v}$ to $(L/\bar{v}+\Delta t)$. Here, Δt is the time width of the disc of charge. By integrating and inserting the limits, it is straightforward to show that:

for the rising edge $$i = A+B\mathrm{e}^{Dt}; \tag{21}$$

for the top $$\ln i = C+Dt; \tag{22}$$

and for the falling edge $$i = E+F\mathrm{e}^{Dt}. \tag{23}$$

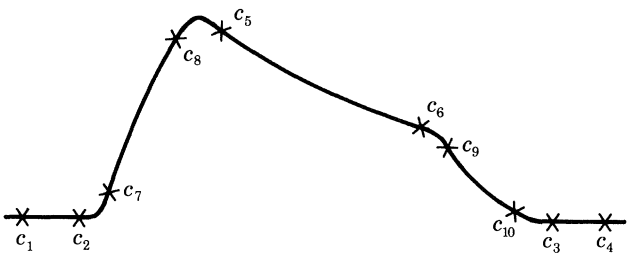

FIGURE 12. Cursor settings used in fitting equations (21)–(23) to the signals, as described in the text. Cursors were kept clear of the corners of the signal in each case, to minimize errors resulting from the finite rise time of the collector circuit.

The constants are given by

$$A = i_0\bar{v}/Lv \tag{24}$$

$$B = -A\mathrm{e}^{vt_1} \tag{25}$$

$$C = \ln\left[A(\mathrm{e}^{vt}-1)\,\mathrm{e}^{vt_1}\right] \tag{26}$$

$$D = -v \tag{27}$$

$$E = -A\mathrm{e}^{-vL/\bar{v}} \tag{28}$$

$$F = A\mathrm{e}^{v(t_1+\Delta t)}, \tag{29}$$

where we have shifted the origin of time such that $t = t_1$ as the front of the charge disc reaches G_3, in accordance with figure 11. The times $t_1 \ldots t_4$ may then be expressed in terms of the constants $A \ldots F$, as

$$t_1 = D^{-1}\ln(1-A/B), \tag{30}$$

$$t_2 = D^{-1}\ln\left[(A-B)/(\mathrm{e}^C-B)\right], \tag{31}$$

$$t_3 = D^{-1}\ln\left[(E-F)/(\mathrm{e}^C-F)\right], \tag{32}$$

$$t_4 = D^{-1}\ln(1-E/F). \tag{33}$$

The equations (21)–(23) were fitted to the signals by means of the same NIC-1080 minicomputer that was used for averaging. The appropriate regions of the signal were specified by using a pair of electronic cursors which could be positioned to the settings shown in figure 12 by means of parameter knobs on the front of the computer. Values of v and $\bar{v}$ and other relevant information were calculated and printed. In doing so, the magnitude of v was found from (27) and that of $\bar{v}$ from the average ionic transit time

$$\bar{v} = 2L/(t_3-t_1+t_4-t_2), \tag{34}$$

by using equations (30)–(33).

The quantity $$\delta_s = 200(t_4 - t_3 - t_2 + t_1)/(t_4 + t_3 - t_2 - t_1), \quad (35)$$

gave the increase in the thickness of the disc as a percentage of the transit time and provided an indication of the axial spreading of the disc due to space charge or other effects. The current passing through G_3, i_0, was found from (24) and the maximum induction i_m in the collector (that is, the signal magnitude at t_2) was computed from

$$i_m = e^{(C+Dt_2)}. \quad (36)$$

It should be noted that $i_m < i_0$ for all situations in practice where the disc thickness is less than L.

To avoid digital rounding off problems in cases where ν was very small, a somewhat different procedure was followed. Where $\nu < 200\ s^{-1}$ the sides were fitted by using linear equations rather than (21) and (23). The top was re-fitted, also by using a linear equation in place of (22), and the intersection points $t_1 - t_4$, $\bar{v}$, δ_s, i_0 and i_m were calculated on this basis, rather than by using the procedure described above; but the initial value of ν from (22) and (27) was retained for printing. Under such circumstances the signal is composed of lines that are virtually straight, and it is not at all surprising, therefore, that, close to ν_c, the difference in values of $\bar{v}$ calculated by using the two methods was undetectable.

On completion of signal analysis the physical conditions, parameter settings and values of ν, $\bar{v}$, δ_s, i_e, i_m and other answers from the analysis were all overlaid on the extreme right edge of the signal, before it was stored on disc.

(*e*) *Data handling*

It was found (see §3*a*, *b*) that ν is a strong function of four independent variables: P, T, E and the ^{3}He isotopic concentration x_3. The task of mapping out the behaviour of ν within this multi-dimensional space necessitated the acquisition and analysis of some thousands of individual signals even while, for the present phase of the research programme, x_3 has been kept fixed at zero. The manipulation and tabulation of this large body of data have been greatly eased by the use of a special data handling program in conjunction with the NIC-1080 minicomputer. The program was designed to go through the signals stored on a series of floppy discs, to extract the overlaid set of parameter values and to store this information in packed form on a data collection disc. Selected data could then be tabulated or transferred to a NIC-1180E minicomputer for plotting, with use of the associated Zeta digital graph plotter.

3. Experimental results

A total of more than 2000 vortex induction signals have been acquired, analysed and stored by the methods described in the preceding section. In §3*a* we discuss how the signal shapes observed in practice compare with the idealized shape defined by equations (21)–(23); and we present a representative selection of the recorded signals. The vortex nucleation rates and velocities extracted by analysing the signals are presented in §3*b*, *c* respectively.

(*a*) *Vortex induction signals*

Figure 13*a* shows the active section of a complete signal cycle as recorded on display 2 for the physical conditions stated in the caption. The transients A, B and C correspond respectively to the field emission source being switched on and to the gate opening and shutting. The

PHILOSOPHICAL TRANSACTIONS OF THE ROYAL SOCIETY A MATHEMATICAL, PHYSICAL & ENGINEERING SCIENCES

electrostatic induction signal starts at D, and the source is finally switched off again at E. Normally, the sampling interval and trigger delay on the transient recorder were set so as to concentrate only on the induction signal itself, as shown in figure 13*b* (since the positions of the transients are not needed). The basis of the technique for measuring ν depends, of course, on the belief that the decaying top section of such a signal will be exponential in form: this belief may be vindicated by taking the logarithm of the signal, as shown in figure 13*c*, clearly exhibiting a linear top.

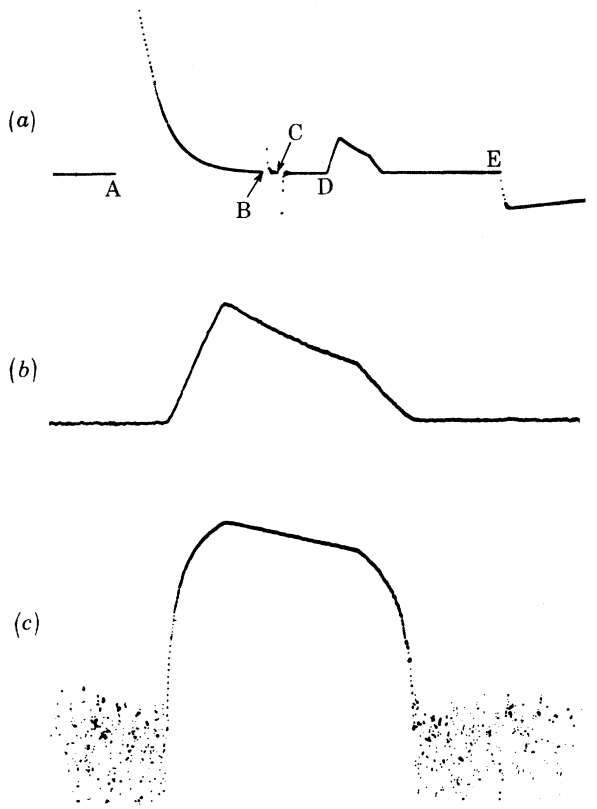

FIGURE 13. Typical signals recorded at the collector. (*a*) The collector current i_c displayed as a function of time t, with the sampling rate of the transient recorder set so as to include the active section of a complete signal cycle. The transients at A and E, separated by 540 μs, correspond respectively to the field emission source (figure 7) being switched on and off, and those at B and C to the gate formed by G_1 and G_2 opening and shutting. The actual induction signal, which starts at D corresponding to the moment when the front of the charge disc first penetrates G_3, looks very similar to the expected signal of figure 11. The physical conditions under which the signal was recorded were: $P = 21$ bar; $T = 0.595$ K; $E = 1.01 \times 10^6$ V m^{-1}. (*b*) Signal recorded under conditions identical to those for (*a*), but with sampling rate and trigger delay set so as to concentrate on the vortex induction signal itself. (*c*) The logarithm of the signal shown in (*b*), with a linear top section demonstrating exponential decay of the bare ion signal.

A stringent test of the analysis presented in the previous sections is to compute the difference between a signal such as that shown in figure 13*b* and the idealized replica constructed by fitting equations (21)–(23) to the signal. The replica is shown in figure 14*a*. It looks similar to the signal itself apart, of course, from the absence of electrical noise and absence of the slight rounding caused by the finite rise time of the collector circuit. The difference between the signal and replica is shown in figure 14*b*, *c*; apart from some 'spikes' due to the rounding, the

subtraction yields random electrical noise, centred on zero and entirely devoid of the systematic deviations that would be expected if equations (21)–(23) did not properly describe the form of the signal.

To evaluate the correction ν_0 required to take account of non-idealities in the electrode structure and circuitry (see §2*a*, *b*), a number of induction signals were recorded under conditions such that the vortex nucleation rate is believed to be negligible (that is, high P, low E, low T: see below). An example of one such signal is shown in figure 15*a*. The discussion of §2*b* shows that, under these circumstances, a very small negative gradient of the top of the signal is to be expected, corresponding to a small positive value of ν_0. Figure 15*b*, however, in

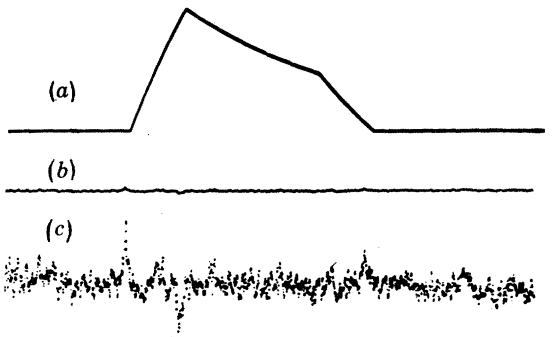

FIGURE 14. Test of the applicability of equations (21)–(23) to the signal shapes obtained in practice. (*a*) Idealized replica constructed from the parameters derived by fitting equations (21)–(23) to the signal shown in figure 13*b*. (*b*) Result obtained by subtracting the idealized replica of (*a*) from the signal of figure 13*b*, plotted on the same ordinate scale. (*c*) Result of subtraction, just as in (*b*), but with the vertical scale now magnified by a factor of 16.

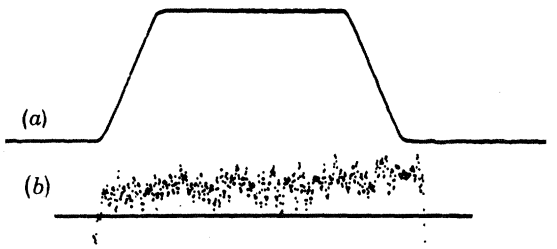

FIGURE 15. (*a*) Signal obtained for $P = 25$ bar, $T = 0.305$ K, $E = 9.0 \pm 10^4$ V m^{-1}. Under these conditions it is believed that ν is negligible, so that it becomes possible to measure the nucleation rate zero correction ν_0. (*b*) The top section of the signal in (*a*), but with the vertical scale multiplied by 32 to demonstrate the small positive gradient corresponding to $\nu_0 = -52 \pm 20$ s^{-1}.

which the top of the signal has been magnified by 32, clearly demonstrates that this was not the case in practice: the gradient, although small, is definitely *positive*. We conclude that the contribution to the net systematic error arising from the use of a finite electrode geometry was outweighed by other contributions that were of opposite sign. These are believed to arise from non-idealities of the signal acquisition circuitry including, in particular, the response characteristics of the preamplifier. It must be emphasized, however, that the resultant net systematic error is extremely small. It corresponds to an apparent increase of about 0.2 % in the current during the free passage of the charge disc across the induction space. Analysis of the signal of figure 15 by the standard procedures outlined in §2*d* yielded $\nu_0 = -52 \pm 20$ s^{-1}, where the quoted error refers to the deviations observed during several successive analyses with use of slightly different cursor setting positions on each occasion. From analyses of a number of such

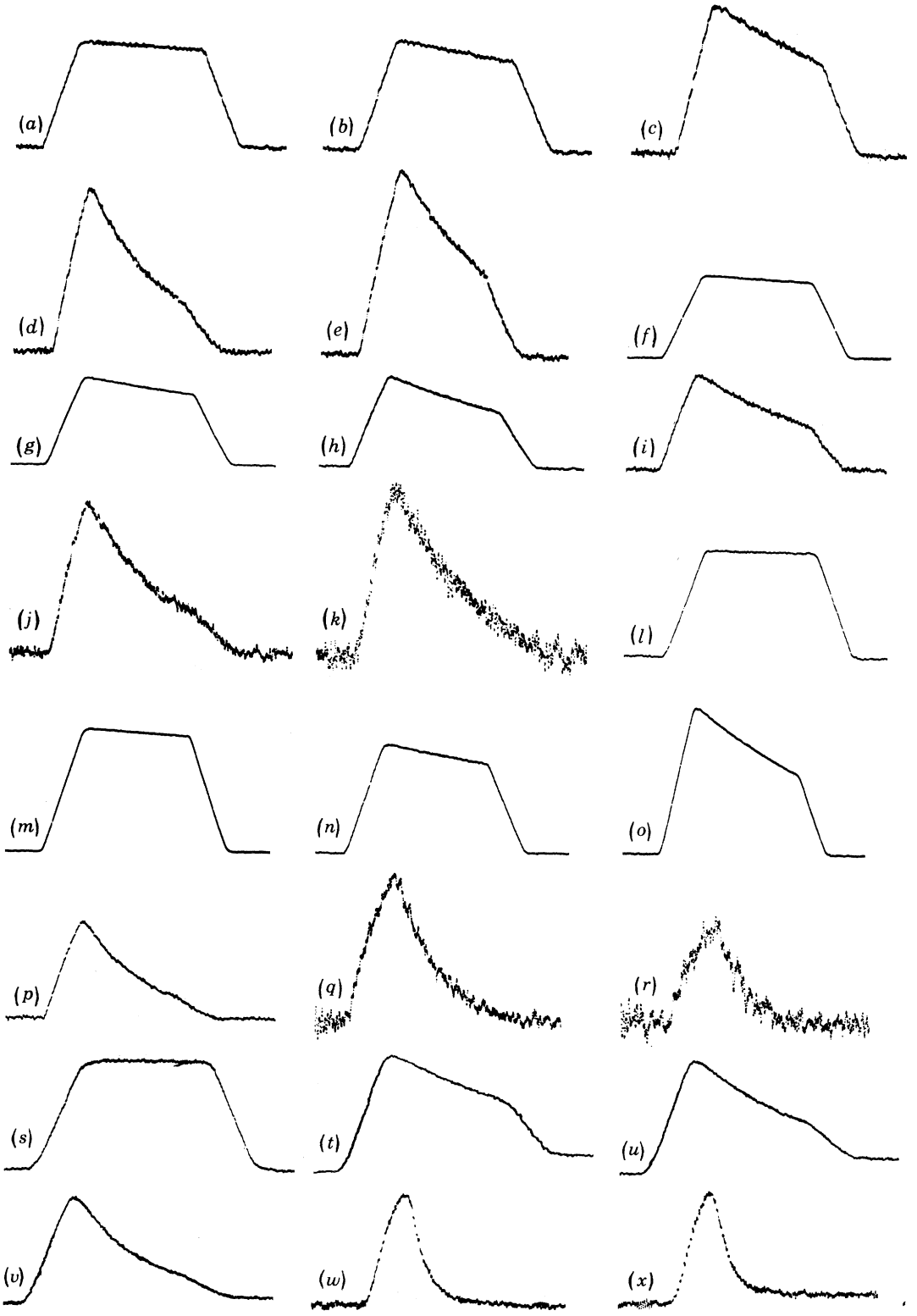

FIGURE 16. Examples of signals recorded under a wide variety of circumstances. The physical conditions and the results of signal analysis in each case are given in table 2.

PHILOSOPHICAL TRANSACTIONS OF THE ROYAL SOCIETY A MATHEMATICAL, PHYSICAL & ENGINEERING SCIENCES

signals, we have concluded that an appropriate mean value to take for ν_0 would be $-50\ \mathrm{s}^{-1}$. This correction is negligible except, of course, when ν is itself small. It is, in any case, usually less than the random experimental error, which may be estimated from the scatter of the data; but we have still felt it to be worth applying because it counters a *systematic* error in the results. Accordingly, before analysing the data, we have added $50\ \mathrm{s}^{-1}$ to all of the unprocessed experimental nucleation rate measurements presented below in §3*b*; and we probably err on the side of caution in estimating a systematic uncertainty of $\pm 50\ \mathrm{s}^{-1}$ in the corrected data.

TABLE 2. DETAILS OF THE SIGNALS SHOWN IN FIGURE 16

signal	P/bar	T/K	E/10^4 V m^{-1}	ν/s^{-1}	$\bar{v}$/m s^{-1}	i_m/nA
(*a*)	21	0.655	5.62	1280	53.01	1.9
(*b*)	21	0.655	11.3	3550	55.27	2.5
(*c*)	21	0.655	24.7	9030	58.47	3.4
(*d*)	21	0.655	67.5	24600	64.46	3.7
(*e*)	21	0.655	112	18300	69.28	4.3
(*f*)	21	0.324	20.2	1550	57.82	7.4
(*g*)	21	0.608	20.2	3990	57.60	8.0
(*h*)	21	0.673	20.2	8530	57.16	4.2
(*i*)	21	0.712	20.2	13500	57.03	2.2
(*j*)	21	0.770	20.2	24400	56.35	0.7
(*k*)	21	0.784	20.2	29500	—	0.4
(*l*)	25	0.297	33.7	219	56.99	3.8
(*m*)	23	0.297	33.7	1090	58.76	9.0
(*n*)	21	0.324	33.7	3660	60.24	9.9
(*o*)	19	0.297	33.7	11200	62.49	5.5
(*p*)	17	0.324	33.7	30300	64.51	2.3
(*q*)	16	0.324	33.7	48700	—	0.8
(*r*)	15	0.324	33.7	85300	—	0.2
(*s*)	25	0.913	20.2	124	48.91	2.0
(*t*)	25	0.913	29.2	(10100)	51.63	2.1
(*u*)	25	0.913	33.7	(17600)	53.03	2.1
(*v*)	25	0.913	39.4	(27300)	53.64	2.0
(*w*)	25	0.913	90.0	10500	—	1.0
(*x*)	25	0.913	112	(132000)	—	0.9

In figure 16 we present a representative selection from our library of signals. The physical conditions under which each of these signals was recorded, and the parameter values arising from its analysis in each case, are given in table 2. From inspection it may be noted that, if other conditions are held constant: (i) ν increases with E (signals (*a*)–(*d*)), but may decrease slightly again (*e*) when E becomes very large; (ii) ν increases with T, as shown in (*f*)–(*k*); ν increases with decreasing P is illustrated by (*l*)–(*r*). At sufficiently high T ((*s*)–(*v*), (*x*)) the signal shape deviates from that expected on the basis of equations (21)–(23) and the technique can no longer be depended upon to provide reliable values of ν. When ν is very large ((*k*), (*q*), (*r*), (*w*)), the right edge of the signal is so attenuated that it becomes impossible to measure $\bar{v}$.

The absolute magnitude of the signal depends on a number of different factors, the most important of which are indicated for typical operating conditions in figure 17. The signal decreases slightly as the electric field in the induction space is reduced (figure 17*a*): this is because the effective transparency of G_3 depends on the ratio of the fields on either side of it. (This effect can, of course, be reduced by reducing the field between G_2 and G_3, but only at the expense of an increased field mismatch across G_2; so that the change would, to some extent, be self-defeating.) The signal decreases rapidly as the temperature is raised above 0.5 K. This

effect is caused by the increased rate of temperature dependent vortex nucleation between the source and G_3 (see below). It arises partly through the loss of bare ions between G_1 and G_3, but more importantly through the decrease in the total emission current from the source itself because of the enhanced space-charge density in the form of charged vorticity (Phillips & McClintock 1975) in the source region. The emission is, of course, a rapid function of the potential applied to the emitters (figure 17*c*). The extent to which the collector signal can be

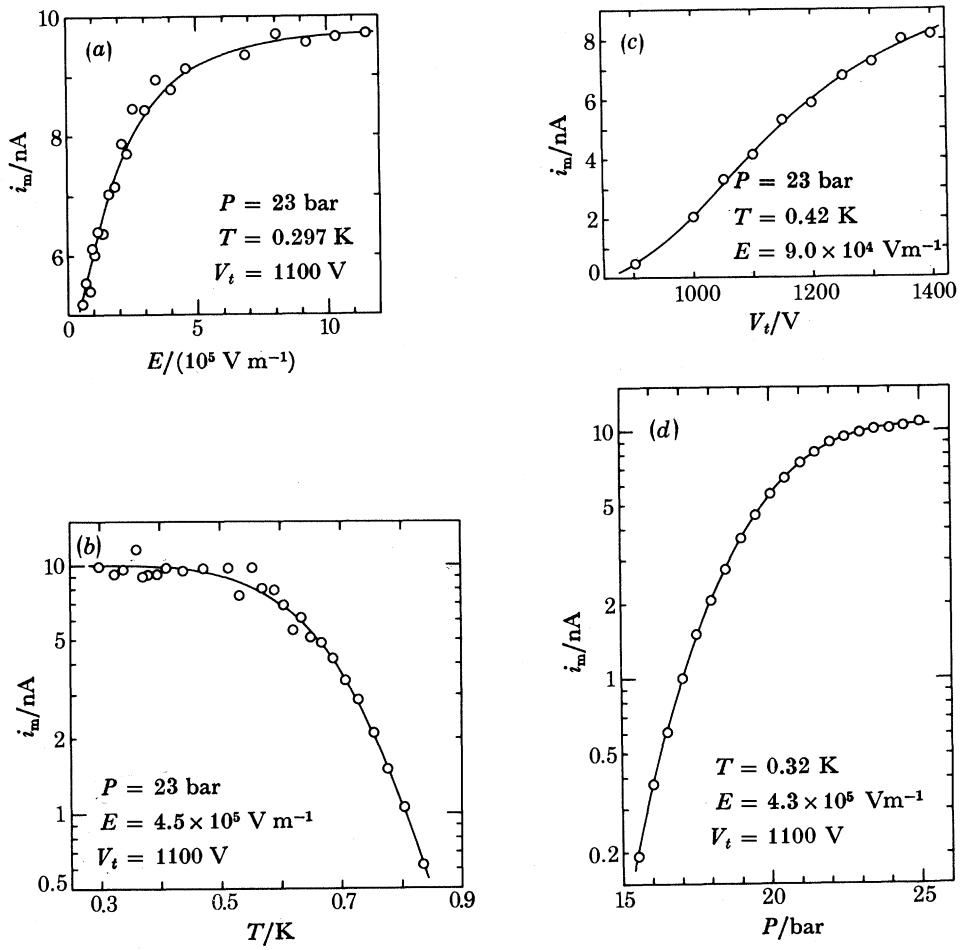

FIGURE 17. Examples of the way in which the maximum induction of the signal i_m (figure 11) varies with (*a*) electric field E, (*b*) temperature T, (*c*) field emission source potential V_t and (*d*) pressure P. The full curves are guides to the eye.

enhanced in practice, simply by increasing the emitter potential, is limited by the possibility of electrical breakdown in the cell, by the increased electric field mismatch across G_1, and by heating of the cell. The collector current decreases rapidly with decreasing pressure (figure 17*d*), owing to the increased rate of vortex nucleation (Phillips & McClintock 1975), which affects the system in much the same way as that due to a rise in temperature.

It was found in practice that achieving a satisfactory signal/noise ratio required unacceptably long averaging periods if i_m fell below 0.5 nA, thus setting an effective limit to the range of physical conditions under which ν could be measured.

(*b*) *Nucleation rate measurements*

Initial testing of the measuring system, using helium of the natural isotopic concentration, yielded values of ν that were highly temperature dependent for $T < 0.5$ K, as shown in figure 18. Also shown is a full curve corresponding to data obtained subsequently (see below) in the same experimental cell and under identical conditions, except in that the natural helium had been replaced by isotopically pure ^{4}He. The change in the magnitude of $\nu(E, T)$ for low E is dramatic, and particularly so given that the effect may well arise from as little as a single ^{3}He atom adsorbed on the ionic surface (McClintock *et al.* 1981). Further studies of this interesting phenomenon, with a range of very dilute ^{3}He–^{4}He solutions, are being planned.

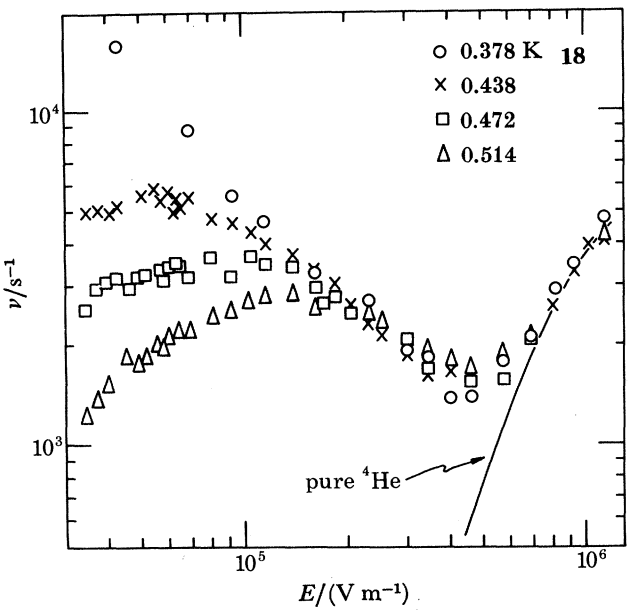

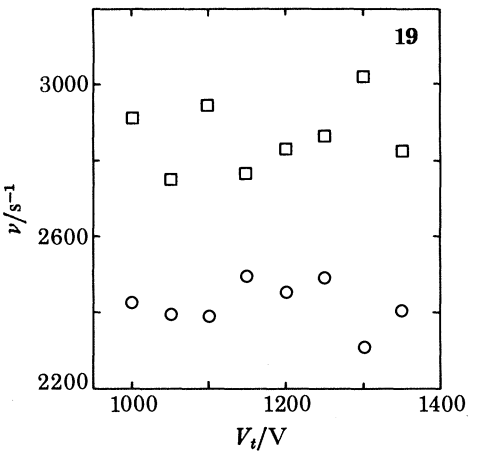

FIGURE 18. The vortex nucleation rate ν measured in liquid helium of the natural isotopic ratio under a pressure of 25 bar, plotted as a function of the electric field E for a number of different temperatures. It may be noted that ν is highly temperature-dependent at low E, but that the data appear to form a universal curve above *ca.* 2×10^5 V m^{-1}. For $E >$ *ca.* 7×10^5 V m^{-1} the data join the full curve representing measurements made in isotopically pure ^{4}He (figure 22*a*).

FIGURE 19. The measured nucleation rate ν plotted as a function of field emission source potential V_t for pure ^{4}He under a pressure of 19 bar and an electric field of 1.35 ± 10^5 V m^{-1}. The squares represent measurements at 0.324 K; and the circles at 0.423 K. Any systematic variation of ν with V_t is smaller than the random experimental error.

With the sole exception of the set of data shown in figure 18, all the nucleation rate measurements reported in the present paper relate to isotopically pure ^{4}He. The possible influence of the source potential on the measured value of ν was carefully investigated but, as shown in figure 19, any such effect is smaller than the scatter in the data. This suggests either that radial inhomogeneities in the charge disc are independent of source potential, or that they are very small; and it suggests that transient heating effects in the cell may be ignored. Another conceivable cause of poor measurements could be the building up of a tangle of charged vorticity in the induction space: the charged rings created during measurement pulses will often grow to macroscopic dimensions and will doubtless become tangled up with one another. The density of such a vortex tangle is quite hard to estimate since, unlike the creation rate, which is

PHILOSOPHICAL TRANSACTIONS OF THE ROYAL SOCIETY A MATHEMATICAL, PHYSICAL & ENGINEERING SCIENCES

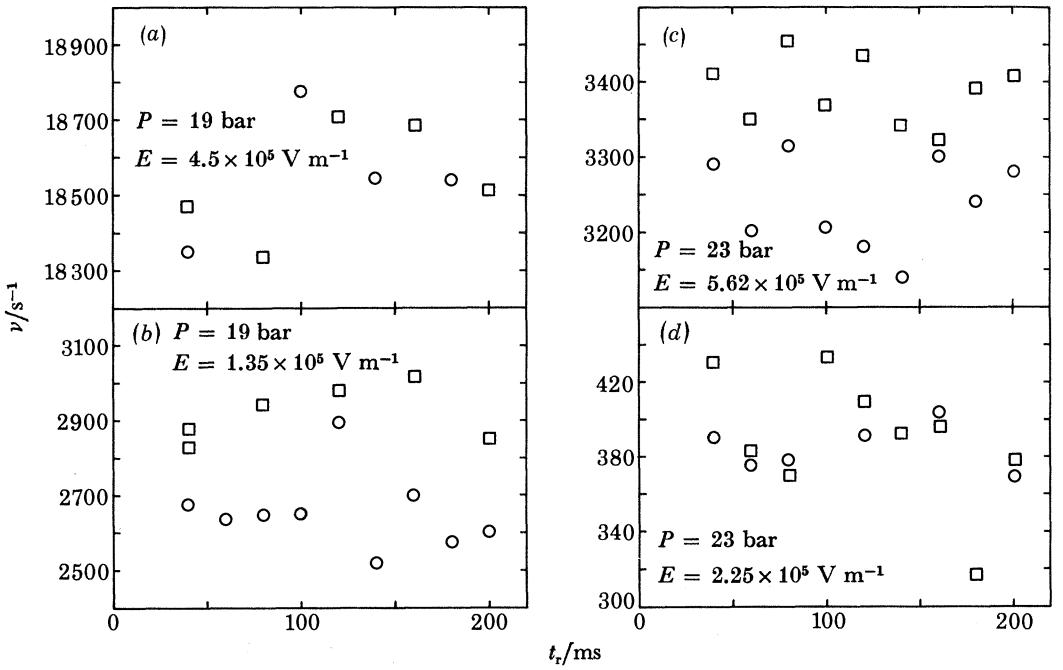

FIGURE 20. Effect of signal repetition rate on measured value of the nucleation rate ν, for relatively high and relatively low values of pressure P, temperature T and electric field E. In each case the measured values of ν are plotted as a function of the elapsed time t_r between signals; the squares and circles are for $T = 0.324$ K and $T = 0.423$ K respectively.

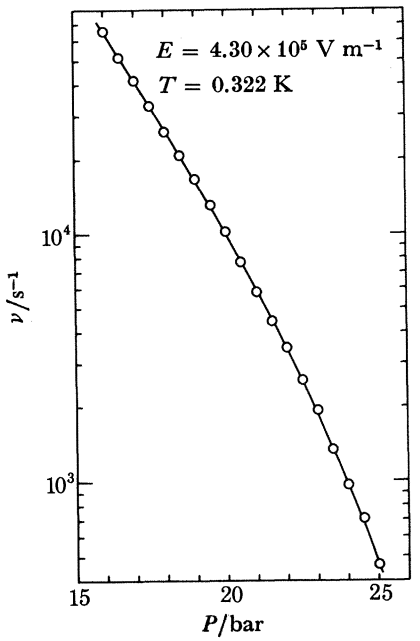

FIGURE 21. Plot of the vortex nucleation rate ν as a function of pressure P, illustrating the sensitivity of ν to small changes in P. The full curve is a guide to the eye.

readily calculable, the annihilation rate under such conditions is unknown. Rather, we have adopted the empirical approach of looking for a possible dependence of ν on the signal repetition rate. Some typical results are plotted in figure 20 where the measured value of ν is plotted for two temperatures, two pressures and two electric fields, against the elapsed time between signals during averaging. It seems clear that the measured value of ν is independent of repetition rate and we conclude, therefore, that, although the subsequent history of the charged vortex rings created during each measurement pulse is unknown in detail, these rings have no measurable effect on the rate at which bare ions are lost from succeeding charge discs.

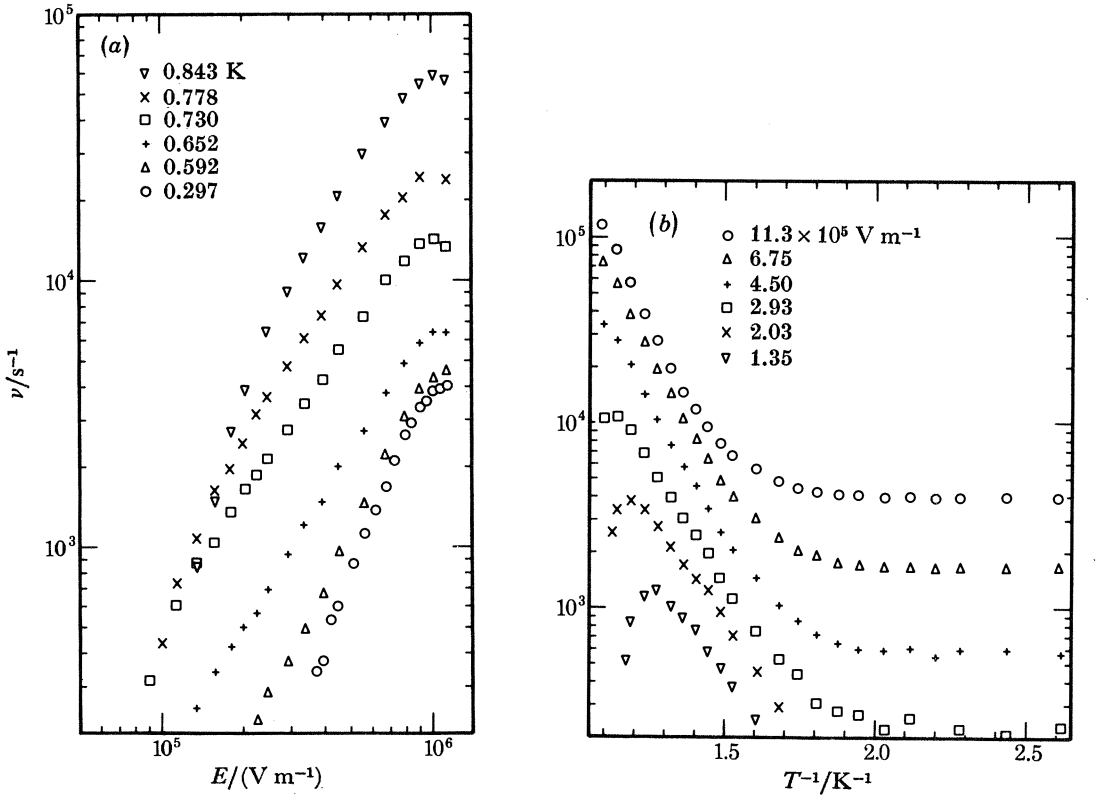

FIGURE 22. Measurements of the vortex nucleation rate ν at 25 bar. In (*a*) ν is plotted as a function of electric field E for a number of different temperatures, and in (*b*) ν is plotted as a function of inverse temperature T^{-1} for a number of different electric fields.

Data are presented below showing the behaviour of $\nu(E, T)$ at a number of fixed pressures. To emphasize the rapid variation of ν with P, however, we have plotted in figure 21 a single scan of $\nu(P)$ for fixed E and T under typical operating conditions. It may be noted that a 1% change in P can produce a corresponding change of 10% or more in ν. The range of P within which measurements can be made by means of our electrostatic induction technique is limited at the bottom end by ν becoming too large, so that i_m becomes too small (figure 17*d*), and at the top end by solidification of the liquid helium at 25.3 bar. The temperature limits are set by the capabilities of the cryostat at the bottom end where, however, ν has become almost temperature independent (see below) and by thermally assisted escape of ions from their rings at the top end (figure 16*t–x*). It should be noted that the technique is restricted to fairly strong electric fields: it is assumed in the analysis that all ions that create rings instantly cease

contributing to the induction in the collector; which will only be true if they grow in diameter very rapidly after being created. It is this requirement, rather than the decrease in i_m for small fields (figure 17*a*), that has caused us to set our minimum field at 5×10^4 V m^{-1}: this ensures that the velocity of a charged ring will have fallen to below 1 % of the bare ion drift velocity within a distance of *ca.* $10^{-2}\,L$ from the point at which it was created.

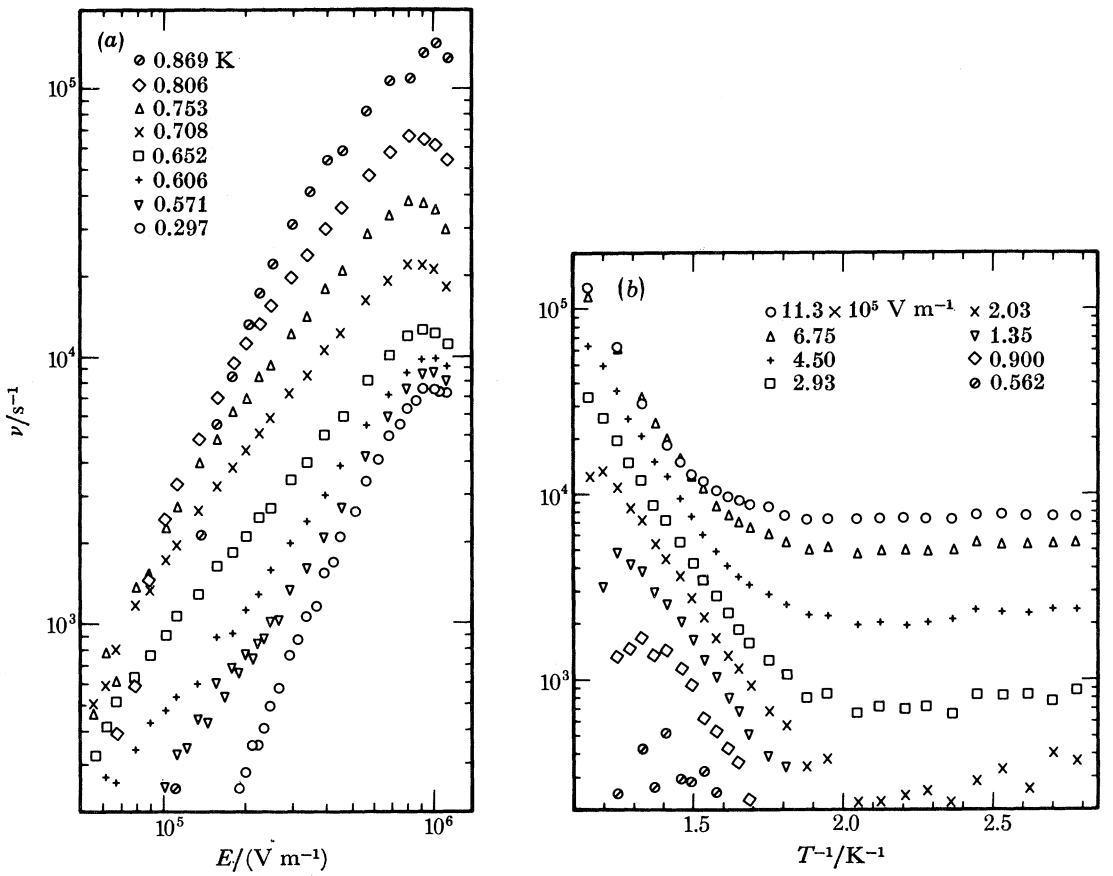

FIGURE 23. Measurements of the vortex nucleation rate ν at 23 bar. In (*a*) ν is plotted as a function of electric field E for a number of different temperatures, and in (*b*) ν is plotted as a function of inverse temperature T^{-1} for a number of different electric fields.

The main body of our experimental results is presented in figures 22–26, each of which refers to a different pressure. In each case: $\nu(E)$ is plotted for several fixed values of T in (*a*); and, in (*b*), $\nu(T^{-1})$ is plotted for several fixed values of E, T^{-1} being used rather than T in order to facilitate comparison with the suggestion (Stamp *et al.* 1979; McClintock *et al.* 1980*a*) that there is a component of ν that is proportional to the thermal roton density. The general form of the characteristics is similar at all pressures at which measurements could be made apart, of course, from the general increase in ν with falling pressure already referred to. At 25 bar, the latter effect limited the lower end of the range of E for which ν could be measured at low T; whereas, at 17 bar, it curtailed the upper end of the temperature range over which $\nu(E, T)$ could be followed. The spreading of the charge disc during its passage across the induction space as defined by the derived value of δ_s (equation (35)) was seldom greater than 3×10^{-3} and was usually considerably less than this.

It may be noted from figures 22*b*, 23*b*, 24*b*, 25*b* and 26*b* that ν is almost independent of temperature below 0.5 K, but increases rapidly at higher temperatures. For low fields at the highest temperatures (figures 22*b*, 23*b*, 24*b*), ν passes through a maximum and then decreases again. At the lower pressures, the signal could not be followed to high enough temperatures to observe this phenomenon. There is some evidence (for example, figure 23*b*) that ν increases again very slightly as the temperature is reduced below 0.5 K. Confirmation of the existence of such an effect may also be seen in figures 19, 20*b* and 20*c*, although it is only slightly outside the scatter of the data.

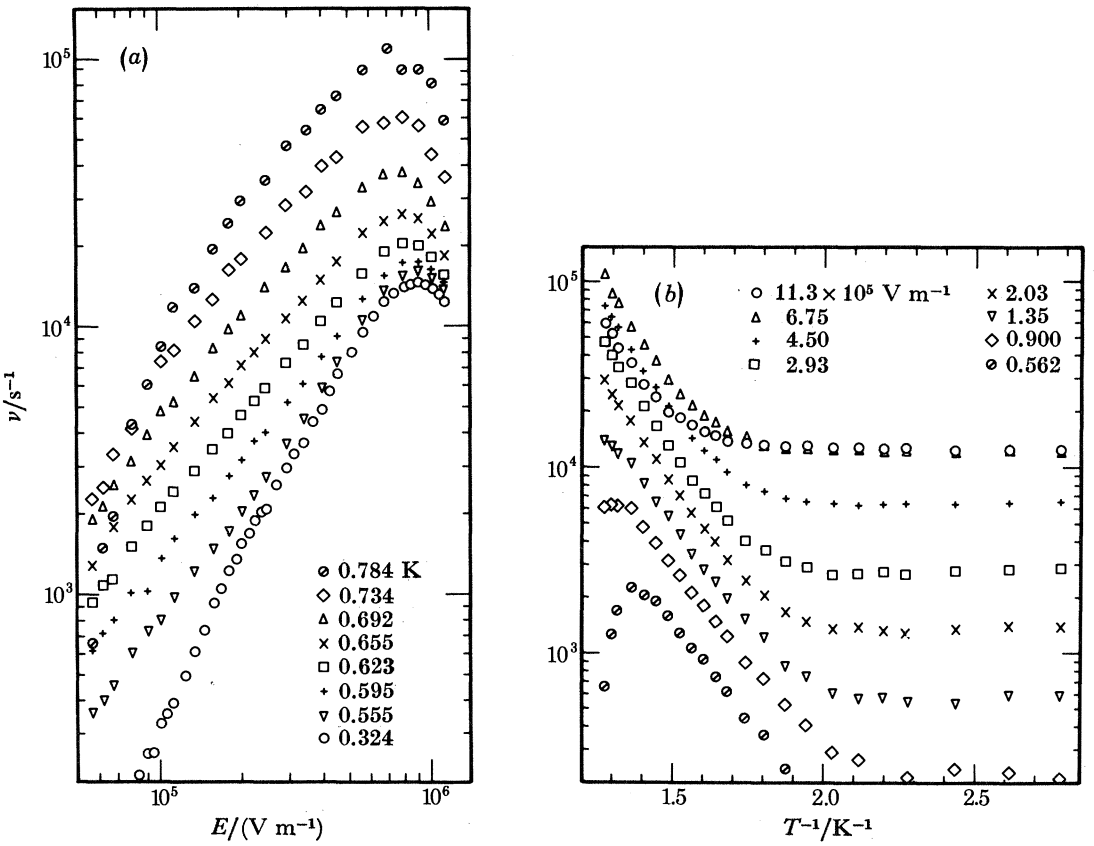

FIGURE 24. Measurements of the vortex nucleation rate ν at 21 bar. In (*a*) ν is plotted as a function of electric field E for a number of different temperatures, and in (*b*) ν is plotted as a function of inverse temperature T^{-1} for a number of different electric fields.

All the $\nu(E)$ curves increase with E for low E, but many of them exhibit a maximum at large E. This maximum is clearly dependent on pressure, being barely attained at 10^6 V m^{-1} for 25 bar (figure 22*a*), but appearing at half this value for 17 bar (figure 26*a*). It is also weakly dependent on temperature, moving to lower values of E as T increases. As shown in figure 25*c*, there was no significant change in the signal shape on either side of the maximum. The two signals were recorded under conditions such that ν is almost the same: the only obvious difference between them is that the one in the larger electric field (figure 25*c*(ii)) is slightly larger, and foreshortened in time, compared to (i), owing to the correspondingly higher ionic drift velocity. At the lower pressures, some structure is seen in $\nu(E)$, with a distinct kink becoming evident in the characteristic, midway between the lowest electric field and that of the

maximum in ν: this phenomenon is most obvious at 17 bar (figure 26*a*) but it also appears to persist, albeit in an attenuated form, up to higher pressures (figures 24*a*, 25*a*). Considerable care was taken to try and eliminate the possibility that the apparent structure might in reality be an artefact arising from, for example, drifts in the parameter settings of the apparatus: all the data that are presented were thus accumulated over a considerable period of time, and

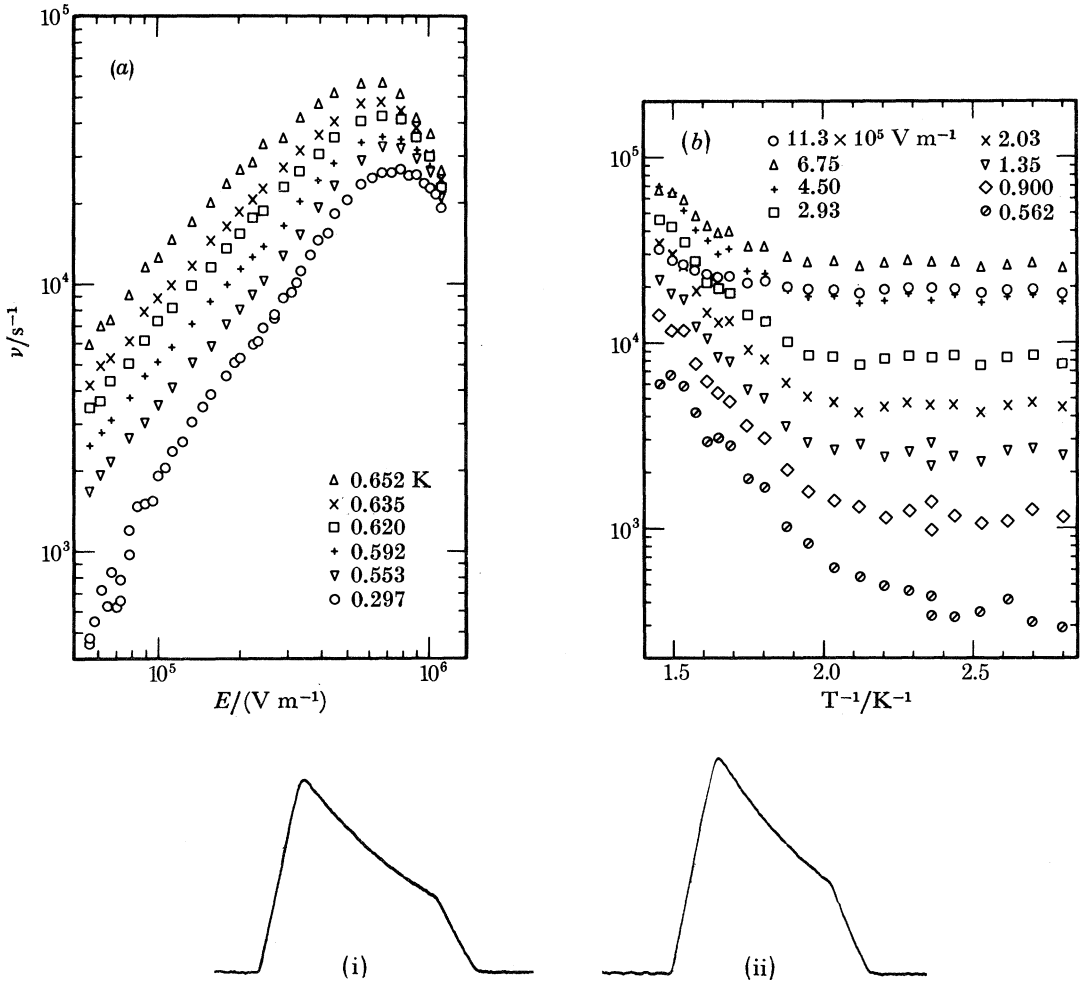

FIGURE 25. Measurements of the vortex nucleation rate ν at 19 bar. In (*a*) ν is plotted as a function of electric field E for a number of different temperatures, and in (*b*) ν is plotted as a function of inverse temperature T^{-1} for a number of different electric fields. The signals shown in (*c*) correspond to almost equal values of ν at 0.297 K, but at very different values of E on either side of the maximum $\nu(E)$: for (i) $E = 4.50 \times 10^5$ V m^{-1}, $\nu = 182100$ s^{-1}; for (ii) $E = 1.12 \times 10^6$ V m^{-1}, $\nu = 19500$ s^{-1}.

the scan of $\nu(E)$ at each temperature represents two, and sometimes four, passes through the E range in opposite directions on different occasions, interlacing the data points, so that any drifts should have shown up as additional scatter. It is therefore hard to avoid the conclusion that the observed structure in $\nu(E)$ is genuine.

It was possible to record a few data at 15 and 16 bar, and these are presented in figure 27. Although the measurements are scattered owing to the very small value of i_m (figure 17*d*), the kink in $\nu(E)$ still seems to be present at midrange electric fields. There is also some evidence for a flattening out of the high field maximum: this appears to be true of both the 15 and the

16 bar characteristics. It must be emphasized, however, that the signals available, particularly those at 15 bar, were extremely weak, so that it would probably be imprudent to try and reach a definite conclusion on this point at the moment.

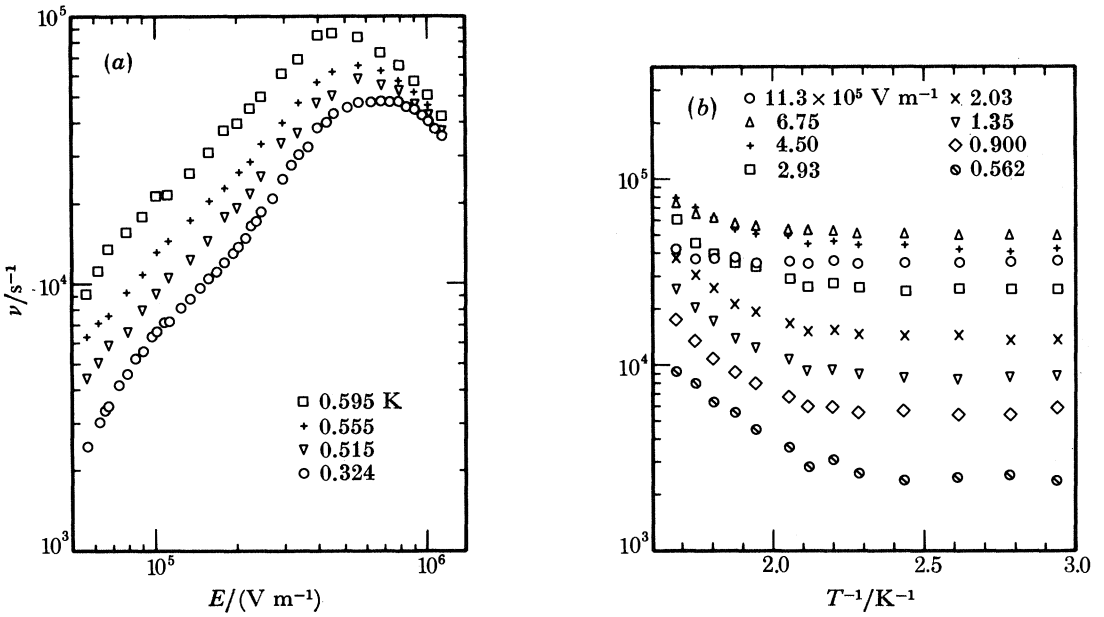

FIGURE 26. Measurements of the vortex nucleation rate ν at 17 bar. In (*a*) ν is plotted as a function of electric field E for a number of different temperatures, and in (*b*) ν is plotted as a function of inverse temperature T^{-1} for a number of different electric fields.

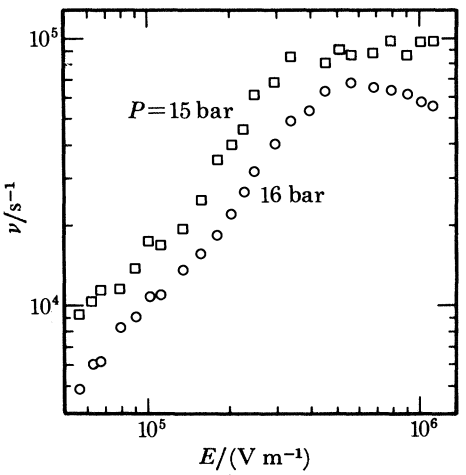

FIGURE 27. Measurements of the vortex nucleation rate ν at the lowest pressures for which useful signals could be recorded, both for 0.324 K, plotted as a function of electric field E.

(*c*) *Velocity measurements*

Although the primary aim of the present research programme was the measurement of vortex nucleation rates, it was straightforward to extract ionic drift velocities from the vortex induction signals by the method described above (§2*d*). There are two reasons why this opportunity was exploited with some vigour. First, as described in more detail below, measurements of $\bar{v}(E, T)$

provide information about the distribution function $f(v, E, T)$ of ionic velocities, and hence are of direct relevance to the interpretation of the vortex nucleation results themselves. Secondly, it was found possible to achieve measurements of $\bar{v}$ that were of greater precision than those reported in I and II. This was partly because of the use of faster electronics which were coupled to a digital data reduction system in place of the analogue system used previously for measuring times of flight. The other factor was improved signal/noise (notwithstanding the adverse electrode geometry, from the point of view of velocity measurements, as compared with those used in I and II) associated with the use of isotopically purified ^{4}He and with the development of a multiple tip field emission source. Purification of the ^{4}He has also enabled the measurements to be extended to a much lower pressure (17 bar) than was possible in I, where data were severely scattered even at 21 bar and could not usefully be recorded below this pressure.

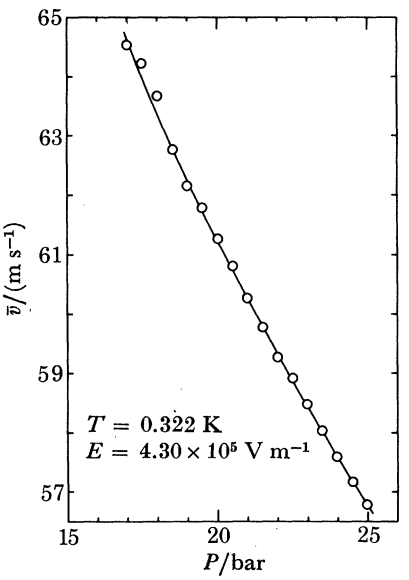

FIGURE 28. Measurements of the ionic drift velocity $\bar{v}$ plotted as a function of pressure P, demonstrating the marked increase of $\bar{v}$ that occurs with decreasing P. The full curve is a guide to the eye.

Most of our velocity measurements are of $\bar{v}(E, T)$ for fixed values of P, but we show in figure 28 a single scan of $\bar{v}(P)$ under typical operating conditions. As discussed in I, the observed dramatic increase of $\bar{v}$ with decreasing P is to be expected because of the corresponding increase in the Landau critical velocity for roton creation, v_L. In figure 29 we plot $\bar{v}(E^{\frac{1}{3}})$ at our lowest temperature, where $\bar{v}$ is effectively temperature independent, for five fixed values of P. The advantage of plotting against $E^{\frac{1}{3}}$, rather than E, is that, as described in I and II, the resultant curves are almost linear. There is a break in the 17 bar results for $70 < E^{\frac{1}{3}} < 95$ (V m^{-1})$^{\frac{1}{3}}$ because, within this range, ν had become so large that the right edges of the signals were too small for adequate velocity measurements.

At higher temperatures, and particularly as T rises above 0.6 K and ion–roton scattering becomes important, the ionic drift velocities deviate slightly from the results of figure 29. These small deviations are of considerable importance because, as discussed in §4, they constitute the sole source of information about the effect of temperature on the velocity distribution function. Velocity measurements made above 0.6 K are presented in figure 30. We have plotted them as $(\bar{v} - v_L)/E^{\frac{1}{3}}$ against $E^{\frac{1}{3}}$ which serves to remove most of the field dependence

and to separate the characteristics recorded at different temperatures (which otherwise would lie almost on top of each other): in this form, the decrease in $\bar{v}$ with increasing temperature is clearly demonstrated. It will be noted that the scatter becomes much more pronounced as the pressure decreases, partly owing to the decrease in i_m, and partly because of the increasing attenuation of the right side of the signals arising from the increasing value of ν. For the same reasons, the range of temperatures over which velocity measurements could be made decreased with decreasing pressure. The data obtained for elevated temperatures at 17 bar were felt not to be worth plotting.

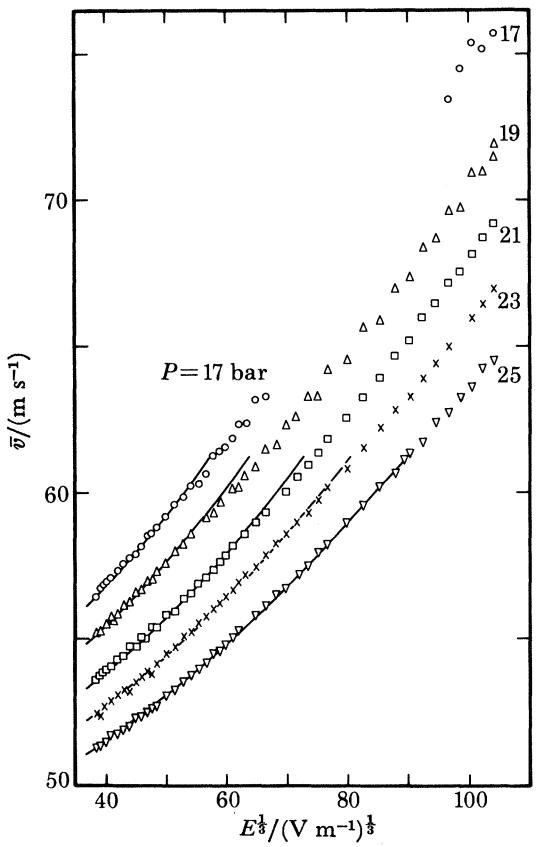

FIGURE 29. Measurements of the ionic drift velocity $\bar{v}$ recorded at *ca.* 0.3 K (where $\bar{v}$ is effectively temperature-independent) for a number of different pressures P and plotted against (electric field E)$^{\frac{1}{3}}$. The full curves are fits of theory to the data, as discussed in §4*a*.

4. DISCUSSION

The way in which the nucleation rate varies with temperature, remaining essentially constant (for given P and E) below 0.5 K, but increasing dramatically for higher temperatures, suggests that the observed value of ν arises as the sum of contributions from two separate mechanisms. We will refer to the low temperature (i.e. temperature independent) part as the spontaneous nucleation process. This can be subtracted from the measured values of ν at high temperatures to obtain the temperature dependent component of the nucleation rate.

The fact that nucleation by the spontaneous process is temperature independent appears to favour the quantum transition model and to preclude the peeling model, if it is assumed

(Schwarz & Jang 1973) that the localized roton states discussed by Donnelly and Roberts (1971) do not occur in reality within the temperature range of interest. On the other hand, the rapid rise in ν with roton density above 0.5 K appears at first sight to favour the peeling model and to exclude the quantum transition model: we will show, however, that this is not necessarily the case.

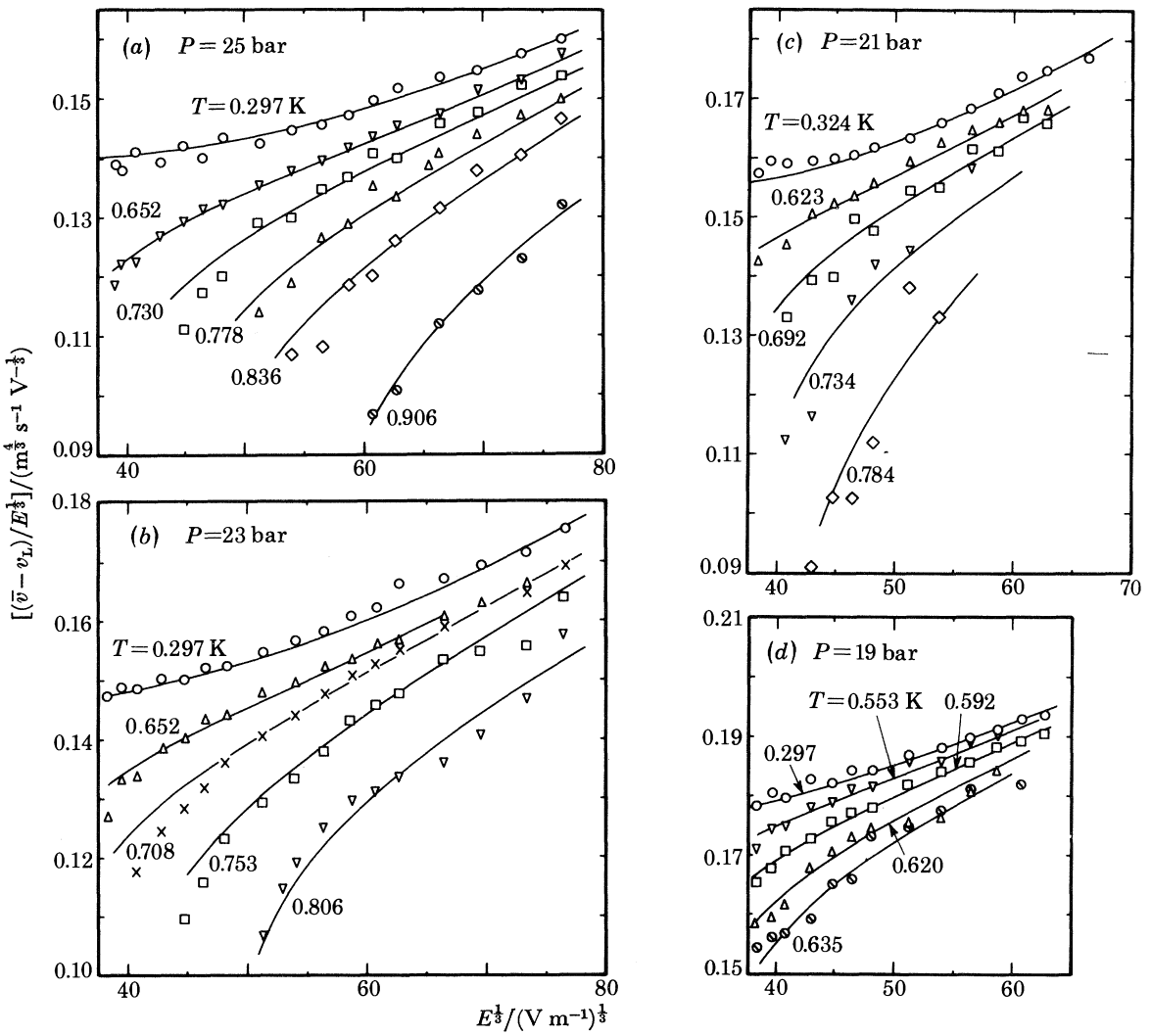

FIGURE 30. Measurements of the ionic drift velocity $\bar{v}$ at a number of different temperatures T and pressures P. For each pressure, the results are plotted as $(\bar{v}-v_L)/E^{\frac{1}{3}}$ against $E^{\frac{1}{3}}$ to separate the data at different temperatures. The full curves are fits of theory to the data as discussed in §4*b*.

Let us suppose that the instantaneous rate of vortex nucleation R is independent of E, and depends only on velocity and temperature for any given pressure (assumed constant in the discussion that follows). The measured rate of nucleation is then given by

$$\nu(E, T) = \int_0^\infty \mathrm{d}v\, f(v, E, T)\, R(v, T), \tag{37}$$

where f is the distribution function of ionic velocities in the direction of E.

For each temperature the drift velocity, $\bar{v}$, is a unique function of E. Thus equation (37) can be written as

$$\nu(\bar{v}, T) = \int_0^\infty \mathrm{d}v\, f(v, \bar{v}, T)\, R(v, T), \tag{38}$$

where

$$\bar{v} = \int_0^\infty v\, f(v, E, T)\, \mathrm{d}v. \tag{39}$$

We now assume that $f(v, \bar{v}, T)$ is independent of temperature, apart from the temperature dependence of $\bar{v}$. This is equivalent to an assumption that processes involving the scattering of excitations do not alter the shape of the distribution function, but only the mean value $\bar{v}$. (If we had chosen to work with $\nu(E, T)$, rather than $\nu(\bar{v}, T)$, we would have had to worry about the change in the mean of the distribution function with temperature.)

If we now propose formally that R can be written as

$$R(v, T) = R_\mathrm{s}(v) + n_\mathrm{r} R_\mathrm{r}(v), \tag{40}$$

where n_r is the number density of rotons and R_s and R_r are two functions of v, then

$$\nu(\bar{v}, T) = \int_0^\infty \mathrm{d}v\, f(v, \bar{v})\, R_\mathrm{s}(v) + n_\mathrm{r} \int_0^\infty \mathrm{d}v\, f(v, \bar{v})\, R_\mathrm{r}(v)$$

or

$$\nu(\bar{v}, T) = \nu_\mathrm{s}(\bar{v}) + n_\mathrm{r} \nu_\mathrm{r}(\bar{v}). \tag{41}$$

This will lead to a nucleation rate that is constant for low temperatures but which increases rapidly above about 0.5 K as the roton number density increases, in accord with the experimental results.

How defensible are the assumptions that we have made? The first supposition was that scattering processes do not alter the overall shape of $f(v, \bar{v})$. The distribution function for high fields is nearly gaussian (Bowley & Sheard 1977). Scattering processes will tend to broaden the distribution function further, but the broadening will be insignificant if the scattering processes occur at a rate that is smaller than the rate of roton emission. A measure of these scattering rates can be obtained by comparing the shift in drift velocity with temperature, $\bar{v}(E, T) - \bar{v}(E, 0)$, to the difference between the drift velocity and the Landau velocity, $v(E, 0) - v_\mathrm{L}$. For the temperatures that we have used, we can ignore the broadening for drift velocities greater than 52 m s^{-1}. Even if broadening occurred, it would not be a serious problem if $R(v)$ were a smooth function of velocity; it would, however, cause errors if there were a critical velocity above which $R(v)$ increased very rapidly.

The second hypothesis (equation (40)) can be tested by seeing whether the temperature dependent component of the nucleation rate scales with the number density n_r of thermal rotons, which is given by

$$n_\mathrm{r} = (k_0^2/2\pi^2\hbar)\, (2\pi\mu_\mathrm{r} k_\mathrm{B} T)^{\frac{1}{2}}\, \mathrm{e}^{-\Delta/k_\mathrm{B} T},$$

where k_0, μ_r and Δ are roton parameters (Wilks 1967; Brooks & Donnelly 1977). Accordingly, we must plot $[\nu(\bar{v}, T) - \nu_\mathrm{s}(\bar{v})]/[T^{\frac{1}{2}} \mathrm{e}^{-\Delta/k_\mathrm{B} T}]$ against $\bar{v}$ to see whether data recorded at different temperatures will fall on a common curve. We will show that this is indeed the case, thus confirming the assumptions inherent in (40).

To proceed with the analysis we require accurate values of ν and $\bar{v}$ at corresponding temperatures, pressures and electric fields. The velocity measurements confer other benefits: we will be able to fit the drift velocity curves $\bar{v}(E)$ to the model of Bowley & Sheard (1977),

thereby generating theoretical values of $f(v, \bar{v})$ which can then be used to test simple models for $R(v)$ in an attempt to account for the measured nucleation rates. One difficulty, which we discuss in more detail below, arises from the fact that the roton parameters under pressure are not known nearly as accurately as those under the saturated vapour pressure, mainly because inelastic neutron scattering data in the relevant region of the helium phase diagram are sparse (Donnelly & Roberts 1977). In the analysis that follows we have taken the values given by Brooks & Donnelly (1977), linearly interpolating for pressures that are not included in their tables. The actual values that we have used are tabulated in table 3.

TABLE 3. ROTON PARAMETERS USED IN DATA ANALYSIS, AND THEORETICAL VALUES OF THE LANDAU CRITICAL VELOCITY

P/bar	15.000	17.000	19.000	21.000	23.000	25.000
Δ/K	7.7323	7.6281	7.5245	7.4209	7.3164	7.2102
μ/m_4	0.14186	0.13985	0.13786	1.13587	0.13387	0.13185
k_0/nm^{-1}	1.9926	2.0000	2.0070	2.0136	2.0200	2.0261
v_L (m s^{-1})	50.237	49.395	48.572	47.764	46.958	46.153

In §4*a* we analyse drift velocity measurements made at the lowest temperatures, where excitation scattering may be neglected within our range of E; and in §4*b* we discuss the situation at higher temperatures, where the drag arising from scattering becomes comparable with that due to roton emission. The spontaneous and temperature dependent vortex nucleation processes are discussed respectively in §4*c*, *d*.

(*a*) *Ionic drift velocities at very low temperatures*

In the model of Bowley & Sheard (1977) it is assumed that the ion emits rotons in pairs, and that the matrix element for this process is constant for any given pressure. The dispersion curve for rotons is taken as

$$E(k) = \Delta + \hbar^2(k-k_0)^2/2\mu. \tag{42}$$

The only other parameter in the model is the effective mass m^* of the ion. This can be estimated from the formula

$$m^* = \tfrac{2}{3}\pi\rho R^3 + m_e, \tag{43}$$

where R is the (pressure dependent) radius of the ion (Ostermeier 1973). An important quantity in the theory is the velocity decrement of the ion (see I) during roton creation $\Delta v = \hbar k_0/m^*$, which, on the basis of (43), will vary with pressure as shown in figure 31.

We can fit the model to the data, using the matrix element as a single adjustable parameter: it is found that at low fields

$$\bar{v} = v_L + AE^{\frac{1}{3}}, \tag{44}$$

where A is a constant and

$$v_L = \min\,(E(k)/\hbar k).$$

At higher fields $\bar{v}(E)$ departs from the simple form given by (44) but is still readily calculable (Allum *et al.* 1977) without the need to introduce any additional adjustable parameters. Using (42) for $E(k)$, we find

$$v_L = \{[2\Delta\mu + (\hbar^2k_0^2)]^{\frac{1}{2}} - \hbar k_0\}/\mu. \tag{45}$$

In practice, we have found it useful to fit theory to the data at each pressure using both v_L and A (in effect, the matrix element) as adjustable parameters. As described above, a small

modification is made to the assumed length of the cell so that agreement with (45) is obtained at 25 bar, using the roton parameters of Brooks & Donnelly (table 3). The intercepts obtained at other pressures then yield a measure of the pressure dependence of v_L, as shown in figure 32. The full curve shows the pressure variation predicted by equation (45). It may be noted that all the measured v_L values agree with the predicted behaviour to better than 1 %, but that they tend to fall slightly above the theoretical curve at the lower pressures. Similar trends have also been observed (Ellis *et al.* 1980*b*) in measurements of higher precision done by a different technique under very much weaker electric fields in the millikelvin temperature range.

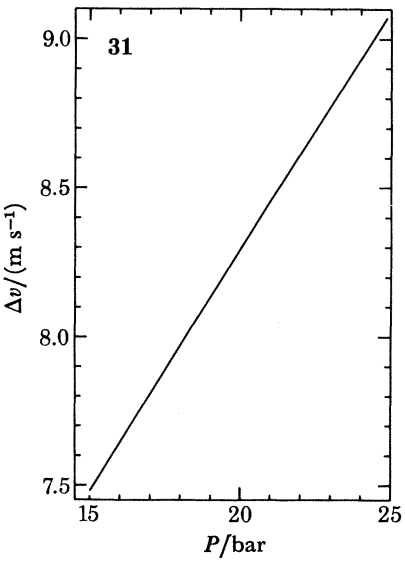

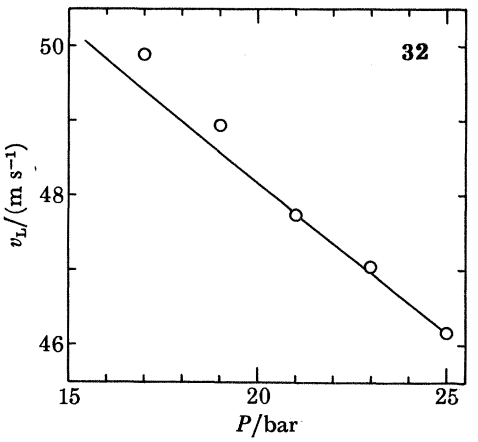

FIGURE 31. The velocity decrement Δv of the ion during roton pair emission, calculated from (43) with use of the ionic radii given by Ostermeier (1973) and plotted as a function of pressure P.

FIGURE 32. Variation of the Landau critical velocity v_L with pressure P. The points were obtained by fitting theory to the data of figure 29. The full curve is the calculated form of $v_L(P)$ by using equation (45) and the roton parameters listed in table 3.

The $\bar{v}(E^{\frac{1}{3}})$ theoretical curves shown in figure 29 were constructed on a slightly different basis, however, to ensure consistency between deduced matrix elements, values of v_L, and the roton parameters (table 3) used below in analysing the vortex nucleation data. The assumed length of the cell was fixed, as before, by fitting the theory to the 25 bar data and adjusting L slightly so as to ensure an intercept exactly equal to the theoretical value of v_L (table 3). Once this had been done, theoretical curves for the other pressures were fitted to the data by using the values of v_L predicted by (45) and by treating the matrix element as the only adjustable parameter. Agreement between experiment and theory (figure 29) is quite good except at high velocities where the data fall below the theoretical curves. As discussed in II, such discrepancies are believed to be caused by:

(i) departures of the density of states from the value deducible from (42), for excitations far from the roton minimum;

(ii) the variation with wavevector of the pole strength of the excitation; and

(iii) the increase with E of the average momentum of the rotons that are emitted.

It may be noted that the onset of the discrepancies occurs at lower values of $(\bar{v}-v_L)$ as the pressure is reduced. A possible explanation is that (i), and therefore also (iii), become more

serious at lower pressures because of the greater asymmetry of the roton minimum; but further work, including low field velocity measurements in an apparatus designed specifically for measuring velocities, is clearly required.

In view of these small discrepancies, we will find it advantageous to plot vortex nucleation rates as a function of drift velocity. Thus, when we come to make comparisons between the data and curves predicted from theoretical values of $f(v, \bar{v})$, little error will arise whereas, if we plotted $\nu(E)$, we would make substantial errors for velocities greater than about 62 m s^{-1}.

Derived values of the matrix element are given in table 4. These values differ slightly from those found previously (McClintock *et al.* 1980*b*), partly because we are fitting to different data for the velocity and partly because we are using a different set of roton parameters. We estimate these matrix elements to be accurate to about 2 %, this error arising entirely from the uncertainty in the slope in the fit to the data.

TABLE 4. VALUES OF THE MATRIX ELEMENT FOR ROTON PAIR EMISSION

P/bar	17	19	21	23	25
$\mathscr{H}/(10^{-52}\,\mathrm{J\,m^3})$	2.59	2.80	3.09	3.34	3.64

The matrix element decreases as the pressure decreases, but the physical mechanisms underlying this phenomenon are far from obvious. The radius of the ion increases with decrease in the pressure, so that one might speculate that the matrix element varies as some inverse power of the radius. Further analysis will require a specific model for the emission process.

(*b*) *Ionic drift velocities at higher temperatures*

The drift velocity of the ion falls as the temperature increases owing to the scattering of excitations, both phonons and rotons. If we want to calculate the drift velocity then, properly, we should recalculate the distribution function $f(v)$ from the Boltzmann equation with the scattering processes included. This is a daunting task; so we have preferred to adopt a more simple-minded approach, which is sufficient for our present purposes.

The rate of momentum loss by the ion through roton emission and through scattering processes is equal to the force on the ion due to the electric field. The rate of scattering by excitations will increase as the velocity of the ion increases. We propose that the drag force on the ion arising from scattering processes may be written as $k(T)\,\bar{v}$, where $k(T)$ is some constant to be determined. The net force on the ion which balances the rate of loss of momentum through roton emission is

$$E' = E - k(T)\,\bar{v}. \tag{46}$$

The scattering processes will reduce the mean velocity of the ion. We can estimate the reduction in drift velocity due to scattering by calculating $f(v, E')$ and then $\bar{v}(E')$. The constant $k(T)$ is needed, but this can be determined from the experimental results at any given temperature by measuring the extent to which $\bar{v}(E)$ departs from the values found at low temperatures, where there is very little scattering.

The full curves of figure 30 were generated on the basis of equation (46), with use of $k(T)$ as an adjustable parameter. Within the scatter of the data the fit is quite good, particularly given that the precision of the velocity measurements decreases as the temperature is raised (see §3*c*). In figure 33 we show the values of $k(T)$ derived by fitting the data in this way, with $\ln k(T)$ plotted as a function of T^{-1}. The almost linear variation with T^{-1} suggests that

roton scattering is important although allowance must, of course, also be made for phonon scattering. We assume, therefore, that $k(T)$ is of the form

$$k(T) = \hbar k_0 n_r \sigma_r + \hbar k_T n_{ph} \sigma_{ph}, \tag{47}$$

where n and σ are respectively the number density and scattering cross sections of either rotons or phonons, as indicated by the subscripts, and $\hbar k_T$ is a typical thermal phonon momentum. We have fitted (47) to the experimental $k(T)$ results for 21, 23 and 25 bar (the 19 bar data cover too small a range of T^{-1} to be useful) by treating σ_r and σ_{ph} as adjustable parameters,

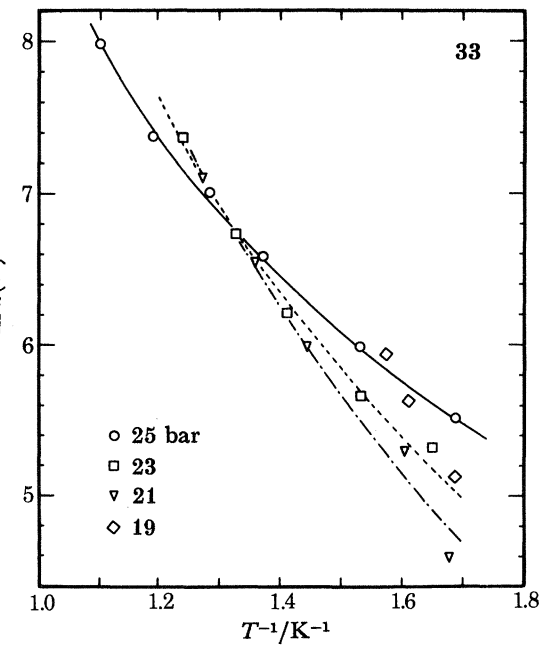

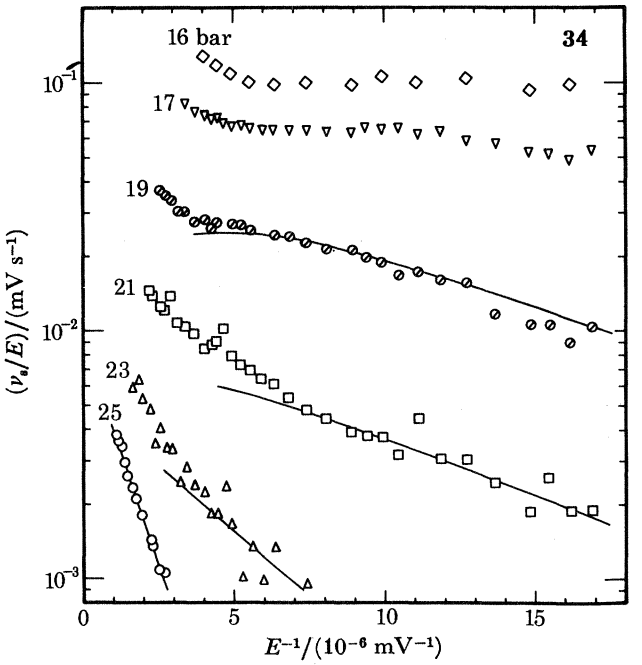

FIGURE 33. Temperature dependence of the quantity k defined by equation (46), plotted as $\ln k$ against (temperature, $T)^{-1}$, for four different pressures. The points were obtained by fitting theory to the $\bar{v}(E, T)$ data plotted in figure 30, and the curves represent fits of equation (47) to the $k(T)$ points: full curve, 25 bar; dashed curve, 23 bar; dot–dashed curve, 21 bar.

FIGURE 34. Low-temperature nucleation rates ν_s at various pressures plotted as $\ln(\nu_s/E)$ against E^{-1} for relatively weak electric fields E, for comparison with equation (49). The data are those of figures 22–27 and the full curves are fits of the theory.

TABLE 5. ROTON EFFECTIVE SCATTERING CROSS SECTIONS σ_r COMPARED WITH THE GEOMETRICAL CROSS-SECTION OF THE ION σ_g

P/bar	21	23	25
σ_r/nm²	19.9	17.3	16.9
σ_g/nm²	4.2	4.0	3.9

yielding the curves shown in figure 33. The roton cross sections obtained in this way are shown in table 5. (The phonon cross sections are not considered reliable.) It may be noted that the values of σ_r are considerably larger than the geometrical cross section, σ_g of the ion. For an ion travelling at 50–60 m s^{-1} there will, however, be a large associated backflow field. It is quite conceivable that rotons are scattering from the backflow around the ion as well as from the surface of the bubble itself. We must emphasize once again that, to obtain accurate roton

and phonon cross sections, it would be necessary to undertake a full theoretical treatment involving solution of the Boltzmann equation with scattering processes included.

We conclude, however, that the temperature dependence of the drift velocity (figure 30) can readily be understood in terms of excitation scattering. We note that roton scattering will occur at a rate of *ca.* $k(T)/\hbar k_0$: provided that this rate is small compared to the roton emission frequency, as has been the case in practice, scattering will have little effect on the shape of the velocity distribution function.

(*c*) *Vortex nucleation at very low temperatures*

At low fields the distribution function is known analytically (Bowley & Sheard 1977) and so it is possible to obtain analytic expressions for $\nu_s(E)$ for various forms of $R_s(v)$. For example, if

$$R_s(v) = R_s\theta(v - v_v), \tag{48}$$

then (Bowley 1976)

$$\nu_s(E) \approx \frac{R_s eE}{2\hbar k_0 \alpha'(v_v - v')^2} \exp\left(-\frac{m^*\alpha'(v_v - v')^2}{3eE}\right), \tag{49}$$

where $v' = v_L + \Delta v$ is the minimum instantaneous velocity at which roton pair emission can occur (see I) and α' is the rate constant (Bowley & Sheard 1977). This suggests that we plot $\ln[\nu_s(E)/E]$ against E^{-1}: the slope of the linear portion should then give $v_v - v'$.

In figure 34 we plot the low electric field data for different pressures in this way. At 25 bar the data appear to be linear, but the systematic error is relatively large because ν is small. At 19 and 21 bar it can be seen that there is a linear region for $E^{-1} > 7 \times 10^{-6}$ m V^{-1}. For smaller values of E^{-1} there is an increase in the slope of the curve which suggests that a new mechanism is coming in above a higher critical velocity. Eventually, of course, for very high fields, the nucleation rate drops dramatically (figures 23*a*, 24*a*, 25*a*, 26*a*).

We can fit the linear part of each curve to (49) and hence obtain an estimate of v_v. The fits to the data at low fields are shown by the full curves of figure 34. The data and fits at intermediate pressures are probably the most reliable, because the absolute value of ν is then much larger than the possible systematic error of ± 50 s^{-1}, but the signal is still large enough for the scatter in the results to be relatively small. For low pressures (15 to 17 bar) the values of $(v_v - v')$ obtained are small and the approximations leading to equation (49) break down.

To account for the detailed shape of $\nu(E)$ at higher fields, we have suggested (McClintock *et al.* 1980*b*) that a new mechanism may come in above a second critical velocity. This can be allowed for by including a second term of the form $R_2\theta(v - v_{v_2})$ and adding the two together. However, a better fit is obtained if we suppose, in addition, that the rate falls abruptly to zero above a third critical velocity, i.e.

$$\left.\begin{aligned} R &= 0 \\ R &= R_1 \\ R &= R_1 + R_2 \end{aligned}\right\} \begin{aligned} &v < v_{v_1} \quad \text{or} \quad v > v_{v_3} \\ &v_{v_2} > v > v_{v_1} \\ &v_{v_3} > v > v_{v_2}, \end{aligned} \tag{50}$$

as sketched in the inset of figure 35. This gives us five parameters to adjust and ensures a fairly good fit after a certain amount of trial and error. Furthermore, we can construct theoretical curves from tables of values of the quantities

$$F(x) = \int_x^\infty f(v, \bar{v})\,\mathrm{d}v \tag{51}$$

in a simple manner, so that this is a convenient form of $R(v)$ to use in practice.

In figure 35 we show the $\nu_s(E)$ measurements at 19 and 23 bar, replotted as a function of $\bar{v}$. It can be seen that we are able to obtain a good fit for lower velocities by using (50), but that we cannot reproduce the rapid decrease in ν found at large fields. This decrease is more pronounced on the plot of $\nu(\bar{v})$ as opposed to that of $\nu(E)$, and the discrepancy between theory and experiment is more obvious: the reason is the disparity between theoretical and experimental $\bar{v}(E)$ for high fields (figure 29).

We have already analysed data at 17, 21 and 25 bar in this way (McClintock *et al.* 1980*b*) but we have re-analysed them using the Brooks & Donnelly (1977) roton parameters. The values of R_1, R_2, v_{v_1}, v_{v_2}, and v_{v_3} found in this way are given in table 6. It can be seen that

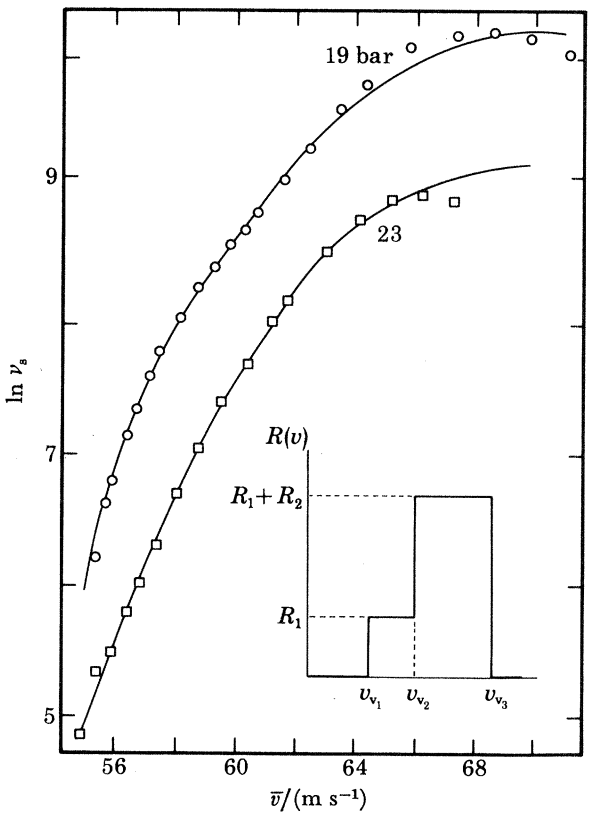

FIGURE 35. Equation (5) fitted (full curves) to low temperature nucleation rates ν_s (points) measured at 19 and 23 bar. The drift velocity $\bar{v}$ is used as abscissa to reduce problems arising from the small deviations (figure 30) that exist between experimental and theoretical values of $\bar{v}(E)$. The fits are satisfactory, except in the region of the maximum in $\nu(\bar{v})$, where the data fall much more rapidly with increasing $\bar{v}$ than the theoretical curves. Inset: sketch showing form of $R(v)$ corresponding to equation (50).

TABLE 6. NUMERICAL VALUES OF PARAMETERS USED IN FITTING EQUATION (50) TO LOW TEMPERATURE VORTEX NUCLEATION $\nu_s(E)$ DATA

P/bar	17	19	21	23	25
$R_1/(10^3\ \mathrm{s}^{-1})$	23	12.3	4.7	2.6	1.8
$R_2/(10^3\ \mathrm{s}^{-1})$	195	146	150	95	56
v_{v_1}/(m s^{-1})	59.8	59.3	59.8	60.7	60.6
v_{v_2}/(m s^{-1})	69.8	69.1	69.8	69.9	70.1
v_{v_3}/(m s^{-1})	72	71.4	71.3	71.7	71.7
v_v^{83}/(m s^{-1})	52.8	53.3	54.0	54.3	54.9

v_{v_1} lies close to 60 m s^{-1} but that it increases slightly with pressure. This compares quite favourably with the estimates of the first critical velocity by Schwarz & Jang (1973), which are also listed, as v_v^{SJ}, in table 6.

It should, however, be noted that the latter authors emphasize very strongly that their values of v_v^{SJ} should be regarded as suggestive rather than quantitative. There are two main reasons for this. First, the values derive from a model calculation based on an initial ring configuration which may not necessarily correspond to reality. Secondly, the magnitude of v_v^{SJ} is strongly influenced (to the extent of $\pm$ *ca.* 10 m s^{-1}) by the value chosen for the vortex core parameter, which itself is poorly known. It should also be noted that the model takes no account of the stability or otherwise of the ion ring complex after its formation. In general, the ion and initial ring may be expected to move at different velocities immediately following the nucleation event and it cannot, therefore, be assumed that the ion will invariably be captured by a ring that it has created (see also below). There are two matters of general principle that should also be commented upon. First, the calculations depend upon the use of hydrodynamic arguments in a régime where their application must at least be open to question. Secondly, the model rests on the premise that local impulse must be conserved. The latter condition seems not implausible, however, given the low density of thermal excitations and the relative isolation of the ion and ring far from the chamber walls. Furthermore, the results of I may be considered to provide an unambiguous experimental demonstration that local impulse is indeed conserved in the analogous case of roton creation by the ion (since, otherwise, extrapolation of $\bar{v}(E)$ to $E = 0$ would not yield $\bar{v}(0) = v_L$).

We would emphasize that, in fitting the low field data, there is no theoretical justification for using the particular form of $R(v)$ given by equation (48). If, instead, we took $R(v)$ to increase linearly as

$$R(v) = B(v - v_v)\,\theta(v - v_v),$$

then, *a priori*, this would be no less plausible. One would then find that ln (ν/E^2) varied linearly with E^{-1} for small fields. This behaviour would also be consistent with the low field data, and it would lead to a critical velocity of about 54 m s^{-1} at all pressures, in excellent agreement with the calculation of Schwarz & Jang. Moreover, one can imagine that there may exist a variety of functions $R(v)$ that are consistent with the data over the full range of fields. All of them will, however, share the feature that $R(v)$ at first increases with v and then decreases very rapidly above about 70 m s^{-1}.

The main merit of using equation (48) (or equation (50)) is that it enables us to make quantitative comparisons of data at different pressures, so as to estimate the pressure dependence of v_v. Similarly, we can compare values of v_v for the spontaneous and the roton assisted processes and find the effect on these values caused by the energy of the roton (see §4*d*, below).

Eventually, it may be possible to test unambiguously between different explicit forms of $R(v)$. This will only be feasible when there is an order of magnitude improvement in the accuracy of the experimental measurements of ν.

It is interesting to speculate on the physical mechanisms underlying the unexpected decrease of ν with E at very large E. We note that the same phenomenon also occurs for the temperature dependent nucleation process (see §4*d*) but that the maximum in $\nu(E)$ has moved to a slightly lower value of E for any given pressure. We can conceive of three possible explanations:

(i) The rate of production of vortex rings $R(v)$ decreases for velocities above 70 m s^{-1}. We proceeded on the basis of this assumption in trying to fit the data using equation (50).

(ii) The ion escapes from the vortex ring that it has created. The apparent decrease in $\nu(\bar{v})$ for large $\bar{v}$ is then caused by the decrease in the number of trapped ions for large velocities $\bar{v}$.

(iii) The ion evades capture by the vortex ring when it is created, this evasion process being more likely to occur at high fields. Only ions that are trapped on vortex rings travel slowly and do not contribute to the signal.

Of the three possibilities listed the least probable is (ii). The escape probability is expected to be negligible for the temperatures and electric fields in question (Donnelly & Roberts 1969). Furthermore, there is no marked temperature dependence of the position of the maximum in $\nu(\bar{v})$ as would be expected if thermally activated escape processes were occurring. Neither is there any sign of the pulse spreading that would be expected to occur if the ions were escaping from vortex rings after a short time delay (figure 25*c*).

If, however, the ions could escape *immediately* from, or equivalently evade capture by, the vortex rings when they are formed there would be no pulse spreading. Provided that this evasion occurred only in high fields, one could then account for the observed drop in the nucleation rate.

It is of particular interest to discuss the extent to which each of the two vortex nucleation models discussed in §1*c* is able to cope with the observed maximum in $\nu(\bar{v})$. First let us consider the peeling model. As the velocity of the ion increases one imagines that the number of trapped rotons (if they exist) also increases, leading to an increase in the nucleation rate $R(v)$. There is no reason to believe that $R(v)$ will decrease at larger velocities; indeed intuition would seem to imply the opposite. The vortex loop when it is created is already joined to the electron bubble as shown in figure 2*a* so that there is then no possibility of the ion evading capture. Unless, for some reason, these very small ion–vortex loop complexes become unstable and break up when the electric field exceeds 10^6 V m^{-1}, the peeling model cannot in any obvious way explain the maximum in $\nu(\bar{v})$.

If the vortex ring is formed in a quantum transition, on the other hand, then one possibility is that it will first appear in a position girdling the ion (Schwarz & Jang 1973) as illustrated in figure 2*b*. As the velocity of the ion increases, so also does the number of places around the ion when the vortex ring can be created. If all such places act as nucleation sites with equal probability, then one would expect $R(v)$ to increase monotonically with v. As the velocity increases further, however, so the vortex rings will be created further from the ion. These individual processes will probably occur less readily since they involve a larger change in the wavefunction of the system. Here, we are supposing that the 'matrix element' for the transition will depend on the overlap of initial and final states of the helium system. If these ideas are correct, then it is possible that the rate $R(v)$ might eventually decrease for large velocities. However, to fit the data we would need to postulate that $R(v)$ decreased to zero for large velocities, and that it did so very rapidly. It is hard to justify a decrease of this form on the basis of the quantum transition model. We are then left with the possibility that the ion evades capture by the vortex ring. In the model of Schwarz & Jang the initial vortex ring is not joined to the ion (figure 2*b*). The ion is acted on by the electric field and by its interaction with the vortex ring. We sketch in figure 36*b* the form of this latter interaction in the x direction for an ion situated at the centre of the vortex ring. If the electric field is larger than max $(\partial V(x)/\partial x)$, then the ion will immediately escape the clutches of the vortex ring. This condition depends upon the initial radius of the vortex ring R, which in turns depends upon the velocity of the ion. Although we have not, as yet, been able to put these ideas on a quantitative basis, it is

PHILOSOPHICAL TRANSACTIONS OF THE ROYAL SOCIETY A MATHEMATICAL, PHYSICAL & ENGINEERING SCIENCES

immediately evident that the evasion process requires both large fields and large velocities of the ion, that it is unlikely to occur on the basis of the peeling model, but that it is certain to occur if the quantum transition model, with something like the Schwarz & Jang initial ring configuration, represents the true state of affairs.

The net result of evasion processes will be that the rate of nucleation will appear to decrease for large velocities and fields. This decrease will be more rapid than if the effective nucleation rate is given by equations (37) and (50) because, as the electric field increases, the minimum size of vortex ring for which evasion can occur will decrease: in effect, the third critical velocity v_{v_3} will be expected to decrease with increasing electric field. This is probably the reason why the theoretical curves of figure 35 exhibit very much broader maxima in $\nu(\bar{v})$ than the experimental data.

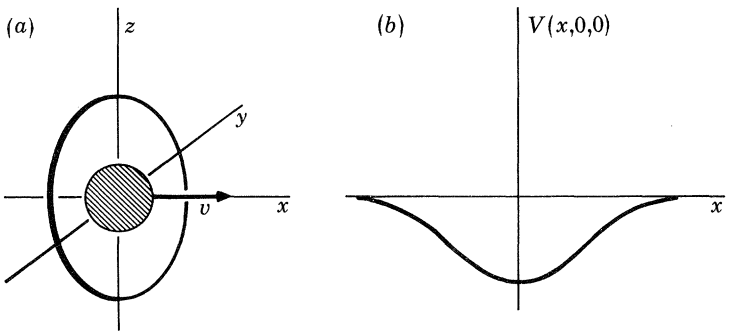

FIGURE 36. Sketch (*a*) of the initial vortex ring, girdling the ion, after being formed in a quantum transition and (*b*) of the variation with x of the effective potential binding ion and ring together. In the interests of clarity, the diameter of the ring has been exaggerated compared to that of the ion.

All the evidence, then, appears to support the view that, at least at low temperatures, vortex rings are produced in a quantum transition and that, in high enough electric fields, the ion–ring complexes that are formed are unstable.

(*d*) *Vortex nucleation at higher temperatures*

As discussed above, the hypothesis that the nucleation rate above 0.5 K arises as the sum of two components, one arising from spontaneous nucleation processes and the other from a second type of nucleation process occurring at a rate proportional to the thermal roton density, can be tested by plotting $[\nu(\bar{v}, T) - \nu_s(\bar{v})]/(T^{\frac{1}{2}} e^{-\Delta/k_B T})$ against $\bar{v}$. The veracity of the hypothesis can be regarded as proven if data recorded at different temperatures all fall on a common curve. In this procedure, we have first plotted $\nu_s(\bar{v})$ and drawn a smooth curve through the data. We have then determined $\nu_s(\bar{v})$ for the velocities required by reading off the values on the smooth curve that we have drawn. This may lead to a systematic error in $\nu(\bar{v}, T) - \nu_s(\bar{v})$ if our estimate of $\nu_s(\bar{v})$ is wrong. The results are shown for pressures between 19 and 25 bar in figure 37. The agreement between data at different temperatures is as good as can be expected, when we bear in mind that any error in $\nu_s(\bar{v})$ will systematically distort the results. For example, at 25 bar the agreement would be improved at velocities of *ca.* 60 m s^{-1} if $\nu_s(\bar{v})$ were smaller by 270 s^{-1}.

At 19 bar one can see clearly the drop in $\nu(\bar{v})$ for velocities above 63 m s^{-1}. The agreement between the three sets of data for lower velocities is quite good, and noticeably better than the agreement at higher velocities. Here we are plotting values of $\bar{v}$ determined experimentally. There is some error in the values of $\bar{v}$ as well as in ν and this error increases at higher velocities.

Part of the poorer agreement seen at higher velocities could be caused by the fact that evasion processes are not properly described by equation (38).

The maximum in $\nu_r(\bar{v})$ occurs for a velocity of 62–63 m s^{-1} for all pressures, whereas the maximum in $\nu_s(\bar{v})$ occurs for a velocity of 66–67 m s^{-1}. A detailed analysis shows that $\nu_r(\bar{v})$ rises slightly less rapidly than $\nu_s(\bar{v})$ with increase in $\bar{v}$ for any given pressure. Apart from this, the curves for $\nu_r(\bar{v})$ and $\nu_s(\bar{v})$ are remarkably similar, which strongly suggests that the underlying physical mechanism for both processes is the same.

It is clear that our hypothesis of a second nucleation process which depends upon the number density of thermal rotons is consistent with experimental results. This seems at first sight to lend support to the view of Donnelly & Roberts that rotons are the prototype vortex rings that seed the nucleation process. We note, however, that the Donnelly & Roberts picture cannot account for the spontaneous nucleation process which occurs in the absence of rotons.

In contrast, as we shall now seek to demonstrate, the quantum transition model (with a small extension) is capable of explaining *both* processes. Let us suppose that a roton collides with the ion and that this sometimes leads to the nucleation of a vortex ring. The nucleation rate would then be proportional, as observed, to n_r. The requirements of energy and momentum conservation require the inclusion of the energy and momentum of the roton, which leads automatically to a reduction in the critical velocity. We now set this idea on a more quantitative basis.

Suppose that spontaneous nucleation first occurs when the ion has momentum p_c. Then

$$p_c^2/2m^* = E_{ir}(p_c), \tag{52}$$

where $E_{ir}(p_c)$ is the energy of the ion ring complex. For the roton assisted process the nucleation first occurs at a momentum of $p_c - \delta p$. Then

$$(p_c - \delta p)^2/2m^* + \Delta = E_{ir}(\boldsymbol{p}_c - \delta\boldsymbol{p} + \hbar\boldsymbol{k}_0). \tag{53}$$

We now expand to first order in small quantities, and put $v_r = \delta E_{ir}/\delta\boldsymbol{p}$, the group velocity of the ion ring complex, yielding

$$\delta\boldsymbol{p}.(v_c - v_r) = \hbar k_0(v_L - v_r\cos\theta), \tag{54}$$

where θ is the angle between $\hbar\boldsymbol{k}_0$ and $\boldsymbol{p}_c$. The critical velocity is then

$$v_c - \delta v = v_c - \frac{\hbar k_0}{m^*}\frac{v_L - v_r\cos\theta}{v_c - v_r}. \tag{55}$$

If v_r is about 11 m s^{-1} (Schwarz & Jang 1973), then we expect the critical velocity to be smaller by about 4 m s^{-1}.

We want to make a quantitative comparison between the spontaneous and roton assisted processes to see if these ideas are correct. Therefore, we fit to theory the low field region of the nucleation data, where the second and third critical velocities are unimportant, using

$$R_s(v) = R\theta(v - v_c) \tag{56}$$

and

$$R_r(v) = R'n_r\theta(v - v_c + \delta v). \tag{57}$$

The absolute values of v_c obtained in this way may be in error because of the choice of this particular form for $R(v)$, but here we are primarily interested in the values of δv. The approximation above serves this purpose well.

It is necessary to average over all orientations of the roton's momentum for the roton-assisted process. Thus,

$$\nu_{\mathrm{r}}(\bar{v}) = \tfrac{1}{2}R'n_{\mathrm{r}}\int_0^{\pi} \mathrm{d}\theta \sin\theta \int_{v_{\mathrm{c}}-\delta v}^{\infty} \mathrm{d}v\, f(v, \bar{v}). \tag{58}$$

It is then possible to fit the data with use of R' and v_{r} as adjustable parameters (R and v_{c} are already known from fitting the data for the spontaneous process). The data at 17 and 25 bar are unsuitable: at 25 bar one cannot obtain v_{c} with sufficient accuracy because ν_{s} is too small, whereas at 17 bar ν is so high that we cannot measure $\bar{v}$ accurately. The full curves of figure 37*b–d* show our best fit to the low field data at intermediate pressures.

There are several sources of error. First, as discussed in §3*a*, there may be a systematic error in the values of $\nu(\bar{v})$ of order 50 s^{-1}. This error is absent from the values of $\nu_{\mathrm{r}}(\bar{v})$, however, that are obtained by subtracting two experimental values of ν. Secondly, there is scatter in the

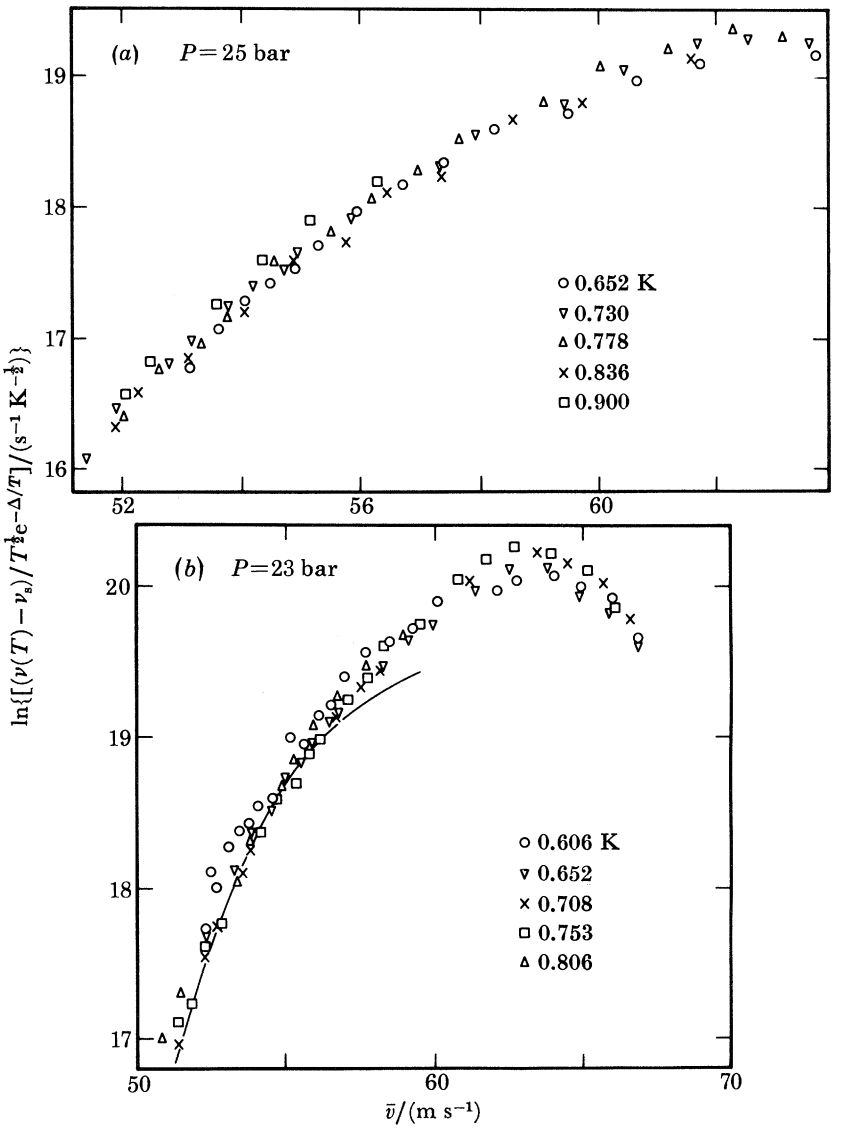

FIGURE 37 (*a*) AND (*b*). For description see opposite.

data which leads to some freedom in choosing the parameters that fit the data. The net result is a relatively small error in the critical velocities but a larger error in the derived value of v_r.

In table 7 we show the values of R' and v_r obtained in this way, together with our estimates of the error in v_r. Also shown are the values predicted by Schwarz & Jang. We have estimated a larger error at 23 bar: this is mainly because of the uncertainty in v_c obtained from $\nu_s(\bar{v})$.

In view of the simplicity of the model, it is quite remarkable how well the values of v_r agree with those predicted by Schwarz & Jang. Although the closeness of the agreement is no doubt fortuitous, particularly in view of uncertainties about the value of the vortex core parameter, it may none the less be concluded that the model is consistent with experiment.

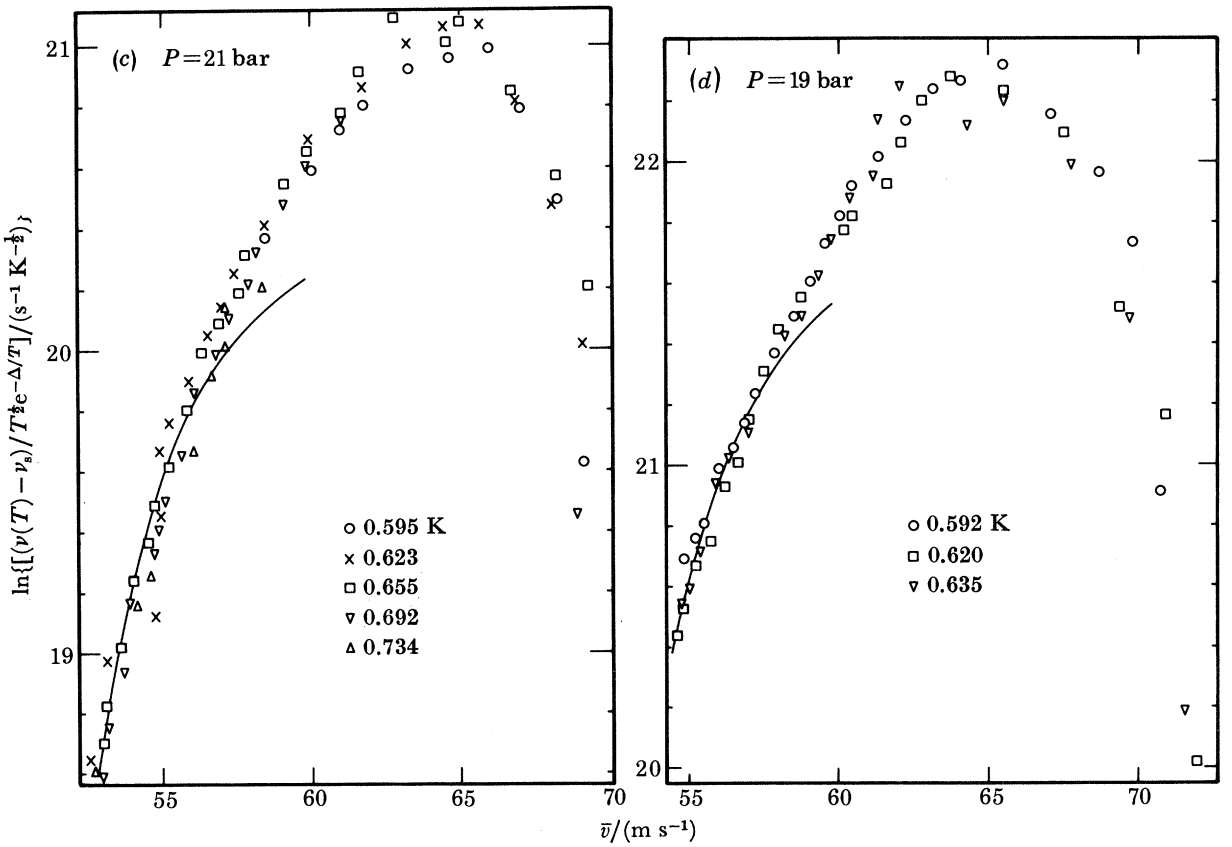

FIGURE 37. Test of the hypothesis that there is a temperature-driven nucleation process which, for any given ionic drift velocity $\bar{v}$, occurs at a rate that is directly proportional to the thermal roton density, n_r. For each pressure, the temperature driven nucleation rate $[\nu(\bar{v}, T) - \nu_s(\bar{v})]$, divided by the temperature dependent part of n_r, $[T^{\frac{1}{2}} e^{-\Delta/k_B R}]$, has been plotted in the form of the natural logarithm against $\bar{v}$ for a number of different temperatures. Within experimental error, the data at each pressure form a common curve, thus lending support to the hypothesis. The full curves of (*b*), (*c*) and (*d*) represent fits of theory to the data at low $\bar{v}$.

TABLE 7. NUMERICAL VALUES OF PARAMETERS USED IN FITTING EQUATION (58) TO HIGH TEMPERATURE VORTEX NUCLEATION $\nu_T(\bar{v})$ DATA

P/bar	19	21	23
$R'/(\mathrm{m^3\ s^{-1}})$	5.4×10^{-18}	1.5×10^{-18}	7.0×10^{-19}
$v_r/(\mathrm{m\ s^{-1}})$	11 ± 5	11 ± 5	16 ± 8
$v_r^{SJ}/(\mathrm{m\ s^{-1}})$	11.8	11.5	11.0

There is one other point that should be made. The maximum in $\nu_s(\bar{v})$ occurs at a velocity larger by about 4 m s^{-1} than the maximum in $\nu_r(\bar{v})$. The roton releases energy to help create the vortex ring. With more energy available, a larger vortex ring can be created. Consequently, an ion travelling at, say, 65 m s^{-1} will be trapped by the vortex ring that is formed spontaneously, whereas it will perhaps evade capture by the larger ring formed with the assistance of a roton. Thus evasion processes would be expected to become important at lower velocities for the roton driven nucleation mechanism than for the spontaneous mechanism, in agreement with experiment.

5. Conclusion

The principal conclusions emerging from these investigations may be summarized as follows.

(i) There exist two distinct mechanisms through which a negative ion can nucleate the creation of a quantized vortex ring in isotopically pure superfluid ^{4}He. The first of these occurs spontaneously at a rate that is independent of temperature. The second, which occurs only in the presence of rotons, is characterized by a nucleation rate that is directly proportional to the thermal roton density for any given ionic drift velocity, and it becomes the dominant nucleation mechanism above *ca.* 0.6 K.

(ii) Both mechanisms give rise to nucleation rates that at first increase with increasing drift velocity but then decrease again at very high velocities.

(iii) The variation of nucleation rate with drift velocity is consistent with there being a critical velocity for the onset of vortex nucleation. The critical velocity is larger for the spontaneous than for the roton-driven nucleation mechanism.

(iv) Vortex nucleation by either mechanism is a probabilistic process: this is demonstrated by the fact that the signals retain their exponentiality even when the ionic drift velocity has become comparable with, or exceeds, the first critical velocity.

(v) The magnitude of the critical velocity for spontaneous nucleation, and the magnitude of the difference in the critical velocities for the two processes, are both consistent with the conditions imposed by a requirement for the conservation of energy and momentum.

(vi) Although the use of equation (50) enables the $\nu(\bar{v})$ data to be fitted over a wide range, no other evidence has been adduced to support the view that v_{v_2} necessarily represents a real critical velocity for the onset of an additional (spontaneous) nucleation process; and the very rapid fall of $\nu(\bar{v})$ at high velocities and electric fields seems to suggest that the quantity v_{v_3} may, in fact, be dependent on field. For the present, therefore, this equation should probably be viewed simply as a convenient means of parametrizing the experimental results.

(vii) The decreased nucleation rate found at very high drift velocities may arise either from the ion evading capture by the vortex ring that it has created, or from a genuine decrease in the nucleation rate at very high instantaneous velocities. Both possibilities are consistent with the quantum transition model; and both appear to be inconsistent with the peeling model of vortex ring creation as at present envisaged. We believe the evasion hypothesis to be the more plausible.

We conclude that, of the models of the vortex nucleation process proposed to date, the quantum transition model in the form developed by Schwarz & Jang (1973) seems best able (with a small extension) to describe the measurements reported in this paper; but we would emphasize that this should not be taken as implying that their model is *necessarily* correct because, as these authors are themselves at pains to point out, there are several reasons why the

PHILOSOPHICAL TRANSACTIONS OF THE ROYAL SOCIETY A MATHEMATICAL, PHYSICAL & ENGINEERING SCIENCES

theory can only be regarded as semi-quantitative, at best. Nonetheless, it does appear to be capable of accounting remarkably well for most of the features which have been observed in the experiments.

It is a pleasure to record our thanks to Mr R. F. C. Dobbs and Mr J. C. H. Small for their help during the acquisition of some of the data. We are greatly indebted to Professor W. M. Fairbairn for his assistance in developing the electrostatic induction technique. We acknowledge valuable discussions with Dr C. Muirhead, Dr K. W. Schwarz and Professor W. F. Vinen, F.R.S. The research programme was supported by the Science Research Council to whom three of us (F.E.M., G.G.N., P.C.E.S.) are also grateful for the support, respectively, of a Senior Visiting Fellowship, a Research Associateship and an Advanced Course Studentship.

Appendix A. Derivation of some equations used in §2*a*

We show here how to calculate the induced charge $q(z_0)$ and potential $\Phi_0(\boldsymbol{x})$ in the experimental cell (as discussed in §2*a*).

The assumption of perfectly conducting walls for the model cells means that we can assume fairly simple boundary conditions for the solution of Poisson's equation $\nabla^2\Phi(x) = \rho(\boldsymbol{x})$, where $\rho(\boldsymbol{x})$ is the charge density. We consider the cell of figure 4, with disc of charge density $\rho_{z_0}(\boldsymbol{x}')$. The potential in the cell will be a sum $\Phi(\boldsymbol{x}) = \Phi_0(\boldsymbol{x}) + \Phi_1(\boldsymbol{x})$ of contributions from the cell walls and the charged disc respectively, with $\Phi_0(\boldsymbol{x}) \gg \Phi_1(\boldsymbol{x})$. It is assumed that the contribution to $\Phi_0(\boldsymbol{x})$ from charge induced on the cell walls by the disc is negligible, so that $\Phi_0(\boldsymbol{x})$ is fixed externally by the potential distribution $\Phi_0(S)$ on the walls.

A very convenient way of calculating $\Phi(x)$ is to construct the Green function or inverse operator for Laplace's equation in this geometry (see Jackson (1975) or Courant & Hilbert (1953) for details of this method). Then the potential at any point $\boldsymbol{x}$ in the cell due to a unit charge placed at a point $\boldsymbol{x}'$ is given by $G(\boldsymbol{x}, \boldsymbol{x}')/\epsilon_4$ where $G(\boldsymbol{x}, \boldsymbol{x}')$ satisfies

$$\nabla'^2/G(\boldsymbol{x}, \boldsymbol{x}') = -\delta(\boldsymbol{x} - \boldsymbol{x}')$$

and the boundary condition $G(\boldsymbol{x}, \boldsymbol{x}') = 0$ if $\boldsymbol{x}$ or $\boldsymbol{x}'$ lie on the conducting wall surface S (ϵ_4 is the dielectric constant of superfluid ^{4}He).

The potential $\Phi(\boldsymbol{x})$ will then be given by

$$\Phi(\boldsymbol{x}) = \Phi_0(\boldsymbol{x}) + \Phi_1(\boldsymbol{x}), \quad \text{where} \quad \Phi_0(\boldsymbol{x}) = -\iint_S \mathrm{d}\boldsymbol{S}.\nabla' G(\boldsymbol{x}, \boldsymbol{x}')\, \Phi_0(\boldsymbol{x}'), \quad \boldsymbol{x}' \text{ on } S, \tag{A 1a}$$

and

$$\Phi_1(\boldsymbol{x}) = \frac{1}{\epsilon_4} \iiint_v \mathrm{d}^3x' G(\boldsymbol{x}, \boldsymbol{x}')\, \rho(\boldsymbol{x}'). \tag{A 1b}$$

The induced charge on the collector plate will be given by

$$q(z_0) = \epsilon_4 \iint_S{}' \mathrm{d}\boldsymbol{S}.\nabla\Phi_1(\boldsymbol{x}) \tag{A 1c}$$

($\boldsymbol{x}$ on S; integration only over surface of collector plate).

The Green function is conveniently expanded as follows,

$$G(\boldsymbol{x}, \boldsymbol{x}') = \frac{1}{2\pi^2} \sum_{\nu=-\infty}^{\infty} \int \mathrm{d}k\, \mathrm{e}^{\mathrm{i}\nu(\phi-\phi')} \sin k(z-z')\, g_\nu(kr, kr'),$$

where $\boldsymbol{x} = (r, z, \phi)$, $\boldsymbol{x}' = (r', \phi', z')$; $g_\nu(kr, kr')$ satisfies

$$\left\{\frac{1}{r}\frac{\mathrm{d}}{\mathrm{d}r}\left(r\frac{\mathrm{d}}{\mathrm{d}r}\right)-\left(k^2+\frac{\nu^2}{r^2}\right)\right\} g_\nu(kr, kr') = -\frac{1}{r}\,\delta(r-r').$$

By symmetry we can write in the usual way for Green functions that

$$\begin{aligned} g_\nu(kr, kr') &= -(1/\gamma)\; U_1^\nu(kr)\; U_2^\nu(kr') \quad (r \leqslant r') \\ &= -(1/\gamma)\; U_1^\nu(kr')\; U_2^\nu(kr) \quad (r \geqslant r'), \end{aligned}$$

where $\gamma = krW_{12}$, and W_{12} is the Wronskian of $U_1(kr)$ and $U_2(kr)$. Then, by standard methods, employing the boundary conditions on $G(\boldsymbol{x}, \boldsymbol{x}')$, we arrive at the following form for the Green function:

$$G(x, x') = \frac{1}{\pi L}\sum_{n=1}^{\infty}\sum_{\nu=-\infty}^{\infty} \mathrm{e}^{\mathrm{i}\nu(\phi-\phi')} \sin(k_n z) \sin(k_n z')\, g_\nu(k_n r, k_n r'),$$

where

$$g_\nu(k_n r, k_n r') = I_\nu(k_n r_<)\left[K_\nu(k_n r_>) - \frac{K_\nu(k_n R)}{I_\nu(k_n R)}\, I_\nu(k_n r_>)\right]$$

and $r_>$, $r_<$ signifies that the greater or lesser of r, r' should be taken, and $k_n = n\pi/L$.

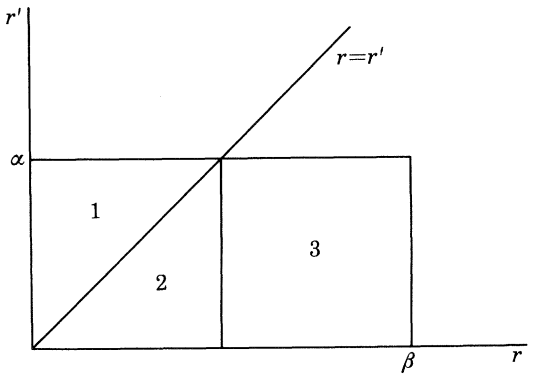

FIGURE A 1. Division of the (r, r') plane into three parts for the calculation of the integrals of equations (A 2) and (A 3).

Now in working out $q(z_0)$ and $\Phi_0(\boldsymbol{x})$ we will repeatedly come up against integrals of the form

$$f_R^\alpha(r) = \int_0^\alpha r'\,\mathrm{d}r'\, g_0(k_n r, k_n r') \qquad (\mathrm{A}\ 2)$$

and

$$F_\alpha^\beta(k_n R) = \int_0^\beta r\,\mathrm{d}r \int_0^\alpha r'\,\mathrm{d}r'\, g_0(k_n r, k_n r') = \int_0^\beta r\,\mathrm{d}r\, f_R^\alpha(r) \quad (\beta > \alpha). \qquad (\mathrm{A}\ 3)$$

It is convenient in calculating these integrals to divide up the region of integration in the (r, r') plane into three parts. Suppose, for example, that we calculate $F_\alpha^\beta(k_n R)$. Then $\beta > \alpha$, and we divide as shown in figure A 1.

A number of standard relations involving Bessel functions are useful for these and other integrations:

$$\frac{\mathrm{d}}{\mathrm{d}x}(x^n I_n(x)) = x^n I_{n-1}(x), \quad \frac{\mathrm{d}}{\mathrm{d}x} I_0(x) = I_1(x), \qquad (\mathrm{A}\ 4a)$$

$$\frac{\mathrm{d}}{\mathrm{d}x}(x^n K_n(x)) = -x^n K_{n-1}(x), \quad \frac{\mathrm{d}}{\mathrm{d}x} K_0(x) = -K_1(x), \qquad (\mathrm{A}\ 4b)$$

$$I_n(x)\, K_{n-1}(x) + K_n(x)\, I_{n-1}(x) = -W[I_n(x), K_n(x)] = 1/x. \qquad (\mathrm{A}\ 4c)$$

Then $F^{\beta}_{\alpha}(k_n R)$ is given by

$$\begin{aligned} F^{\beta}_{\alpha}(k_n R) &= \mathscr{I}_1 + \mathscr{I}_2 + \mathscr{I}_3 \\ &= \int_0^{\alpha} r\,\mathrm{d}r \int_r^{\alpha} r'\,\mathrm{d}r'\, U^0_1(k_n r)\; U^0_2(k_n r') \\ &\quad + \int_0^{\alpha} r\,\mathrm{d}r \int_0^{\alpha} r'\,\mathrm{d}r'\, U^0_1(k_n r')\; U^0_2(k_n r) \\ &\quad + \int_{\alpha}^{\beta} r\,\mathrm{d}r \int_0^{\alpha} r'\,\mathrm{d}r'\, U^{\circ}_1(k_n r')\; U^{\circ}_2(k_n r). \end{aligned}$$

The integral $\mathscr{I}_1 + \mathscr{I}_2$ is then easily found (by using the above relation for Bessel functions) to be

$$\mathscr{I}_1 + \mathscr{I}_2 = F^{\alpha}_{\alpha}(k_n R) = \frac{\alpha}{k_n}\left\{\tfrac{1}{2} - I_1(k_n\alpha)\left[K_1(k_n\alpha) - \frac{K_0(k_n R)}{I_0(k_n R)}\, I_1(k_n\alpha)\right]\right\}$$

and $\mathscr{I}_3$ is given by

$$\mathscr{I}_3 = \frac{\alpha}{k_n^2}\, I_1(k_n\alpha)\left\{\alpha K_1(k_n\alpha) - \beta K_1(k_n\beta) - \frac{K_0(k_n R)}{I_0(k_n R)}\left[\alpha I_1(k_n\alpha) - \beta I_1(k_n\beta)\right]\right\},$$

so that

$$F^{\beta}_{\alpha}(k_n R) = \frac{\alpha}{k_n^2}\left\{\tfrac{1}{2}\alpha - \beta I_1(k_n\alpha)\left[K_1(k_n\beta) + \frac{K_0(k_n R)}{I_0(k_n R)}\, I_1(k_n\beta)\right]\right\}. \tag{A 5}$$

In calculating $F^{\beta}_{\alpha}(k_n R)$ we also produce the answer for $f^{\alpha}_{R}(r)$:

$$f^{\alpha}_{R}(r) = \frac{\alpha}{k_n}\, I_1(k_n\alpha)\left[K_0(k_n r) - \frac{K_0(k_n R)}{I_0(k_n R)}\, I_0(k_n r)\right] \quad (r \geqslant \alpha) \tag{A 6a}$$

$$= \frac{1}{k_n^2} - \frac{\alpha}{k_n}\cdot I_0(k_n r)\left[K_1(k_n\alpha) + \frac{K_0(k_n R)}{I_0(k_n R)}\, I_1(k_n\alpha)\right] \quad (r \leqslant \alpha). \tag{A 6b}$$

We now go on to consider the three model cells discussed in §2.

Model cell (a)

Treating first the case of an infinitely thin uniformly charged disc, with

$$\rho_{z_0}(\boldsymbol{x}') = (Q/\pi a^2)\;\delta(z' - z_0)\;\theta(a - r'),$$

we find by integrating over ϕ' and z' in equation (A 1*b*) and using the axial symmetry of the problem, that

$$\Phi_1(\boldsymbol{x}) = \frac{2Q}{\pi a^2 L}\int_0^a r'\,\mathrm{d}r' \sum_{n=1}^{\infty} \sin(k_n a)\sin(k_n z_0)\, g_0(k_n r, k_n r'),$$

so that

$$\begin{aligned} q(z_0) &= \lim_{z\to L}\frac{4Q}{a^2 L}\int_0^b r\,\mathrm{d}r\,\frac{\partial}{\partial z}\int_0^a r'\,\mathrm{d}r' \sum_{n=1}^{\infty}\sin(k_n z)\sin(k_n z_0)\, g_0(k_n r, k_n r') \\ &= \frac{4Q}{a^2 L}\sum_{n=1}^{\infty}(-1)^n\, k_n \sin(k_n z_0)\, F^b_a(k_n R). \end{aligned}$$

From this relation we obtain equations (4*a*) and (4*b*) of the main text. Similarly, from equation (A 1*a*) we have

$$\Phi_0(\boldsymbol{x}) = \frac{-2V}{L}\sum_{n=1}^{\infty}(-1)^n \sin(k_n z)\, f^b_R(r),$$

which comes to

$$\Phi_0(\boldsymbol{x}) = \frac{V}{L}\left\{z + 2b\sum_{n=1}^{\infty}(-1)^n \sin(k_n z)\, I_0(k_n r)\left[K_1(k_n b) + \frac{K_0(k_n R)}{I_0(k_n R)}\, I_1(k_n b)\right]\right\} \quad (r \leqslant b)$$

$$= \frac{-2bV}{L}\sum_{n=1}^{\infty}(-1)^n \sin(k_n z)\, I_1(k_n b)\left[K_0(k_n r) - \frac{K_0(k_n R)}{I_0(k_n R)}\, I_0(k_n r)\right] \quad (r \leqslant b),$$

which upon differentiation ($E(\boldsymbol{x}) = -\nabla\Phi(x)$) give relations (7*a*)–(7*d*) of the main text. In deriving these expressions for $q(z_0)$ and $\Phi_0(\boldsymbol{x})$ we have used the Fourier expansion of a ramp function:

$$\frac{Qz_0}{L} = -2Q\sum_{n=1}^{\infty}\frac{(-1)^n}{n\pi}\sin\left(\frac{n\pi z_0}{L}\right).$$

If we allow a variation of $\rho_{z_0}(\boldsymbol{x}')$ with r', so that

$$\rho_{z_0}(\boldsymbol{x}') = \frac{Q}{\pi a^2}\,\delta(z'-z_0)\,\theta(a-r')\,\rho(r'),$$

where

$$\int_0^R r'\,\mathrm{d}r'\rho(r') = \tfrac{1}{2}a^2,$$

then

$$q(z_0) = \frac{4Q}{\alpha^2 L}\sum_{n=1}^{\infty}(-1)^n k_n \sin(k_n z_0)\int_0^a r'\,\mathrm{d}r'\rho(r')\,f_R^b(r'),$$

which results in the factor, given in the main text, multiplying the nonlinear terms in $q(z_0)$:

$$\frac{Qk_n}{aI_1(k_n a)}\int_0^a r'\,\mathrm{d}r'\rho(r')\,I_0(k_n r').$$

Model cell (b)

The behaviour of cell (*b*) may easily be calculated from first principles as above, but it is easier to look at what happens when we let $b = R$ for model cell (*a*). In this case, using equation (A 4*c*), we get

$$q(z_0) = -Q\left\{\frac{z_0}{L} + \frac{4L}{a}\sum_{n=1}^{\infty}\frac{(-1)^n}{(n\pi)^2}\sin(k_n z_0)\,\frac{I_1(k_n a)}{I_0(k_n R)}\right\}, \tag{A 7a}$$

$$\Phi_0(\boldsymbol{x}) = \frac{V}{L}\left\{z + 2L\sum_{n=1}^{\infty}\frac{(-1)^n}{n\pi}\sin(k_n z)\,\frac{I_0(k_n r)}{I_0(k_n R)}\right\}. \tag{A 7b}$$

We can readily relate these solutions to those for model cell (*b*) by symmetry (substituting $x \to (L-z)$ and changing the potential accordingly), obtaining equations (5) and (8) of the main text.

Model cell (c)

The behaviour of $q(z_0)$, being determined only by the shape of the collector plate, is clearly given by (A 7*a*). That $\Phi_0(\boldsymbol{x}) = Vz/L$ is intuitively obvious, but we may easily check it by calculating directly from equation (A 1*a*). Indeed, for an arbitrary potential distribution $\Phi(z)$ on the side walls, we obtain the solution

$$\Phi_0(\boldsymbol{x}) = \sum_{n=1}^{\infty} c_n \sin(k_n z)\,\frac{I_0(k_n r)}{I_0(k_n R)},$$

where

$$c_n = \frac{2}{L}\int_0^L \mathrm{d}z\,\Phi(z)\sin(k_n z),$$

which must in general be added to the potential determined by the top and bottom collector plates.

Appendix B. Tabular vortex nucleation data

A small selection of measured nucleation rates ν is presented in tabular form, covering the full experimental range of pressure P, temperature T and electric field E. The raw measurements of ν have been corrected by the addition of $\nu_0 = 50\ \mathrm{s}^{-1}$ (see §3*a*) and rounded to three significant figures. Experimental errors are estimated to lie within: ± 0.03 bar in P; ± 3 mK

Table B 1. Nucleation rates at $P = 25$ bar

(The measured nucleation rate ν is given for various electric fields E and temperatures T.)

T/K ...	0.297	0.592	0.652	0.730	0.778	0.836	0.906
E / 10^4 V m^{-1}	ν/s^{-1}						
13.5	—	—	299	918	1130	1170	367
20.3	—	215	550	1710	2490	3380	3790
29.3	226	424	989	2810	4770	7470	10600
45.0	651	1020	2010	5560	9790	13900	27100
67.5	1740	2290	3910	10000	17700	25600	54200
90.0	3430	4080	5900	13700	24700	35700	—
113	4110	4730	6520	13500	24100	—	—

Table B 2. Nucleation rates at $P = 23$ bar

(The measured nucleation rate ν is given for various electric fields E and temperatures T.)

T/K ...	0.297	0.571	0.606	0.652	0.708	0.753	0.806	0.869
E / 10^4 V m^{-1}	ν/s^{-1}							
5.62	—	—	—	372	545	517	—	—
9.00	—	—	480	813	1410	1610	1500	—
13.5	—	492	639	1340	2690	4020	4990	2200
20.3	331	830	1190	2170	4530	7080	11500	13400
29.3	821	1390	2060	3490	7400	12400	20300	31500
45.0	2190	2790	3950	6020	12400	21400	36900	59700
67.5	5170	6050	7270	10200	19700	34200	59300	113000
90.0	7760	8700	9860	12800	22700	38500	66500	144000
113	7620	8270	9330	11400	18500	30400	55600	133000

Table B 3. Nucleation rates at $P = 21$ bar

(The measured nucleation rate ν is given for various electric fields E and temperatures T.)

T/K ...	0.324	0.555	0.595	0.623	0.655	0.692	0.734	0.784
E / 10^4 V m^{-1}	ν/s^{-1}							
5.62	—	410	671	977	1350	1950	2330	710
9.00	303	776	1270	1860	2710	3980	6110	6090
13.5	658	1270	2040	2930	4450	6550	10600	14100
20.3	1600	2080	3220	4700	7180	11100	18000	29600
29.3	3010	3660	5260	7340	10800	17000	28300	47800
45.0	6540	7400	9300	12200	17600	26700	42800	73000
67.5	12200	13500	15600	19000	24700	37000	57200	108000
90.0	14400	16100	17500	20100	25300	34200	56000	91100
113	12400	13200	13800	15700	18400	23900	36200	59500

in T; $\pm 1\%$ in E, subject to a possible additional systematic error related to uncertainty in the absolute value of the Landau critical velocity (see §2*b*); $\pm 50\ s^{-1}$ systematic error, plus scatter, in ν. Tables B1–B5, covering $17 < P < 25$ bar, include data for a range of temperatures, but table B6 for 15 and 16 bar provides results only at *ca.* 0.3 K because the signal became too small to use at higher temperatures (see §3*a*).

TABLE B 4. NUCLEATION RATES AT $P = 19$ bar

(The measured nucleation rate ν is given for various electric fields E and temperatures T.)

T/K ...	0.297	0.553	0.592	0.620	0.635	0.652
E / 10^4 V m^{-1}	ν/s^{-1}					
5.62	502	1730	2510	3500	4440	5970
9.00	1550	3120	4530	6240	7980	11700
13.5	3100	5140	7230	9980	11800	17300
20.3	5320	8200	11400	15400	18900	27100
29.3	8970	12900	16800	30000	27400	35200
45.0	18300	23600	28100	35200	41100	52100
67.5	26300	32700	35800	42900	48200	56800
90.0	25600	29800	31800	35700	38400	42100
113	19600	21600	21900	23300	25100	26400

TABLE B 5. NUCLEATION RATES AT $P = 17$ bar

(The measured nucleation rate ν is given for various electric fields E and temperatures T.)

T/K ...	0.324	0.515	0.555	0.595
E / 10^4 V m^{-1}	ν/s^{-1}			
5.62	2480	4510	6350	9130
9.00	5610	8010	10800	17800
13.5	8880	12400	17300	26000
20.3	13700	19100	26000	39500
29.3	24500	33500	40000	60100
45.0	43200	51100	61600	87100
67.5	48200	55900	62500	73900
90.0	44600	46700	51400	56900
113	35600	35300	37600	42900

TABLE B 6. NUCLEATION RATES AT $P = 15$ AND $P = 16$ bar

(The measured nucleation rate ν is given for various electric fields E at a temperature of *ca.* 0.3 K, where ν is temperature independent, for $P = 15$ and $P = 16$ bar.)

P/bar ...	15	16
E / 10^4 V m^{-1}	ν/s^{-1}	
5.62	9270	4900
9.00	13900	9100
13.5	19600	13700
20.3	40200	22100
29.3	69000	40000
45.0	81400	62700
67.5	88000	65000
90.0	86500	61800
113	99600	55000

PHILOSOPHICAL TRANSACTIONS OF THE ROYAL SOCIETY A MATHEMATICAL, PHYSICAL & ENGINEERING SCIENCES

Appendix C. Tabular drift velocity data

A small selection of low temperature velocity data, covering the full experimental range of pressure and electric field, is presented in table C 1. These differ slightly from some of the data presented previously in I and II because, as discussed in §2*b*, the measured length of the cell has been scaled slightly to yield an intercept for v_L at 25 bar that is in agreement with a more recent set of roton parameters (Brooks & Donnelly 1977; see table 3).

Table C 1. Drift velocities at low temperatures

(The measured drift velocity $\bar{v}$ is given for various pressures P and electric fields E in the temperature independent régime.)

P/bar ...	17	19	21	23	25
E/10^4 V m^{-1}	$\bar{v}$/(m s^{-1})				
5.62	56.63	55.40	53.80	52.60	51.48
9.00	58.10	56.73	54.93	53.63	52.51
13.5	59.78	58.16	56.13	54.89	53.54
20.3	61.60	59.82	57.82	56.41	54.79
29.3	63.50	61.66	59.52	58.05	56.34
45.0	—	64.37	62.02	60.40	58.42
67.5	—	67.35	64.90	63.02	60.88
90.0	73.67	69.84	67.40	65.20	62.94
113	75.98	72.15	69.39	67.19	64.68

References

Allum, D. R. & McClintock, P. V. E. 1976 *J. Phys.* C **9**, L273–L276.

Allum, D. R. & McClintock, P. V. E. 1978*a* *J. Phys., Paris* C **6**, 174–175.

Allum, D. R. & McClintock, P. V. E. 1978*b* *J. low Temp. Phys.* **31**, 321–338.

Allum, D. R., McClintock, P. V. E., Phillips, A. & Bowley, R. M. 1977 *Phil. Trans. R. Soc. Lond.* A **284**, 179–224.

Atkins, M. & McClintock, P. V. E. 1976 *Cryogenics* **16**, 733–734.

Blount, E. I. & Varma, C. M. 1976 *Phys. Rev.* B **14**, 2388–2399.

Bowley, R. M. 1976 *J. Phys.* C **9**, L367–L370.

Bowley, R. M., McClintock, P. V. E., Moss, F. E. & Stamp, P. C. E. 1980 *Phys. Rev. Lett.* **44**, 161–164.

Bowley, R. M. & Sheard, F. W. 1977 *Phys. Rev.* B **16**, 244–254.

Brooks, J. S. & Donnelly, R. J. 1977 *J. Phys. Chem. Ref. Data* **6**, 51–104.

Careri, G., Cunsolo, S., Mazzoldi, P. & Santini, M. 1965 *Phys. Rev. Lett.* **15**, 392–396.

Courant, R. & Hilbert, D. 1953 *Methods of mathematical physics*, vol. 1, pp. 351–388. New York: Interscience.

Donnelly, R. J. & Roberts, P. H. 1969 *Proc. R. Soc. Lond.* A **312**, 519–551.

Donnelly, R. J. & Roberts, P. H. 1971 *Phil. Trans. R. Soc. Lond.* A **271**, 41–100.

Donnelly, R. J. & Roberts, P. H. 1977 *J. Phys.* C **10**, L633–L635.

Ellis, T., Jewell, C. I. & McClintock, P. V. E. 1980*b* *Physics Lett.* A **78**, 358–360.

Ellis, T., McClintock, P. V. E., Bowley, R. M. & Allum, D. R. 1980*a* *Phil. Trans. R. Soc. Lond.* A **296**, 581–595.

Fetter, A. L. 1976 In *The physics of liquid and solid helium* (ed. K. H. Benneman & J. B. Ketterson), p. 1, ch. 3. New York: J. Wiley & Sons.

Iordanskii, S. V. 1965 *Zh. eksp. teor. Fis.* **48**, 708–714; translated in *Soviet Phys. JETP* **21**, 467–471.

Jackson, J. D. 1975 *Classical electrodynamics* (2nd edn), chs 2 and 3. New York: J. Wiley and Sons.

Landau, L. D. 1941 *J. Phys. Moscow* **5**, 71–90. (Reprinted in Khalatnikov, I. M. 1965 *Introduction to the theory of superfluidity*, pp. 185–204. New York: W. A. Benjamin.)

Landau, L. D. 1947 *J. Phys. Moscow* **11**, 91–92. (Reprinted in Khalatnikov, I. M. 1965 *Introduction to the theory of superfluidity*, pp. 205–206. New York: W. A. Benjamin.)

Langer, J. S. & Fisher, M. E. 1967 *Phys. Rev. Lett.* **19**, 560–563.

McClintock, P. V. E. 1978 *Cryogenics* **18**, 201–208.

McClintock, P. V. E., Moss, F. E. & Bowley, R. M. 1980*a* *Phys. Lett.* A **76**, 303–305.

McClintock, P. V. E., Moss, F. E. & Bowley, R. M. 1980*b* *J. Phys.* C **13**, L503–L509.

McClintock, P. V. E., Moss, F. E., Nancolas, G. G. & Stamp, P. C. E. 1981 Proc. 16th Int. Conf. Low Temp. Phys. *Physica* B **107**, 573–574.

PHILOSOPHICAL TRANSACTIONS OF THE ROYAL SOCIETY A MATHEMATICAL, PHYSICAL & ENGINEERING SCIENCES

Meyer, L. & Reif, F. 1961 *Phys. Rev.* **123**, 727–731.
Neeper, D. A. 1968 *Phys. Rev. Lett.* **21**, 274–275.
Neeper, D. A. & Meyer, L. 1969 *Phys. Rev.* **182**, 223–234.
Ngan, T. H., Small, J. C. H. & McClintock, P. V. E. 1981 Proc. 16th Int. Conf. Low Temp. Phys. *Physica* B **107**, 597–598.
Ostermeier, R. M. 1973 *Phys. Rev.* A **8**, 514–529.
Padmore, T. C. 1972 *Phys. Rev.* A **5**, 356–372.
Phillips, A. & McClintock, P. V. E. 1974 *J. Phys.* C **7**, L118–L122.
Phillips, A. & McClintock, P. V. E. 1975 *Phil. Trans. R. Soc. Lond.* A **278**, 271–310.
Pines, D. 1966 In *Quantum fluids* (ed. D. F. Brewer), p. 328. Amsterdam: North-Holland.
Pippard, A. B. 1972 In *Forces and particles: an outline of the principles of classical physics*, p. 168. London: Macmillan.
Rayfield, G. W. 1966 *Phys. Rev. Lett.* **16**, 934–936.
Rayfield, G. W. 1967 *Phys. Rev. Lett.* **19**, 1371–1373.
Rayfield, G. W. 1968*a* *Phys. Rev.* **168**, 222–233.
Rayfield, G. W. 1968*b* *Phys. Rev. Lett.* **20**, 1467–1468.
Rayfield, G. W. & Reif, F. 1964 *Phys. Rev.* **136**, A1194–1208.
Schwarz, K. W. & Jang, P. S. 1973 *Phys. Rev.* A **8**, 3199–3210.
Scott, R. J. & McClintock, P. V. E. 1977 *Phys. Lett.* A **64**, 205–207.
Stamp, P. C. E., McClintock, P. V. E. & Fairbairn, W. M. 1979 *J. Phys.* C **12**, L589–L593.
Strayer, D. M., Donnelly, R. J. & Roberts, P. H. 1971 *Phys. Rev. Lett.* **26**, 165–169.
Titus, J. A. & Rosenshein, J. S. 1973 *Phys. Rev. Lett.* **31**, 146–149.
Wilks, J. 1967 *The properties of liquid and solid helium*. Oxford: Clarendon Press.
Zoll, R. 1976 *Phys. Rev.* B **14**, 2913–2926.
Zoll, R. & Schwarz, K. W. 1973 *Phys. Rev. Lett.* **31**, 1440–1443.

Note added in proof, 30 *August* 1982. Very recent experiments (G. G. Nancolas & P. V. E. McClintock, *Phys. Rev. Lett.* **48**, 1100–1192; 1982) have shown that the ion/vortex-ring transition can be quenched completely by the application of a sufficiently strong electric field ($\nu = 0$ for $E \gtrsim 2 \times 10^6\,\mathrm{V\,m^{-1}}$). This result appears to be fully consistent with the evasion model proposed in §4(c) above.

PHILOSOPHICAL TRANSACTIONS OF THE ROYAL SOCIETY A MATHEMATICAL, PHYSICAL & ENGINEERING SCIENCES